AFRL-AFOSR-VA-TR-2016-0311

Understanding the fundamental roles of momentum and vorticity injections in flow control

Kunihiko Taira
FLORIDA STATE UNIV TALLAHASSEE
874 TRADITIONS WAY
TALLAHASSEE, FL 32306 - 0001

09/02/2016
Final Report

REPORT DOCUMENTATION PAGE

The public reporting burden for this collection of information is estimated to average 1 hour per response, including the time for reviewing instructions, searching existing data sources, gathering and maintaining the data needed, and completing and reviewing the collection of information. Send comments regarding this burden estimate or any other aspect of this collection of information, including suggestions for reducing the burden, to the Department of Defense, Executive Service Directorate (0704-0188). Respondents should be aware that notwithstanding any other provision of law, no person shall be subject to any penalty for failing to comply with a collection of information if it does not display a currently valid OMB control number.

PLEASE DO NOT RETURN YOUR FORM TO THE ABOVE ORGANIZATION.

1. REPORT DATE (DD-MM-YYYY)	2. REPORT TYPE	3. DATES COVERED (From - To)
12-08-2016	Final Report	15 May 2013 - 14 May 2016

4. TITLE AND SUBTITLE

Understanding the fundamental roles of momentum and vorticity injections in flow control

5a. CONTRACT NUMBER

FA9550-13-1-0183

5b. GRANT NUMBER

5c. PROGRAM ELEMENT NUMBER

6. AUTHOR(S)

Taira, Kunihiko, Phillip Munday, and Aditya G. Nair

5d. PROJECT NUMBER

5e. TASK NUMBER

5f. WORK UNIT NUMBER

7. PERFORMING ORGANIZATION NAME(S) AND ADDRESS(ES)

Florida State University
Sponsored Research Services
874 Traditions Way, Tallahassee, FL 32306-0001

8. PERFORMING ORGANIZATION REPORT NUMBER

9. SPONSORING/MONITORING AGENCY NAME(S) AND ADDRESS(ES)

U.S. Air Force Office of Scientific Research
875 Randolph Street
Arlington, VA 22203

10. SPONSOR/MONITOR'S ACRONYM(S)

AFOSR

11. SPONSOR/MONITOR'S REPORT NUMBER(S)

12. DISTRIBUTION/AVAILABILITY STATEMENT

DISTRIBUTION A: Distribution approved for public release.

13. SUPPLEMENTARY NOTES

14. ABSTRACT

The objective of this study is to numerically investigate the fundamental roles that momentum and vorticity injections play in suppressing flow separation over a canonical airfoil. Open-loop control of separated, incompressible flow over a NACA 0012 airfoil at $Re = 23{,}000$ is examined through large-eddy simulations. We find that the modification to the flow field can be captured by quantifying both the effects of wall-normal momentum (coefficient of momentum) and wall-normal vorticity (derived coefficient of circulation), by considering a newly defined total input parameter (total coefficient). Moreover, the study has developed advanced analysis techniques. First, the capability to perform bi-global stability analysis has been developed and validated, which can serve as a basis for physics-based active flow control guided by the knowledge of hydrodynamic instabilities. Second, as part of modeling complex unsteady flows in general, efforts in this study have led to the initial development of a novel network-theoretic approach in quantifying nonlinear interactions present in vortical flows.

15. SUBJECT TERMS

16. SECURITY CLASSIFICATION OF:			17. LIMITATION OF ABSTRACT	18. NUMBER OF PAGES	19a. NAME OF RESPONSIBLE PERSON
a. REPORT	b. ABSTRACT	c. THIS PAGE			
U	U	U	UU		19b. TELEPHONE NUMBER (Include area code)

Standard Form 298 (Rev. 8/98)
Prescribed by ANSI Std. Z39.18
Adobe Professional 7.0

INSTRUCTIONS FOR COMPLETING SF 298

1. REPORT DATE. Full publication date, including day, month, if available. Must cite at least the year and be Year 2000 compliant, e.g. 30-06-1998; xx-06-1998; xx-xx-1998.

2. REPORT TYPE. State the type of report, such as final, technical, interim, memorandum, master's thesis, progress, quarterly, research, special, group study, etc.

3. DATES COVERED. Indicate the time during which the work was performed and the report was written, e.g., Jun 1997 - Jun 1998; 1-10 Jun 1996; May - Nov 1998; Nov 1998.

4. TITLE. Enter title and subtitle with volume number and part number, if applicable. On classified documents, enter the title classification in parentheses.

5a. CONTRACT NUMBER. Enter all contract numbers as they appear in the report, e.g. F33615-86-C-5169.

5b. GRANT NUMBER. Enter all grant numbers as they appear in the report, e.g. AFOSR-82-1234.

5c. PROGRAM ELEMENT NUMBER. Enter all program element numbers as they appear in the report, e.g. 61101A.

5d. PROJECT NUMBER. Enter all project numbers as they appear in the report, e.g. 1F665702D1257; ILIR.

5e. TASK NUMBER. Enter all task numbers as they appear in the report, e.g. 05; RF0330201; T4112.

5f. WORK UNIT NUMBER. Enter all work unit numbers as they appear in the report, e.g. 001; AFAPL30480105.

6. AUTHOR(S). Enter name(s) of person(s) responsible for writing the report, performing the research, or credited with the content of the report. The form of entry is the last name, first name, middle initial, and additional qualifiers separated by commas, e.g. Smith, Richard, J, Jr.

7. PERFORMING ORGANIZATION NAME(S) AND ADDRESS(ES). Self-explanatory.

8. PERFORMING ORGANIZATION REPORT NUMBER. Enter all unique alphanumeric report numbers assigned by the performing organization, e.g. BRL-1234; AFWL-TR-85-4017-Vol-21-PT-2.

9. SPONSORING/MONITORING AGENCY NAME(S) AND ADDRESS(ES). Enter the name and address of the organization(s) financially responsible for and monitoring the work.

10. SPONSOR/MONITOR'S ACRONYM(S). Enter, if available, e.g. BRL, ARDEC, NADC.

11. SPONSOR/MONITOR'S REPORT NUMBER(S). Enter report number as assigned by the sponsoring/ monitoring agency, if available, e.g. BRL-TR-829; -215.

12. DISTRIBUTION/AVAILABILITY STATEMENT. Use agency-mandated availability statements to indicate the public availability or distribution limitations of the report. If additional limitations/ restrictions or special markings are indicated, follow agency authorization procedures, e.g. RD/FRD, PROPIN, ITAR, etc. Include copyright information.

13. SUPPLEMENTARY NOTES. Enter information not included elsewhere such as: prepared in cooperation with; translation of; report supersedes; old edition number, etc.

14. ABSTRACT. A brief (approximately 200 words) factual summary of the most significant information.

15. SUBJECT TERMS. Key words or phrases identifying major concepts in the report.

16. SECURITY CLASSIFICATION. Enter security classification in accordance with security classification regulations, e.g. U, C, S, etc. If this form contains classified information, stamp classification level on the top and bottom of this page.

17. LIMITATION OF ABSTRACT. This block must be completed to assign a distribution limitation to the abstract. Enter UU (Unclassified Unlimited) or SAR (Same as Report). An entry in this block is necessary if the abstract is to be limited.

Final Report

Understanding the fundamental roles of momentum and vorticity injections in flow control

(FA9550-13-1-0183)

Kunihiko Taira, Phillip M. Munday, & Aditya G. Nair

Mechanical Engineering
Florida State University

August 12, 2016

Abstract

The objective of this study is to numerically investigate the fundamental roles that momentum and vorticity injections play in suppressing flow separation over a canonical airfoil. Open-loop control of separated, incompressible flow over a NACA 0012 airfoil at $Re = 23,000$ is examined through large-eddy simulations. In particular two conditions are considered: (1) $\alpha = 6°$ – shallow stall and (2) $\alpha = 9°$ – deep stall for applications of flow control. This study does not attempt to replicate a specific actuator but aims to independently introduce wall-normal momentum and vorticity flux into the flow through model boundary conditions. We find that the modification to the flow field can be captured by quantifying both the effects of wall-normal momentum (coefficient of momentum) and wall-normal vorticity (derived coefficient of circulation), by considering a newly defined total input parameter (total coefficient). The influence of spanwise spacing is also examined and is shown that the total coefficient accounts for spacing, as long as the actuators are spaced sufficiently far enough to avoid destructive interference. The result from this study is hoped to lead to a general approach for quantifying the control input for a family of actuators.

Moreover, the study has developed advanced analysis techniques. First, the capability to perform bi-global stability analysis has been developed and validated, which can serve as a basis for physics-based active flow control guided by the knowledge of hydrodynamic instabilities. Second, as part of modeling complex unsteady flows in general, efforts in this study have led to the initial development of a novel network-theoretic approach in quantifying nonlinear interactions present in vortical flows. Dense fluid flow graphs, with vortices as nodes and induced velocity as edge weights are distilled to the key structures using spectral sparsification, while preserving nonlinear dynamics and invariants. We have also been able to quantify two-dimensional turbulence as a weighted scale-free network and evaluate its resilience to perturbations. The network-based approach to analyze interactions in fluid flows should provide a refreshing perspective to examine a wide range of unsteady flow phenomena.

Resulting Publications

1. P. M. Munday & K. Taira, "Separation control on NACA 0012 airfoil using momentum and wall-normal vorticity injection," AIAA 2014-2685, 2014.

2. P. M. Munday & K. Taira, "Surface vorticity flux analysis in separation control on NACA 0012 airfoil," AIAA 2015-2632, 2015.

3. A. G. Nair & K. Taira, "Network-theoretic approach to sparsified discrete vortex dynamics," J. Fluid Mech. 768, 549-571, 2015

4. K. Taira, A. G. Nair, & S. L. Brunton, "Network structure of two-dimensional decaying isotropic turbulence," J. Fluid Mech. 795, R2, 2016

Resulting Conference Presentations

1. K. Taira & P. M. Munday, "The role of vorticity injection in separation control." APS DFD, Pittsburgh, 2013.

2. P. M. Munday & K. Taira, "The effects of momentum and vorticity injection for suppressing separation on a NACA 0012 airfoil." APS DFD, San Francisco, 2014.

3. A. G. Nair & K. Taira, "Network-theoretic approach to model vortex interactions." APS DFD, San Francisco, 2014.

4. K. Taira & A. G. Nair, "Sparsified-dynamics modeling of discrete point vortices with graph theory." APS DFD, San Francisco, 2014.

5. A. G. Nair & K. Taira, "Network-based representation of energy transfer in unsteady separated flow," APS DFD, Boston, 2015.

6. K. Taira, A. G. Nair, & S. L. Brunton, "Network structure of two-dimensional homogeneous turbulence." APS DFD, Boston, 2015.

7. K. Taira, A. G. Nair, & S. L. Brunton, "Structure and resilience of two-dimensional fluid flow networks." SIAM Uncertainty Quantification, Lausanne, Switzerland, 2016.

8. A. G. Nair, K. Taira, & S. L. Brunton, "Network-theoretic analyses of vortex dynamics." SIAM Annual Meeting, Boston, 2016.

Contents

Chapter 1

Introduction

Separated flow is a major cause for reduced aerodynamic performance of airfoils at high angles of attack, which leads to drag increase and lift decrease. An airfoil at a high incident requires the oncoming flow to maneuver the leading edge, which creates an adverse pressure gradient along the suction surface, which ultimately results in a separated boundary layer. Such behavior of the boundary layer can be avoided by increasing momentum in the streamwise direction of the flow in order to oppose the adverse pressure gradient. Historically, flow control has been used to avert separated flow and the accompanying detrimental effects (Chang, 1976). Additional momentum can be introduced into the boundary layer either directly or by utilizing free stream momentum to energize the boundary layer (Gad-el-Hak, 2000a). Directly adding momentum to the boundary layer, quite simply, forces the boundary layer in the direction of the free stream. Alternatively, one can utilize the free stream momentum by inducing or enhancing the mixing between the free stream and fluid within the boundary layer to energize the flow near the wall.

1.1 Flow Control

As a means to prevent or delay separation, active and passive flow control actuators can be utilized to introduce perturbations to the flow field (Gad-el-Hak, 2000a; Cattafesta *et al.*, 2008; Joslin & Miller, 2009; Cattafesta & Sheplak, 2011). Active flow control is defined by the addition of external energy to the flow, and can be performed with a large assortment of flow control actuators (Cattafesta & Sheplak, 2011), such devices include steady and unsteady blowing/suction (Lachmann, 1961; Wu *et al.*, 1998), synthetic jets (Glezer & Amitay, 2002), plasma actuators (Corke *et al.*, 2010), and vortex generator jets (Compton & Johnston, 1992; Selby *et al.*, 1992; Zhang, 2003). Passive flow control devices modify the flow without external energy input and include, leading edge modification (Pedro & Kobayashi, 2008; Skillen *et al.*, 2015), vortex generators (VGs) (Kerho *et al.*, 1993; Lin, 2002), and riblets (**?**Choi *et al.*, 1993). The flow control actuators listed above do not encompass all devices that have been developed, but provides an idea of the extent of the variety of actuators in use.

The actuators mentioned above have been implemented in different scenarios to modify separated flows. Such effort has relied mostly on experiments as the studies have often been closely related to actuator development. Seifert & Pack (1999) performed experiments with synthetic jets for flow over NACA 0012 and 0015 airfoils at Reynolds numbers ($1.5 \times 10^6 \leq Re \leq 23.5 \times 10^6$) and Mach numbers ($0.2 \leq M_\infty \leq 0.65$). At post-stall angles of attack ($\alpha \gtrsim 8°$), the reattached flow with control results in approximately 50% increase in lift and 50% decrease in drag. More recently, Rathay *et al.* (2014*a*,*b*) and Seele *et al.* (2012, 2013) increased side force on scaled vertical tail stabilizer using synthetic jet actuators and sweeping jet actuators. The former studies laid the foundation for a successful full-scale flow control on a vertical tail using sweeping jet actuators (Whalen *et al.*, 2015) and eventual implementation on the Boeing ecoDemonstrator 757. In another study, Little *et al.* (2010) used a dielectric barrier discharge plasma actuator to modify the separation due to the deflection flap of a high-lift airfoil at $Re = \mathcal{O}(10^5)$. Effects of control, which include delaying separation as well as lengthening and flattening the separated region, were dependent on the waveform of the control input.In the same spirit, using micro-vortex generators, Lin *et al.* (1994) reduced flap separation over a three-element airfoil in high-lift configuration. By mitigating separation, the lift-to-drag ratio is doubled. The effectiveness of the sub-boundary layer vortex generators is highly dependent on the geometry, spacing, height, and angle. With the aforementioned control approaches, flow separation is mitigated with different actuators but often leveraging similar control mechanisms. The large number of studies in separation control have given emergence to different types of non-dimensional parameters (e.g., momentum coefficient, swirl coefficient, blowing ratio) used to report the control input for each device.

The difficulty in analyzing the flow through experiments is caused by the complex three-dimensional nature of separated flow under the influence of control with a wide range in spatial scales being present in the flow field. For the same computational analysis of flow control at moderate Reynolds number also requires substantial resource to perform a sizable number of parameter study with high fidelity. While challenging and computationally expensive, numerical simulations have also been performed to study flow control on NACA airfoils. In addition to resolving the baseline conditions at Reynolds numbers similar to experiments, replicating an actuator introduces added complexity (Raju *et al.*, 2009). Earlier numerical studies have examined the effectiveness of blowing/suction (Wu *et al.*, 1998; Huang *et al.*, 2004) and vortex generators (Shan *et al.*, 2008). More recently, high-fidelity, three-dimensional LES of complex interactions between the flow over the airfoil and synthetic jet actuation have been performed by You *et al.* (2008) at $Re = 896,000$ including the internal actuator geometry. These types of complex interactions were further investigated by Abe *et al.* (2013) at $Re = 63,000$, in which the perturbations with different spanwise wavelengths were considered to model internal effects of the synthetic jet. Based on this study, Sato *et al.* (2015) modeled the effects of plasma actuators and performed a parametric sweep to determine cases for separation mitigation. These studies highlighted the difficulty in replicating and modeling the influence of specific actuator inputs.

Regardless of the selected type of actuator, we can view the flow to be affected by

means of mass, momentum, energy, and vorticity injections. Active flow control actuators can in an obvious manner add the aforementioned forcing inputs. In contrast, passive flow control actuators introduce perturbations in response to the flow negotiating the actuator geometry. Instead of simulating flow control using each and every type of actuator, we aim to understand the response of the separated flow to fundamental control inputs that these actuators add. The present investigation is of the influence of wall-normal momentum and vorticity injections for separated flow over a NACA 0012 airfoil at 9° for $Re = 23,000$. The three-dimensional LES herein sheds light on the separated flow physics and identify the key actuation mechanism for reattaching the flow at high angles of attack.

1.2　Vortical Interactions

As part of modeling and quantification efforts on nonlinear interactions in complex fluid flows, we consider novel approaches. In particular, we extend network analysis (Newman, 2010) and graph theory (Bollobás, 1998) to canonical examples of point-vortex dynamics and two-dimensional turbulence, as an initial attempt to develop these network based techniques.

In the field of fluid mechanics, there have been extensive studies performed to capture the behavior of complex fluid flow. Lagrangian based methods, such the vortex methods, allow us to simulate the unsteady fluid flow (Leonard, 1980; Cottet & Koumoutsakos, 2000). These methods involve modeling of fluid flow with point vortices, vortex sheets, vortex filaments or vortex patches (Saffman, 1992; Cottet & Koumoutsakos, 2000). Low-order representation of these vortex models (Wang & Eldredge, 2013; Hemati *et al.*, 2014) have been proposed in recent years. The evaluation of the velocity field for vortex methods rely often on fast summation methods (Greengard & Rokhlin, 1987) for reduced computational time. In the present work, we use network-theoretic approach to capture the behavior of vortical elements involved in complex fluid flows.

As the computational approaches for vortex dynamics are being developed, there are also ongoing efforts in flow modeling. Reduced-order models have been utilized successfully to describe unsteady incompressible and compressible flows (Rowley *et al.*, 2004; Noack *et al.*, 2005). One such approach is to utilize Galerkin projection to derive reduced-order models using spatial bases such as the Proper Orthogonal Decomposition (POD) modes (Berkooz *et al.*, 1993; Holmes *et al.*, 1996). The reduced-order model distills the infinite-dimensional Navier-Stokes equations to model equations with state variables having significantly reduced dimensions. In the present work, we also aim to capture the essential physics of unsteady fluid flow but not by reducing the dimension of the state variable. Instead, we examine the interaction between the elements of the state variables and *sparsify the interactions* utilizing a network-theoretic approach. We refer to the dynamical model based on sparsifying the interactions as *sparsified dynamics* in this paper.

Network describes how components are linked to one another. We can represent the components by points (nodes) and the connections by lines (edges) through a mathematical abstraction. The structure comprised of these nodes and edges is called a graph, which has been studied in detail in the field of graph theory (Bollobás, 1998). Network analysis is

concerned with the study of graphs as well as the interaction and evolution of the variables of interest on graphs over time and space (Newman, 2010). The framework developed in network analysis and graph theory can provide insights into how the structure of a network can influence the overall dynamics taking place on the network. Network analysis and graph theory by nature are very fundamental and generic, which enable them to impact a wide range of applications, including the analysis of biological and social networks, study of traffic flows, and design of robust power grids (Newman, 2010). Biologists and medical scientists use network analysis to determine how electrical signals travel inside the brain and how abnormality in the brain network connections can affect the normal functionality (Duarte-Cavajalino *et al.*, 2012; Owen *et al.*, 2013).

In epidemiology, researchers model the outbreak of diseases on the population network. Locations with high concentration of population, such as airports, stations, schools, and hospitals, can be represented on a network with large number of connections. Identifying such locations is especially critical when containment measures are designed to control outbreaks of HIV (Morris, 1993), SARS (Lloyd-Smith *et al.*, 2005), and Influenza (Glass *et al.*, 2006; Cauchemeza *et al.*, 2011). Each of these diseases have different dynamics and an associated network structure. Once the high-risk groups and areas are identified, network analysis can assist in designing and implementing prevention and combat strategies in the most swift manner with limited resources (Salathé & Jones, 2010; Robinson *et al.*, 2012). Network analysis can also reveal how a group of people are socially connected to one another and examine how subgroups within a population are interlinked in a complex manner (Porter *et al.*, 2005). Moreover, network analysis has been utilized in electrical engineering to determine the voltages and currents associated with electrical circuits via graph representations (Chen, 2004). In the aforementioned applications of network analysis, the connections between people or elements are highlighted.

In the present work, we consider representing vortices with nodes and the interactions amongst the vortices with edges. By utilizing the network-theoretic framework to study vortex dynamics, we highlight the connections (edges) that the vortices have in the flow field. Such analysis emphasizes how a collection of vortices influence each other through a causal point of view on a network structure. We believe that the present study can provide an alternative tool to analyze how vortices or flow structures interact in the flow field and support the development of interaction-based models to capture unsteady vortex dynamics. Furthermore, we consider the use of graph sparsification as a tool for sparsifying the interaction between the point vortices. These models keep the nodes intact and reduce the number of edges maintaining the dimensionality of the original system unlike reduced-order models. The removal of edges can drastically reduce computational cost to model the full dynamical behavior, sharing the same spirit as reduced-order models.

The chaotic motion of a large number of vortices in turbulent flows is caused by the induced velocities of the vortices themselves. What makes turbulence rich and complex are the vortical interactions in the flow field that take place over a wide range of length scales (Tennekes & Lumley, 1972; Hinze, 1975; Frisch, 1995; Pope, 2000; Davidson, 2004; Lesieur, 2008). Thus, complete understanding of turbulence has remained a challenge to this day

because of its high-dimensionality, multi-scale interactions, nonlinearity and the resulting chaos. Network science provides an alternative view of complex fluid flows in terms of a network of vortex interactions (Nair & Taira, 2015), and this perspective illuminates the underlying structure and organization of turbulent flows. In this work, we show that two-dimensional isotropic turbulence (Kraichnan & Montgomery, 1980; McWilliams, 1984; Benzi et al., 1990; Benzi & Colella, 1992; Davidson, 2004; Boffetta & Ecke, 2012) has a scale-free network structure reminiscent of other networks found in nature (Barabási & Albert, 1999; Caldarelli, 2007). While most of the attention has been placed on unweighted scale-free networks, we consider the use of weighted scale-free network to describe the variations in the strength of interactions or connectivities (Barrat et al., 2004). Upon identifying the network structure of turbulence, physical insights can be obtained as to which vortical interactions are important in capturing the overall physics and how it may be possible to control the dynamics of turbulent vortices (Liu et al., 2011; Farazmand et al., 2011; Brunton & Noack, 2015).

1.3   Structure of This Report

The remainder of this report is organized as follows. We present the computational approach and the flow control setup in section 2. Section 3 details the influence of control on the separated flow, with focus on vortex dynamics. With the understanding of flow control effects on the flow, we quantify control inputs in section 4 and are related to the change in aerodynamic forces. The flow control findings are broadly categorized using non-dimensional parameters based on the control inputs. We perform global stability analysis in section 5. We highlight network analysis methodology in section 6 and quantify the vortical interaction in section 7. We extend the network analysis to quantify turbulent flow interactions in section 8. We end this paper with concluding remarks.

Chapter 2

Flow Control Simulation Approach

2.1 Simulation Setup

We perform large-eddy simulations (LES) of flow over a NACA 0012 airfoil using an in-compressible flow solver, `Cliff` (`CharLES` software package, Cascade Technologies; Ham & Iaccarino (2004); Ham *et al.* (2006)). The incompressible Navier–Stokes equations are discretized using the second-order finite-volume and time-integration schemes. Incorporating energy conservation properties (Morinishi *et al.*, 1998), the solver is capable of handling structured and unstructured grids. In the present computation, we define the Reynolds number as $Re = U_\infty c/\nu = 23,000$, which is based on the free stream velocity, U_∞, the chord length of the airfoil, c, and the free stream viscosity, ν. To predict the flow field at this Reynolds number, eddy viscosity is introduced with the Vreman subgrid-scale model (Vreman, 2004). We investigate the influence of control of fully separated flow at $\alpha = 9°$ for the purpose of increasing lift and reducing drag.

The overall size of the computational domain is $(x/c, y/c, z/c) \in [-20, 25] \times [-20, 20] \times [-0.1, 0.1]$, as illustrated in Fig. 2.1. The spatial directions x, y, and z refer to the streamwise, wall-normal, and spanwise directions, respectively. At the inlet, laminar, uniform flow of $\boldsymbol{u}/U_\infty = (1, 0, 0)$ is prescribed. Stress-free boundary conditions are applied at the far-field (top and bottom) boundaries. A convective outflow condition, $\frac{\partial \boldsymbol{u}}{\partial t} + U_c \frac{\partial \boldsymbol{u}}{\partial \hat{n}} = 0$, is prescribed at the outlet, with the convective velocity (U_c) set to the time-averaged normal velocity, to allow wake structures to leave the domain without disturbing the near-field solution. In the spanwise direction, flow is taken to be periodic.

The present study utilizes a hybrid structured/unstructured spatial discretization. A structured grid is used to achieve adequate resolution in the near field of the airfoil and an unstructured far-field grid utilized to reduce the number of points needed in this region of the computational domain. The mesh is planar (two-dimensional) and extruded in the spanwise direction. The computational domain in the vicinity of the actuators is also refined in order to resolve the fine-scale flow structures produced by interaction of the incoming flow and the actuator inputs. Based on the domain size and necessary spatial resolution, the resulting computational domain is comprised of approximately 40×10^6 grid points.

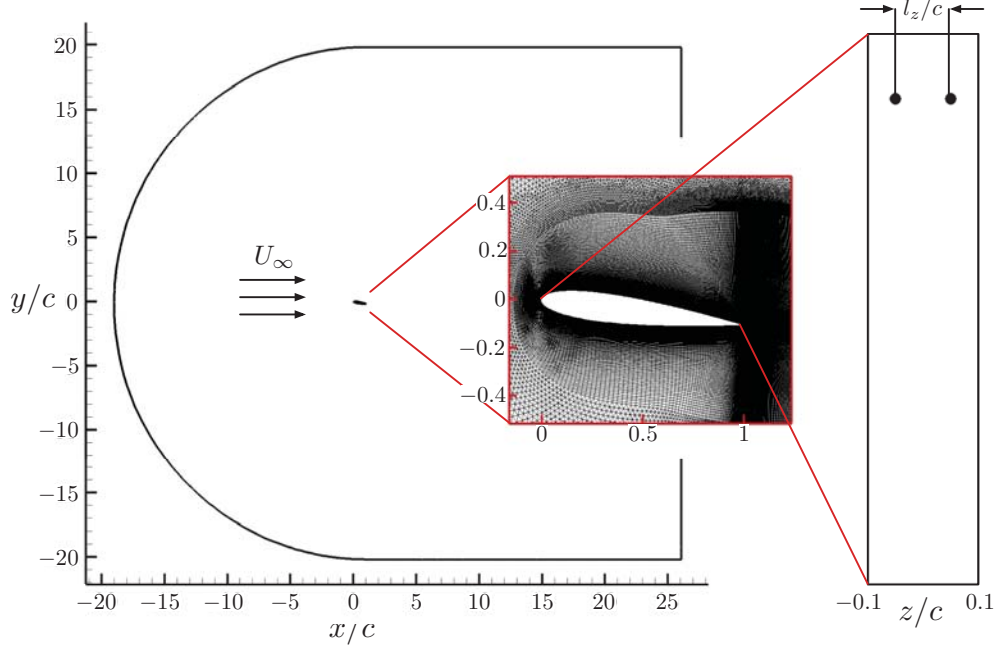DISTRIBUTION A: Distribution approved for public release.

Figure 2.1: Computational domain used for the LES, with the background flow directed from left to right. A top down view to the right shows the airfoil with two actuators over the spanwise extent.

To perform wall-resolved LES in the present investigation, sufficient resolution is needed near the airfoil surface. The largest non-dimensional wall spacing along the suction surface of the airfoil is $x^+ \approx 6$, $y^+ \approx 0.5$, and $z^+ \approx 12$ ($\boldsymbol{x}^+ \equiv u_\tau \boldsymbol{x}/\nu$, where u_τ is the friction velocity). No slip, no penetration boundary conditions are applied on the airfoil surface. The surface mesh of the airfoil is refined such that 30 points span across each actuator, which we describe in detail below in Section 2.2. For the controlled cases, an actuator velocity profile, to be discussed later, is specified at the actuator locations on the surface of the airfoil. As shown in Fig. 2.1, the spanwise actuator spacing is set to $l_z/c = 0.1$ for the majority of the present study. Later in this paper, we consider using 1 to 4 actuators ($l_z/c = 0.2$ to 0.05) over the span of 0.2 to examine the influence of spanwise spacing on control effectiveness.

Throughout this paper, the lift, drag, and pressure coefficients are defined as

$$C_L \equiv \frac{F_L}{\frac{1}{2}\rho_\infty U_\infty^2 A}, \quad C_D \equiv \frac{F_D}{\frac{1}{2}\rho_\infty U_\infty^2 A}, \quad \text{and} \quad C_P \equiv \frac{p - p_\infty}{\frac{1}{2}\rho_\infty U_\infty^2}, \tag{2.1}$$

where $A = l_z c$ is the planform area of the airfoil, and ρ_∞ is the free stream density. The forces, F_L and F_D, represent lift and drag, respectively. The coefficient of pressure subtracts off the free-stream pressure value p_∞ and is normalized by the dynamic pressure. The forces produced by control are included in the reported lift and drag values.

To ensure the validity of our computational approach, we compare our computational results for the baseline flow with those reported in Kojima *et al.* (2013). Upon examining

the flow field, airfoil pressure distribution, and forces, we observe good agreement as they have been reported in detail in our prior publications (Munday & Taira, 2014, 2015). Moreover, the computational requirements for the computational domain size, boundary condition treatment, and grid resolution were examined with care. With the separated flow validated, we now consider the applications of flow control to mitigate separation.

2.2 Actuation Setup

We introduce steady circular jets with swirl on the suction surface of the airfoil specified by velocity boundary conditions. A canonical setup for the actuators is shown in Fig. 2.1 (right). The actuator jets are specified by circular regions with a radius of $r_0/c = 0.01$ and placed at 10% chord location. This is the typical actuator location used in the majority of the cases, but we also report the influence of the spanwise spacing and chordwise placement (herein the chordwise direction is defined as ξ). In particular, we consider 1 to 4 actuators across the spanwise extent. In order to assess the influence of the injection of wall-normal momentum and wall-normal vorticity independently, wall-normal (u_n) and azimuthal velocity (u_θ) profiles are specified. At the actuator locations, the time-invariant velocity profiles are

$$\frac{u_n}{u_{n,\max}} = 1 - \left(\frac{r}{r_0}\right)^2, \quad \frac{u_\theta}{u_{\theta,\max}} = 4\left(1 - \frac{r}{r_0}\right)\frac{r}{r_0}, \tag{2.2}$$

which are plotted in Fig. 2.2. For simulations with multiple actuators over the spanwise extent of the computational domain, we consider arrangements where swirl is introduced in a co-rotating or counter-rotating manner. Throughout the paper, we denote co-rotating cases with COR and counter-rotating ones with CTR, respectively. The magnitude of wall-normal velocity is chosen such that the coefficient of momentum is on the same order of magnitude as in previous successful studies (Greenblatt *et al.*, 2015). The azimuthal velocity is selected such that the maximum velocity is on the same order of magnitude as the free stream, which is the upper bound for vortex generators.

To examine the fundamental influence of the above actuation inputs on separated flow over the airfoil, we consider a large number of flow control cases. We considered control at $\alpha = 6°$ and $\alpha = 9°$ and a summary of all the controlled cases are tabulated in Appendix A.1 and A.2, respectively. In the tables, all of the control input values are listed along with the resulting force coefficients. Also listed in the appendix is the total coefficient which will be defined and discussed in detail in Section 4. In what follows our discussion pertains to $\alpha = 9°$. In the present study, we keep our actuation inputs to be steady to limit the numbers of parameters and LES computations to be tractable.
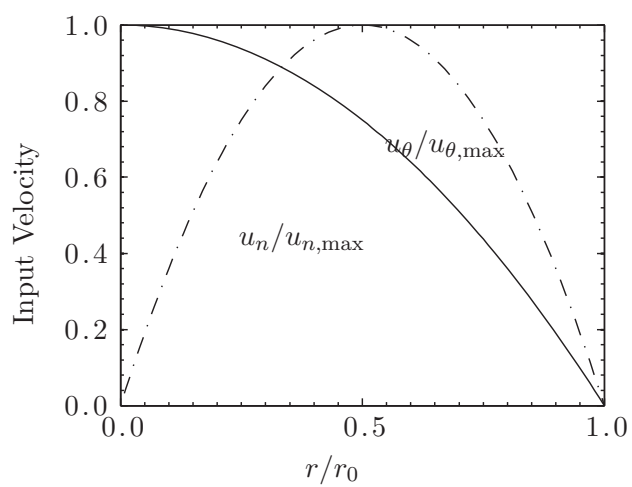
Figure 2.2: Prescribed velocity profiles for flow control inputs.

Chapter 3

Flow Physics

In this section, we examine the flow field for both uncontrolled and controlled cases in detail. At an angle of attack of $\alpha = 9°$ and $Re = 23,000$, flow separates near the leading edge and does not reattach which is consistent with results of similar studies (Chang, 1976; Kotapati et al., 2010; Kojima et al., 2013). First, we discuss how the separated flow will be evaluated

3.1   Flow Visualization

To highlight the effect of control input on the flow field, the time-averaged zero-streamwise-velocity ($u_x = 0$, herein) iso-surface is visualized. By definition, separated flow is accompanied by reverse flow. The $u_x = 0$ iso-surface encompasses the reverse flow region and is used here to capture separation and reattachment. While the $u = 0$ surface provides a general sense of the size of the separated region, it does not encompass and should not be considered as the entirety of a separated boundary layer. We also superpose the spanwise Reynolds stress distribution on the $u_x = 0$ iso-surface to provide insights into turbulent mixing of near-wall and free stream momentum. The spanwise Reynolds stress is defined as $\tau_{xy} \equiv \rho \overline{u'_x u'_y}$, which is based on the fluctuations in the x and y-directions, u'_x and u'_y, respectively. Visualizing the Reynolds stress identifies locations in which turbulent mixing is enhanced to aid in reattachment with control input. Figure 3.1, illustrates the $u_x = 0$ iso-surface for the baseline case. The images in Fig. 3.1 are of the time-averaged flow fields, and the red line highlights the locations of the $u_x = 0$ iso-surface amongst the time-averaged streamlines. For the baseline flow, the time-averaged results are homogeneous throughout the spanwise direction. Identifying locations of reversed flow throughout the span will help in understanding the effects of control input later.

For incompressible flow, vorticity can only be generated along the wall surface or injected by the control inputs. Vorticity is introduced to the flow through a wall-normal diffusive flux at the surface

$$\nu(\nabla \boldsymbol{\omega})_0 \cdot \hat{n} = -\hat{n} \times \left[\frac{d\boldsymbol{u}}{dt} + \frac{1}{\rho} \nabla p \right]_0, \tag{3.1}$$

which is caused by the acceleration of the wall and the local pressure gradient in the tangential
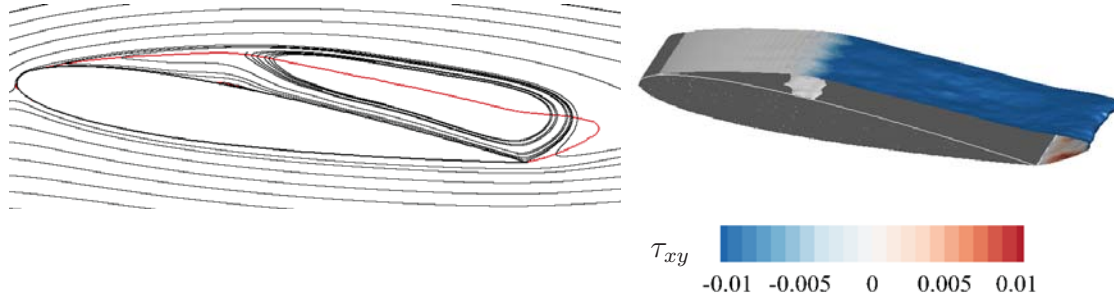
14

Figure 3.1: Time-averaged streamlines (black) and the zero-streamwise-velocity ($u_x = 0$) curve (red) on the left. The zero-streamwise-velocity iso-surface colored with Reynolds stress is to the right.

direction (Hornung, 1989; Wu *et al.*, 2006). Here, the subscript zero denotes the surface value and $\hat{n}$ represents the wall-normal unit vector. Since the wing is assumed stationary in the present study, only the pressure gradient attributes to the above flux. This wall-normal diffusive flux is referred to as the source of vorticity (Hornung, 1989) and is denoted by $\boldsymbol{\sigma} \cdot \hat{n}$

$$\boldsymbol{\sigma} \cdot \hat{n} = (\sigma_x, \sigma_y, \sigma_z)^T = \nu(\nabla\boldsymbol{\omega})_0 \cdot \hat{n}, \qquad (3.2)$$

The subscripts of σ_i refer to the directions of the wall-normal flux components. Throughout the study, time-averaged σ_i are shown to closely examine the local influx and efflux of vorticity in the separated region of the flow.

The spanwise vorticity flux for the baseline case is shown in Fig. 3.2. Negative spanwise vorticity flux is observed upstream of the separation location as the boundary layer negotiates the leading edge. Flow maneuvering the curvature of the leading edge causes a pressure gradient in the streamwise direction, which is correlated to regions with increased spanwise vorticity flux. Additionally, near the reattachment location, an increase in spanwise vorticity flux in the same direction (seen in red) is observed. The spanwise vorticity flux at the reattachment location is introduced due to the pressure gradient, as shown in Fig. 3.2. Time-averaged quantities are used, therefore the streamwise and wall-normal vorticity flux are zero for the baseline cases. Through this analysis, emphasis will be placed on the separation and reattachment location (if present), as well as near the actuators to observe the effects control has on the vorticity flux.

3.2 Separation Control

Baseline Flow

Now, let us consider the separated flow over the NACA 0012 airfoil. Flow over the airfoil at this higher angle of attack separates from the leading edge and does not reattach over the chord as seen in Fig. 3.3 (top). A shear layer develops at the leading edge and generates

σ_z

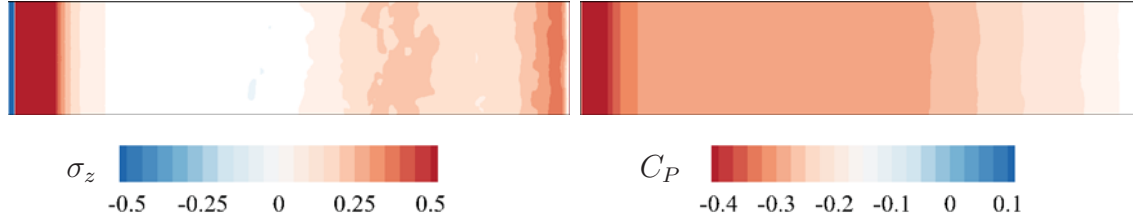-0.5 -0.25 0 0.25 0.5

C_P

-0.4 -0.3 -0.2 -0.1 0 0.1

Figure 3.2: Spanwise vorticity flux on the suction surface of the airfoil for the baseline flow case. Surface pressure profiles for the corresponding cases are shown on the right.

Case	$u_{n,max}/U_\infty$	$u_{\theta,max}/U_\infty$	C_μ	C_Γ	Rot. dir.	C_D	C_L
Baseline	0	0	0	0	–	0.118	0.584
9A	1.26	0	0.44%	0	–	0.108	0.403
9B	1.26	0.95	0.44%	2.29%	CTR	0.094	0.483
9C	1.26	1.26	0.44%	2.60%	COR	0.065	0.671

Table 3.1: Representative flow control cases for $\alpha = 9°$ chosen for flow visualization in Fig. 3.3.

large spanwise vortices. The breakdown of these vortices leads to turbulent flow past the mid-chord of the airfoil. The $u_x = 0$ iso-surface covers the entire suction surface of the airfoil, even extending downstream into the wake. The resulting large region of reverse flow is detrimental to the aerodynamic forces on the airfoil. At the trailing edge bluff body shedding is observed, which is noted by the large-scale, opposite sign vortices. Spanwise Reynolds stress on the $u_x = 0$ iso-surface shows the development of a large turbulent wake with the breakdown of the spanwise vortex. Through the investigation of the vorticity flux on the surface of the airfoil. A high level of spanwise vorticity flux is observed near the leading edge and is correlated to a strong pressure gradient caused by the curvature of the airfoil. Since there is no reattachment, no other large influxes of vorticity are observed downstream of the separation location.

In an attempt to reattach the massively separated flow over the airfoil at $\alpha = 9°$, actuation with wall-normal velocity of $u_{\text{n,max}}/U_\infty = 0$ to 1.83 and azimuthal velocity values of $u_{\theta,max}/U_\infty = 0$ to 2.52 is considered. The actuator location is based on the separation point for the $\alpha = 6°$ case ($\xi/c = 0.1$). For the angle of attack of $\alpha = 9°$, the actuator is located downstream of the separation point (we later examine the effect of moving the actuator to the separation point at $\xi/c = 0.05$). Three representative control cases for $\alpha = 9°$ are listed in Table 3.1, and we note that the aerodynamic forces can be altered significantly, up to 36% reduction in drag and 31% increase in lift with appropriate control inputs.

With only pure blowing (case 9A, $u_{n,max}/U_\infty = 1.26$) flow control negatively impacts lift. In Fig. 3.3 we observe that the separated flow is not modified much by this control configuration. Comparing case 9A to the baseline flow, the size of the separated region increases in the wake. Although a deficit in the reverse flow is created in the vicinity of the

actuator for case 9A, flow eventually separates throughout the span. We found solely adding momentum with a wall-normal velocity of $u_{n,max}/U_\infty = 1.26$ is not effective in overcoming the adverse pressure gradient throughout the span/chord. The most notable difference in the instantaneous flow profiles of the pure blowing case is the spanwise vortex is no longer present. The actuator jets show the Kelvin-Helmholtz instability which interacts with the separated shear layer. This results in the spanwise vortex break down close to the leading edge. The Reynolds stress on the iso-surface is of lower level than that observed for the baseline case. The reduced amount of turbulent mixing from the actuator perturbation does not result in reattaching flow. We observe secondary surface vorticity flux with case 9A due to obstruction and resulting pressure gradients created by the actuator. Due to the flow separating upstream of the actuator, flow is not forced between the actuators as drastically as the lower angle of attack, which increased momentum between the actuators for the previous angle of attack.

Next, let us introduce swirling motion to the control jets. As shown in Fig. 3.3, the combination of wall-normal momentum and vorticity injections (cases 9B and 9C) can greatly modify the time-averaged flow field. Cases 9B and 9C use azimuthal actuator velocity profiles with $u_{n,max}/u_\infty = 0.95$ and 1.26, respectively. For these two cases, the addition of wall-normal vorticity and wall-normal momentum decrease the size of the reverse flow region. For case 9B, flow still separates near the leading edge of the airfoil and reattaches in the vicinity of the actuator, forcing the oncoming flow to be redirected closer to the airfoil. Overall, the resulting size of the separated flow region is noticeably smaller. The change in the time-averaged flow field is reflected in the forces; drag is further decreased and lift increased compared to pure blowing with identical wall-normal velocity input. Once again, the large structures emanating from the actuators seen in the pure blowing case are broken into smaller structures when rotation is added to actuation.

Fully reattaching the flow with the same wall-normal momentum requires additional wall-normal vorticity input. The control input with $u_{n,max}/u_\infty = 1.26$ and $u_{\theta,max}/u_\infty = 1.26$ by case 9C results in a fully attached boundary layer. This fully attached case translates to significant improvements in terms of aerodynamic forces. In case 9C we observe in Fig. 3.3 (bottom) the reverse flow region is diminished downstream of the actuators. Although flow separates upstream of the actuators, but the momentum added to the boundary layer by the actuators allows for the flow to overcome the adverse pressure gradient. The wall-normal momentum penetrates the boundary layer and transports injected vorticity into the shear layer, mixing the free stream momentum and boundary layer. Minimal Reynolds stress is observed on the $u_x = 0$ iso-surface, which indicates the large scale vortical structures produced by the actuators are responsible for reattachment. The combination of momentum and vorticity injection reattaches the flow over the airfoil in this configuration. Spanwise vorticity flux observed downstream of the actuators correlates to a reattached boundary layer. It should be observed that σ_z contour plot for case 9C shows a desirable profile over the entire top surface, resulting in a favorable pressure gradient (attached flow) achieved by the control inputs with wall-normal momentum and vorticity.

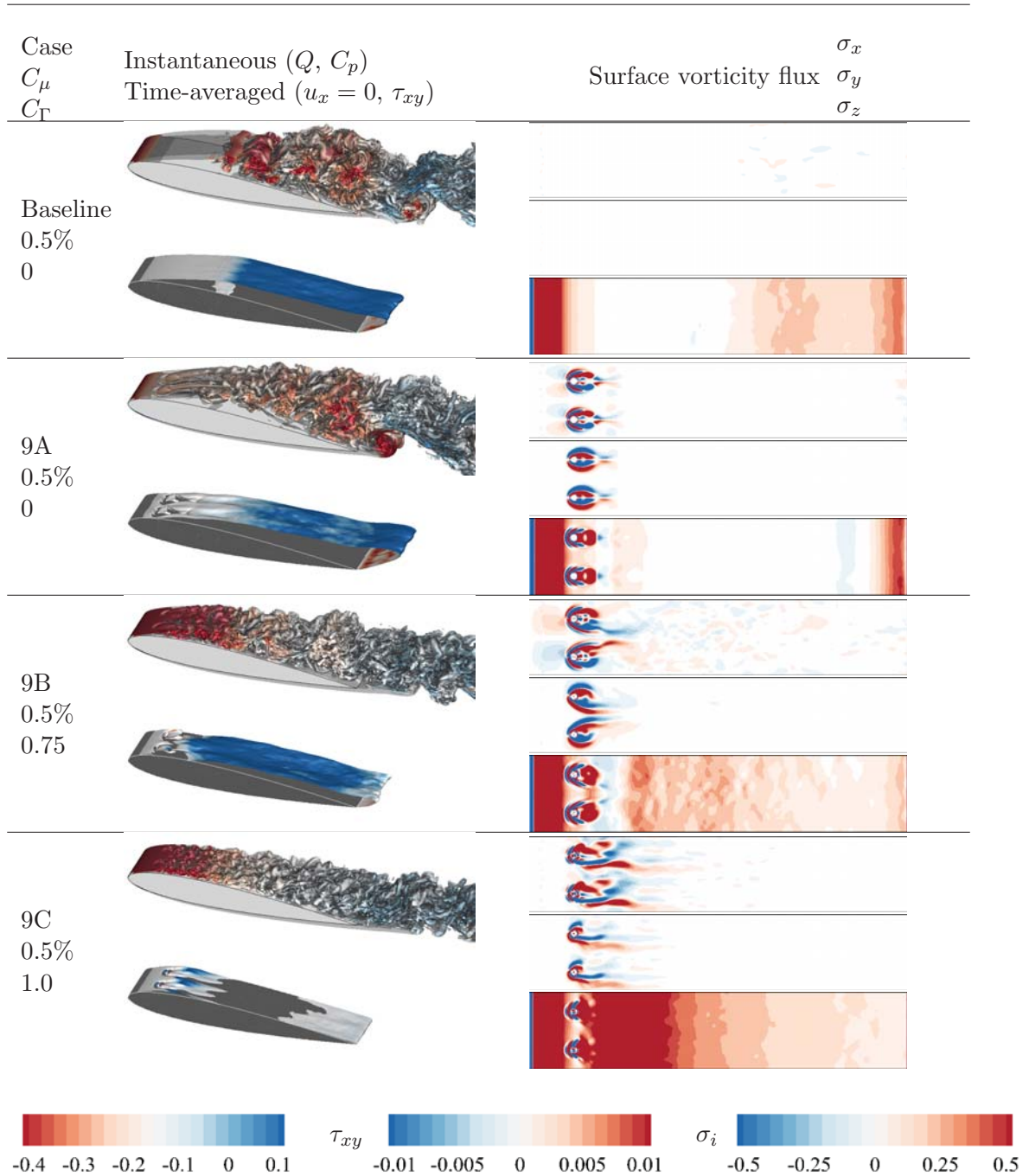Controlling the flow at $\alpha = 9°$ requires both wall-normal momentum and vorticity injec-

Case C_μ C_Γ	Instantaneous $(Q,\ C_p)$ Time-averaged $(u_x = 0,\ \tau_{xy})$	Surface vorticity flux	σ_x σ_y σ_z
Baseline 0.5% 0			
9A 0.5% 0			
9B 0.5% 0.75			
9C 0.5% 1.0			

C_P -0.4   -0.3   -0.2   -0.1   0   0.1

τ_{xy} -0.01   -0.005   0   0.005   0.01

σ_i -0.5   -0.25   0   0.25   0.5

Figure 3.3: For each case at $\alpha = 9°$, the instantaneous flow field (top left) is shown with Q-criterion colored with pressure. The time-averaged zero-streamwise velocity $(u_x = 0)$ iso-surface is colored with spanwise Reynolds stress τ_{xy} (bottom left). Visualized on the right are the wall-normal vorticity flux components in the streamwise (top), wall-normal (middle), and spanwise (bottom) directions.

tions to reattach to the flow based on the representative cases considered above. Flow control with only wall-normal momentum input (case 9A) perturbed the shear layer, but does not significantly impact the separated wake. The addition of wall-normal vorticity reduces the size of the separated flow region. From case 9B with $u_{\theta,\mathrm{max}}/U_\infty = 0.95$, we observe a decrease in the size of the separated flow region. Furthermore, in case 9C with $u_{\theta,\mathrm{max}}/U_\infty = 1.26$, separation is minimized downstream of the actuators resulting in 37% drag decrease and 31% lift increase. With all the cases examined herein, we summarize the influence of flow control inputs in terms of the aerodynamic forces experience by the NACA 0012 airfoil in the following sections.

Chapter 4

Control Input Quantification

Using the knowledge gained from the flow fields in the previous section let us further elaborate on the flow physics and quantify the momentum introduced to the boundary layer as a function of actuator input parameters. To describe the control input, we will use the wall-normal and azimuthal velocities input by the actuators as well as the geometry of the actuator. We separate the effects of momentum directly input into the boundary layer, and momentum introduced to the boundary layer by streamwise vortices, which we identify as the coefficient of momentum and coefficient of circulation. Combining these two coefficients results in what we will refer to as the total coefficient. Using the following quantification should create a push for thorough bench-top characterization of different actuators, thus allowing all actuators to be compared in a similar manner. After defining the input parameters, we examine the resulting aerodynamic forces based on these coefficients. For all results presented, force induced by the actuator is included in the reported forces.

4.1   Coefficient of Momentum

The influence of momentum directly added to the boundary layer is quantified strictly with the wall-normal velocity component and actuator radius. By convention, we use the momentum coefficient which is the ratio between the momentum input by the actuator to the momentum of the free stream. For the wall-normal velocities discussed above, the momentum added was not adequate to reattach the separated flow. We observed in the following section, increasing the wall-normal velocity eventually reattaches the flow. The normal velocity used in this study result in coefficient of momentum $\mathcal{O}(0.1\% - 1\%)$, which is of similar magnitude successfully implemented by previous studies for control over symmetric airfoils (Deng *et al.*, 2007; Gilarranz *et al.*, 2005; Seifert & Pack, 1999; You *et al.*, 2008). Next the forces are plotted with versus the coefficient of momentum.
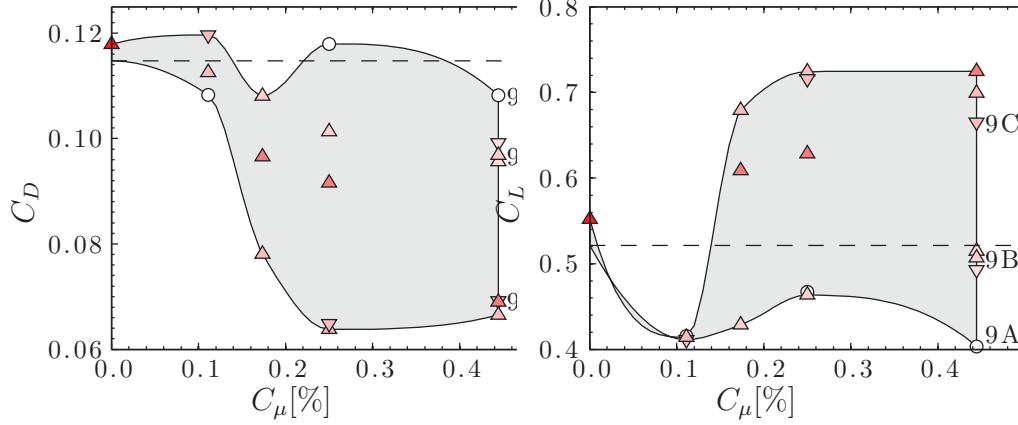
Figure 4.1: The coefficients of drag (left) and lift (right) versus the coefficient of momentum. The baseline value is indicated by ---- and the controlled cases are pure blowing, ○, co-rotating, ▽, and counter-rotating, △.

4.1.1 Force Coefficient

The resultant drag and lift forces versus the coefficient of momentum are plotted in Fig. 4.1. The information contained in Fig. 4.1 is as follows; first we distinguish between pure blowing (○), co-rotating jets (▽), and counter-rotating jets (△). Coefficient of momentum is only quantified by wall-normal velocity, therefore we color the rotating jet cases with the azimuthal velocity. Additionally, overlaid on these plots is a region of influence, in which we encompass the resultant forces obtained from this study. The region of influence aids in understanding the effect of the coefficient of momentum by highlighting the range of forces attained for each coefficient of momentum.

When flow passes over the airfoil at $\alpha = 9°$ and $Re = 23,000$, the drag forces show a generally decreasing trend. The change in drag force is minor ($\Delta C_D \approx 0.04$), but the percentage change is fairly drastic ($\Delta C_D \approx 35\%$). While almost all of the cases reduced drag on the airfoil, lift enhancement is achieved with appropriate control input. For coefficients of momentum $0.15 \lesssim C_\mu[\%] \lesssim 0.45$, the addition of wall-normal vorticity influences the resulting flow. In general, for a constant coefficient of momentum ($0.15\% \lesssim C_\mu$), increasing u_θ is correlated to increasing lift and decreasing drag. For example, cases 9A, 9B, and 9C all use the same momentum coefficient, we observe that increasing azimuthal velocity or swirl input by the actuator increases lift and decreases drag. This trend is noted by the diminishing size of the reverse flow region, which was noted when comparing cases 9A, 9B, and 9C.

From these figures we ascertain that a wall-normal velocity $u_n/U_\infty > 0.625$ effectively injects the wall-normal vorticity into the flow. The region of influence illustrates this point, it is thin for small momentum coefficients ($u_n/U_\infty < 0.625$). It appears that for these wall-normal velocities, the swirl added to the boundary layer is not injected near the edge of boundary layer which would be most effective to mix the free-stream and boundary layer.

The gray region widens with increasing coefficient of momentum, and now the vorticity is being injected further into the flow by the wall-normal momentum. The width of the region of influence eventually saturates and is not modified by the larger momentum coefficients plotted in Fig. 4.1. An upper limit of drag decrease and lift increase appears to be achieved for cases with $C_\mu > 0.25$, and wall-normal vorticity. Next, let us define the coefficient of circulation and evaluate the forces as a function of the coefficient of circulation.

4.2 Coefficient of Circulation

Considering the previous discussion, we would like a variable similar to the coefficient of momentum to describe the circulation input to the flow. In the previous section we noted that the combination of wall-normal momentum and swirl reattached the flow. The increasing wall-normal velocity was needed to advect the vorticity further into the boundary layer. We note that an alternative form of the coefficient of momentum is the dot product of the non-dimensional mass flow rate $(\overline{m}_j/U_\infty A)$ and the blowing ratio (R), $C_\mu = \dot{\overline{m}}_j \overline{u}_j / 0.5 U_\infty^2 l_z c$. Therefore, with a similar thought process, we multiply the non-dimensional mass flow rate with the ratio of the azimuthal velocity to the free-stream velocity. This term will be denoted as the coefficient of circulation (C_Γ) and defined as

$$C_\Gamma = \frac{\dot{\overline{m}}_j \overline{u}_\theta}{\frac{1}{2} U_\infty^2 A} = \frac{\overline{u}_n \pi r_0^2 \overline{u}_\theta}{\frac{1}{2} U_\infty^2 A}, \tag{4.1}$$

and similar to the normal velocity, $\overline{u}_\theta = u_{\theta,\,\mathrm{max}} 2/3$. While this might not appear to be the obvious choice to define the circulation input into the flow, we will show in the following that it works well to describe the momentum introduced by streamwise vortices. Coefficient of circulation, in essence is similar to helicity density, which is the dot product of velocity and vorticity. Based on the velocity profiles, the circulation input by the actuator is $\Gamma_n = 64\pi u_{\theta,\,\mathrm{max}} r_0/27$. Using the circulation input by the actuator we compute the non-dimensional vortex strength $(8 \lesssim \Gamma_\mathrm{n}/u_\tau h \lesssim 53)$ which is similar to vortex strength reported by Ashill $et\ al.$ (2002) $(15 \lesssim \Gamma/u_\tau h \lesssim 45)$. This means that the estimated vortex strength values in the present theoretical study are realizable with present vortex generator technology.

In the previous section, we identified circulation input $(f(u_\theta))$ and penetration depth $(f(u_n/U_\infty))$ to be key parameters in affecting the flow. Here, we chose to non-dimensionalize the circulation input such that $\hat{\Gamma}_n = \Gamma_n/U_\infty l_z = 32\pi \overline{u}_\theta r_0/9 U_\infty l_z$. The selection to non-dimensionalize by the spanwise spacing of the actuators is because, we are concerned with streamwise vortices mixing the free-stream and boundary layer. A streamwise vortex will impart velocity normal to the boundary layer (mixing), which acts between the two actuators. Therefore we can rewrite the coefficient of circulation as

$$C_\Gamma = \frac{\hat{\Gamma}_n \overline{u}_n r_0 \mathcal{C}}{\frac{1}{2} U_\infty c}, \tag{4.2}$$

and here we multiply by a constant $\mathcal{C}$ to account for the fractional term in circulation. The remaining terms produce the blowing ratio $(R = \overline{u}_n/U_\infty)$ which has been identified
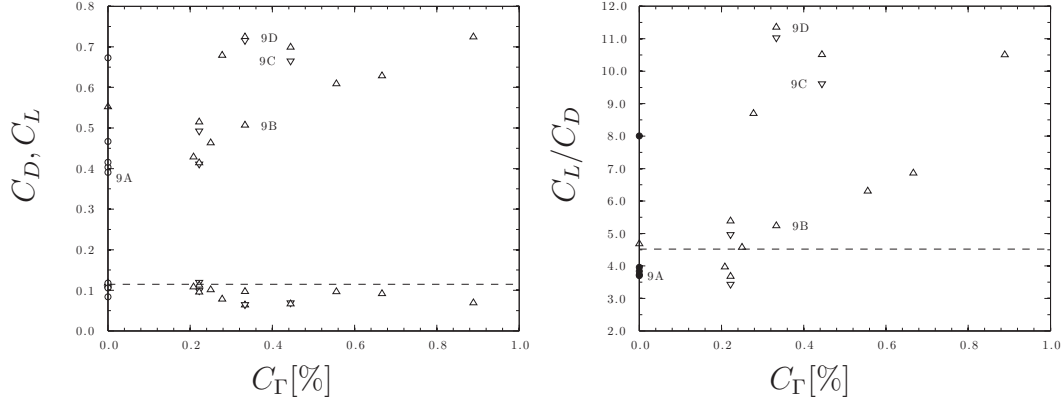
Figure 4.2: The coefficients of drag (left) and lift (right) versus the coefficient of circulation. The baseline value is indicated by ---- and the controlled cases are pure blowing, $\bigcirc$, co-rotating, ∇, and counter-rotating, Δ.

previously, and when multiplied by the diameter $(r_0/0.5)$ we obtain a coarse estimate of the penetration depth. While Muppidi & Mahesh (2005) establish a more precise estimation of the jet height (h) based on the downstream distance from the actuator and constants $(A$ and $B)$, $h/Rd = A(x/Rd)^B$, we note the reliance on the blowing ratio and diameter, Rd. The resulting coefficient of circulation is the non-dimensional circulation times the non-dimensional height of the actuator $(\hat{h} = h/c)$. Therefore we can more simply express the coefficient of circulation as $C_\Gamma = \mathcal{C}\hat{\Gamma}\hat{h}$. Next we will assess if the coefficient of circulation is adequate to account of the vorticity input by the actuator.

4.2.1 Force Coefficient

Plotting the aerodynamic forces versus 4.2 (left) and we note some general trends; lift increases and drag decreases with increasing coefficient of circulation. This general trend does not pertain to all of the cases but does largely quantify the trend observed. For example, cases 9C and 9D show increased lift compared to lower coefficients of circulation. Although, further increasing the coefficient of circulation coincides with a decrease in lift force. The aerodynamic performance parameter (C_L/C_D) is plotted in Fig. 4.2 (right). In this figure we observe that there is a drastic difference in the aerodynamic performance, it ranges from $3.5 < C_L/C_D < 11.5$. From this plot and the flow field results, we know that the cases with $C_L/C_D > 7$ correlate to fully attached flow. For most cases it is apparent based on the forces the result of the flow control input. With the above quantification of swirl input to the flow, the pure blowing cases are zero. Therefore, these cases are on the y-axis in Fig. 4.2. These plots indicate that the above coefficient does begin to quantify the effects of vorticity input, but does not sufficiently collapse the data without the inclusion of wall-normal momentum input. Next, we include the influence of both terms to account for all of the momentum introduced to the boundary layer by the control input.
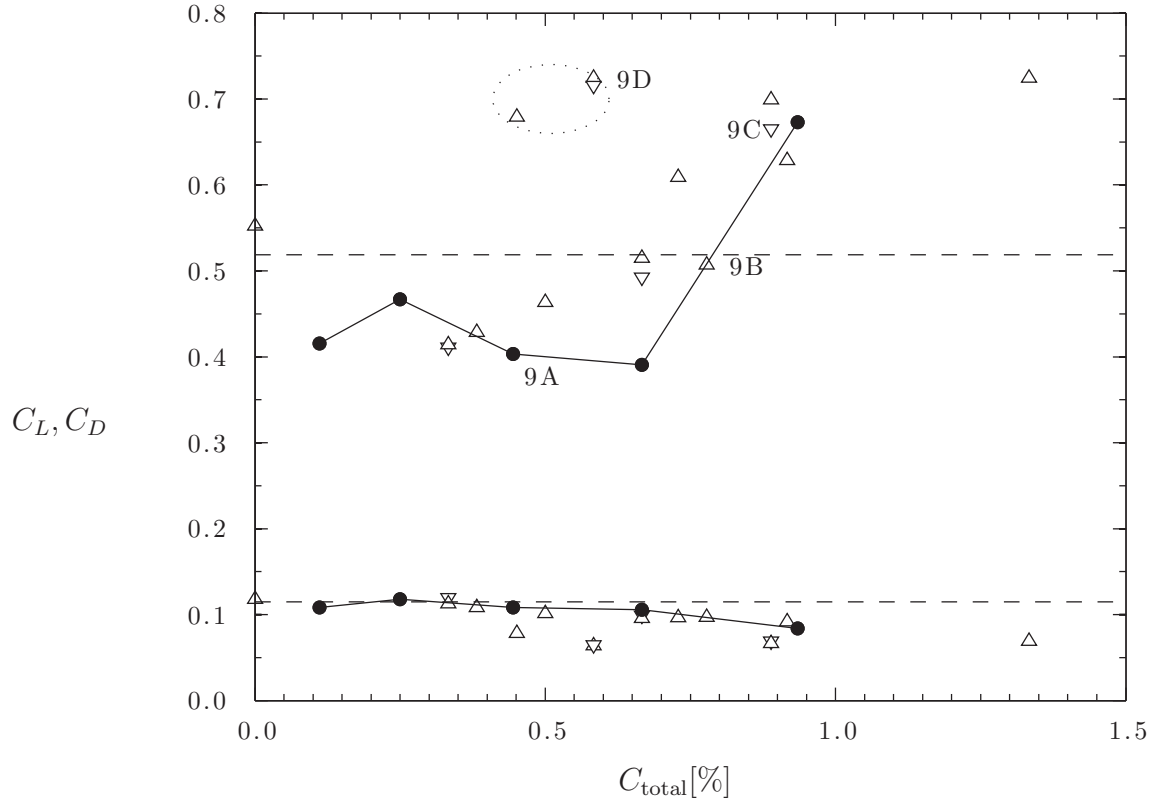
Figure 4.3: The drag and lift forces versus the total coefficient. The baseline value is indicated by ---- and the controlled cases are pure blowing, $\bigcirc$, co-rotating, ∇, and counter-rotating, Δ.

4.3 Coefficients of Momentum and Circulation

The coefficient of momentum has been used extensively in the past to describe the influence of actuators, and with the inclusion of the coefficient of circulation we attempt to include another component that affects the effectiveness of control input. Combining these two coefficients ($C_{\text{total}} = C_\mu + C_\Gamma$) allows us to more accurately quantify the total momentum introduced to the boundary layer, which can aid in the application of a wide range of actuators to single flow control scenario. The force coefficients versus the total coefficient are plotted in Fig. 4.3. Additional cases, that are discussed below, have been added to this plot to allow for further investigation into the momentum and circulation coefficient. We purposely highlight the pure blowing cases with filled circles, because these values are identical to the values for pure blowing in Fig. 4.1. In the pure blowing cases $C_\Gamma = 0$, and $C_{\text{total}} = C_\mu$, therefore we are trying to use the coefficient of circulation to account for the influence of vorticity added to flow; shifting the values to align more closely to the trend produced by the pure blowing cases.

With the current selection of $C_\mu + C_\Gamma$ we obtain, in general, two prevailing trends exist which correlate to the separated flow, and fully reattached flow. Plotting lift versus the total coefficient, three regions appear in Fig. 4.3. For smaller control input ($C_\text{total} \lesssim 0.6\%$), lift force decreases for the majority of cases which is due adding the perturbation to the flow. Though the perturbation does not add adequate momentum to overcome the adverse pressure gradient. After the initial drop due to the perturbation, the lift forces are fairly consistent. In Fig. 4.4 this region is very flat and the aerodynamic performance is consistent for the pure blowing cases. This first region primarily correlates to separated flow, and is described by case 9A, in which the time-averaged recirculation region is approximately the same size as the baseline case. We also note that in this region there are cases that reattach the flow.

For these cases which are encircled in Fig. 4.3, flow reattaches when the majority of other cases are separated with this control input. The outlier Case 9D, is plotted in Fig. 4.6 with the same visualizations as Fig. 3.3. We notice that this case eliminates separation similar to case 9C. The zero-streamwise velocity iso-surface shows very little Reynolds stress, which indicates that the flow is primarily modified by the large structures as opposed to turbulent fluctuations. The significant difference for the circled ∇ and Δ cases is the blowing ratio is such that $h(u_n/U_\infty)/\delta \approx 1$ based on the relation described by Muppidi & Mahesh (2005). For these cases that reattach the flow with $C_\text{total} \lesssim 0.6\%$, the interaction of wall-normal and azimuthal vorticity are ideal to induce the interaction of the free stream and boundary layer, leading to reattached flow. Using an azimuthal velocity $\phi = 1$ input at approximately the boundary layer height is the most effective location for the streamwise vortices to mix the flow, which is why these cases reattach the flow with a smaller total coefficient.

Near $C_\text{total} \approx 0.65\%$ lift begins to increase, shown in Fig. 4.3, and correlates to the increase in aerodynamic performance in Fig. 4.4. In the vicinity of this region we observe a small transition region, $0.65 \lesssim C_\text{total} \lesssim 0.8\%$, which corresponds to case 9B. The increase in these values is a result of reducing the size of the reverse flow region. For case 9B, control input is impacting the separation region, but flow still remains separated from the leading edge. The final region is attached flow, $C_\text{total} \gtrsim 0.8\%$, and is depicted by case 9C. For cases that are shown in this region we can begin to be confident that any device selected with $C_\text{total} \gtrsim 0.8\%$ will reattach the flow. All of the cases we examined with a total coefficient greater than 0.8 reattach the flow and result in similar force coefficients. The maximum attainable increase in lift and drag reduction is for an attached flow, so further increasing input does not continue increasing the aerodynamic performance. These three regions are not exact, but for any properly quantified actuators would indicate how much input is needed to reattach the flow.

From the previous cases discussed (9A, 9B, 9C, 9D) and our initial estimations based on C_μ, we did not attach the flow with pure blowing. Taking the knowledge of the previous discussion and the $C_\text{total} > 0.8$ cut-off into consideration, we estimated a wall-normal velocity that would reattach the flow based on the total coefficient. Using this value ($C_\text{total} = C_\mu = 0.95\%$, case 9E), we observe in Fig. 4.3 that this pure blowing case follows the aforementioned trend. As expected using a value with $C_\text{total} > 0.8\%$ has aerodynamic forces similar to cases
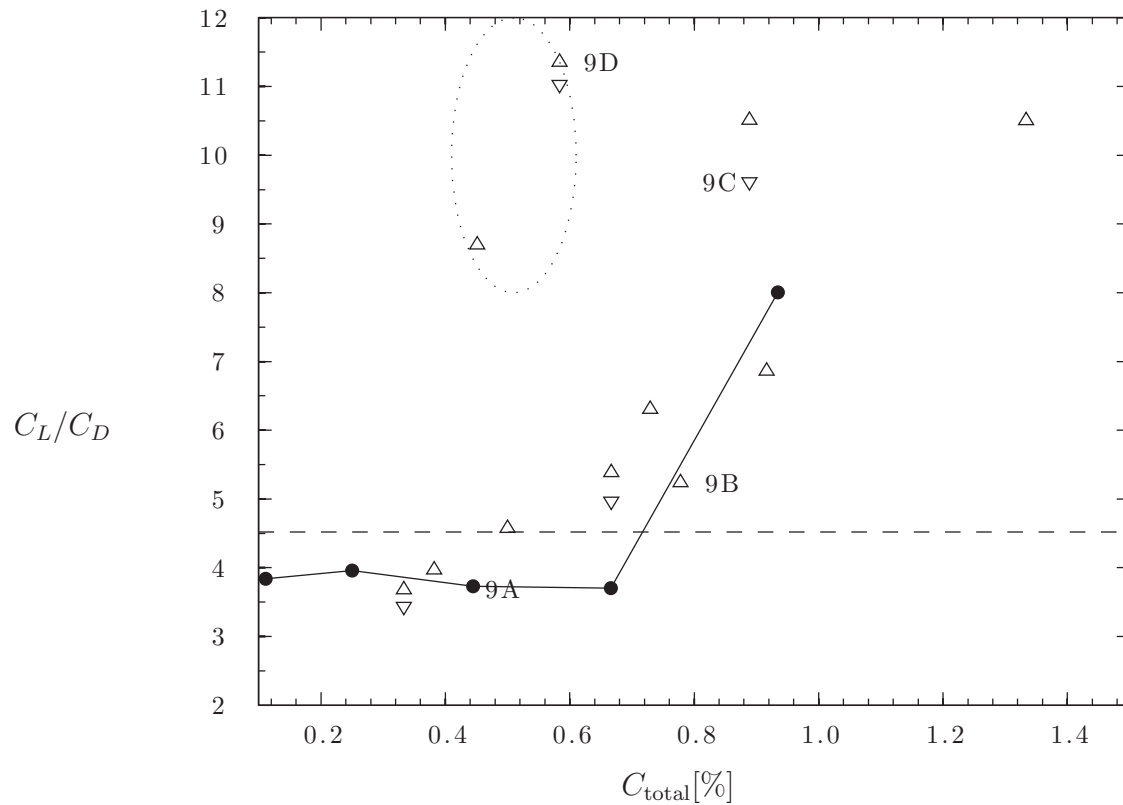
Figure 4.4: The aerodynamic performance versus the total coefficient. The baseline value is indicated by ---- and the controlled cases are pure blowing, ◯, co-rotating, ∇, and counter-rotating, Δ.

α	Case	$u_{n,max}/U_\infty$	$u_{\theta,max}/U_\infty$	Rot. dir.	C_D	C_L
9°	Baseline	–	–	–	0.118	0.584
	9D	0.945	1.26	CTR	0.084	0.673
	9E	1.83	0	–	0.084	0.673
	9F $(l_z/c = 0.2)$	1.78	0	–	0.075	0.725

Table 4.1: Select control parameters for flow over a NACA0012 airfoil at $\alpha = 9°$. The case names are for control settings that are used in the text herein.

with attached flow. The resulting flow field is plotted in Fig. 4.6 (top) and we observe that the flow is indeed attached downstream of the actuators. The increased maximum velocity increases both the momentum injected into the flow leading to attached flow for this case.

4.4 Spanwise Spacing

The total coefficient is normalized by the area that each actuator affects, thus taking into account spanwise spacing. While keeping $C_\mu = 0.44\%$, spacing smaller than $l_z/c < 0.1$ was investigated. The resulting input values are $0.15\% < C_{\text{total}} < 1.0\%$ were used in an attempt to control the flow with this configuration. It was found that the actuators are too close together and interact with one another. This interaction causes control to be less effective and no cases were run in which the flow was successfully attached for $l_z/c = 0.0667$ and 0.05.

Increasing the spacing to $l_z/c = 0.2$ allows the actuators to function without interfering with the adjacent neighbor. The normal velocity is selected such that the coefficient of momentum is the same as cases run for $l_z/c = 0.1$. To keep the coefficient of momentum constant, the maximum wall-normal velocity is increased, which offsets the increase in area. The cases run at $l_z/c = 0.2$ are plotted in Fig. 4.5. Drag decreases with increasing total coefficient, while lift increases once flow is attached. With the cases run, we observe that the data adheres to the previously reported trend. For this spacing flow reattaches at a lower total coefficient. We observe in Fig. 4.6 flow is attached downstream of the actuator for case 9F, which has flow features similar to 9E. This indicates that the spacing of the actuators an important parameter when attempting to optimize flow control input.
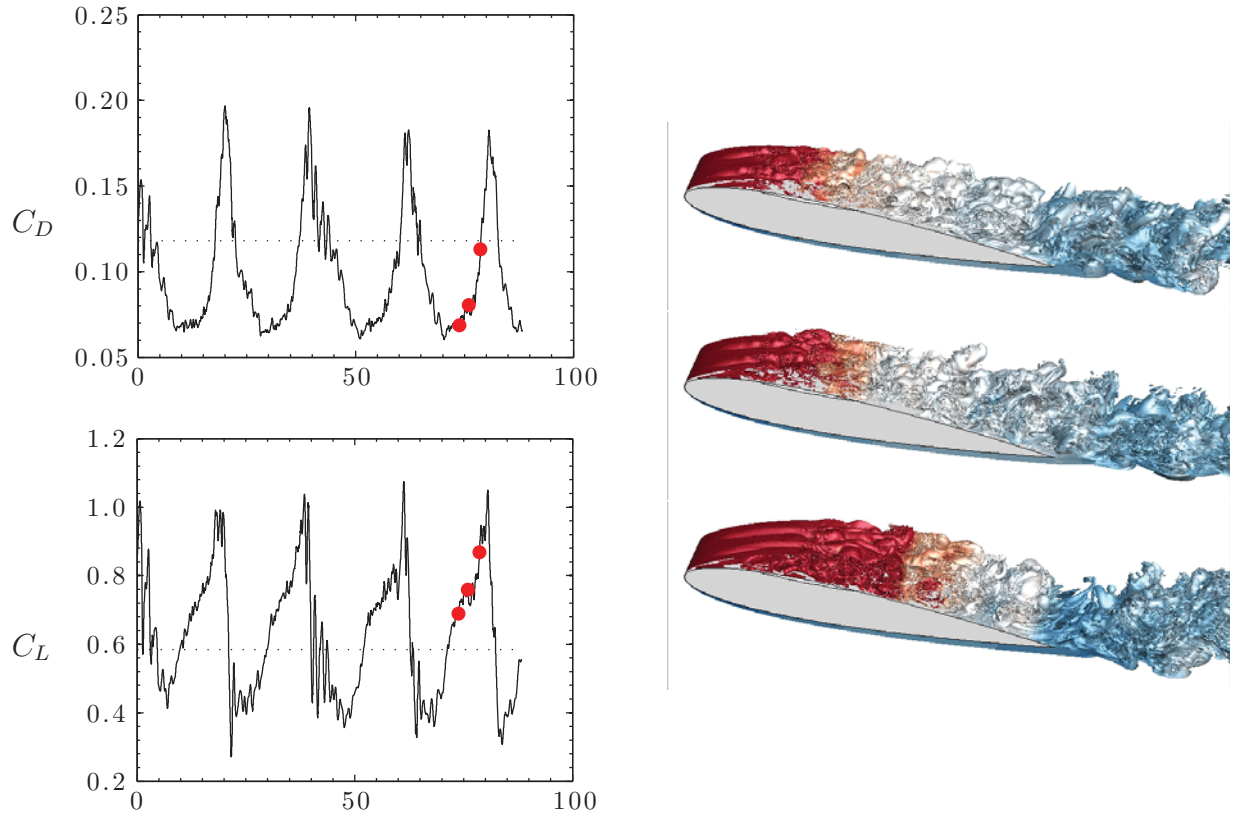
Table 4.2: Time history of the drag (top left) and lift (bottom left) coefficient for a pure blowing actuator at $\xi/c = 0.05$ The baseline force is shown with ⋯⋯ . The flow field images correspond to the ● in the time history plots, and from top to bottom the images are sequential in time.
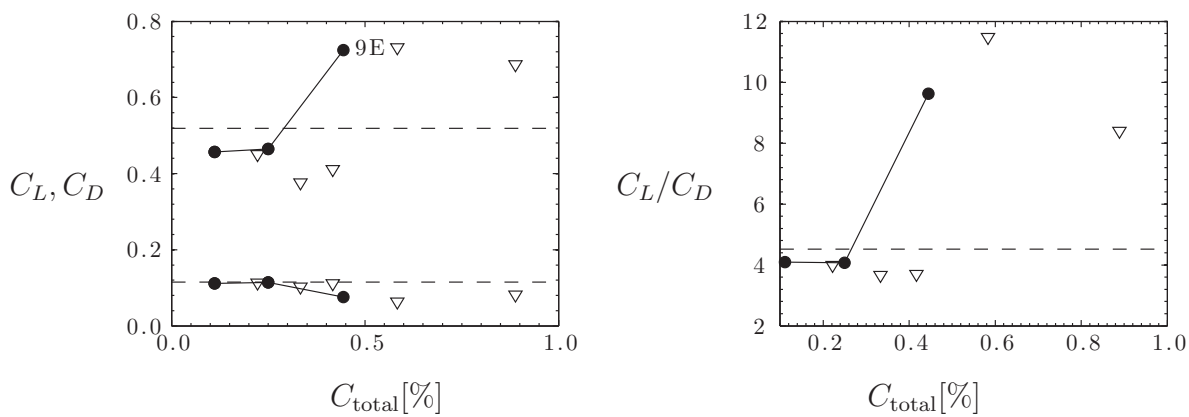
Figure 4.5: The drag and lift forces (left) and aerodynamic performance (right) versus the total coefficient. The baseline value is indicated by ---- and the controlled cases are pure blowing, ◯, co-rotating, ∇, and counter-rotating, Δ.

C_μ ϕ	Instantaneous flow field Zero-streamwise velocity	Surface vorticity flux
0.25% 1.0 (9D)		
0.93% 0 (9E)		
0.5% 0 (9F)		

C_P -0.4 -0.3 -0.2 -0.1 0 0.1 τ_{xy} -0.01 -0.005 0 0.005 0.01 σ_i -0.5 -0.25 0 0.25 0.5
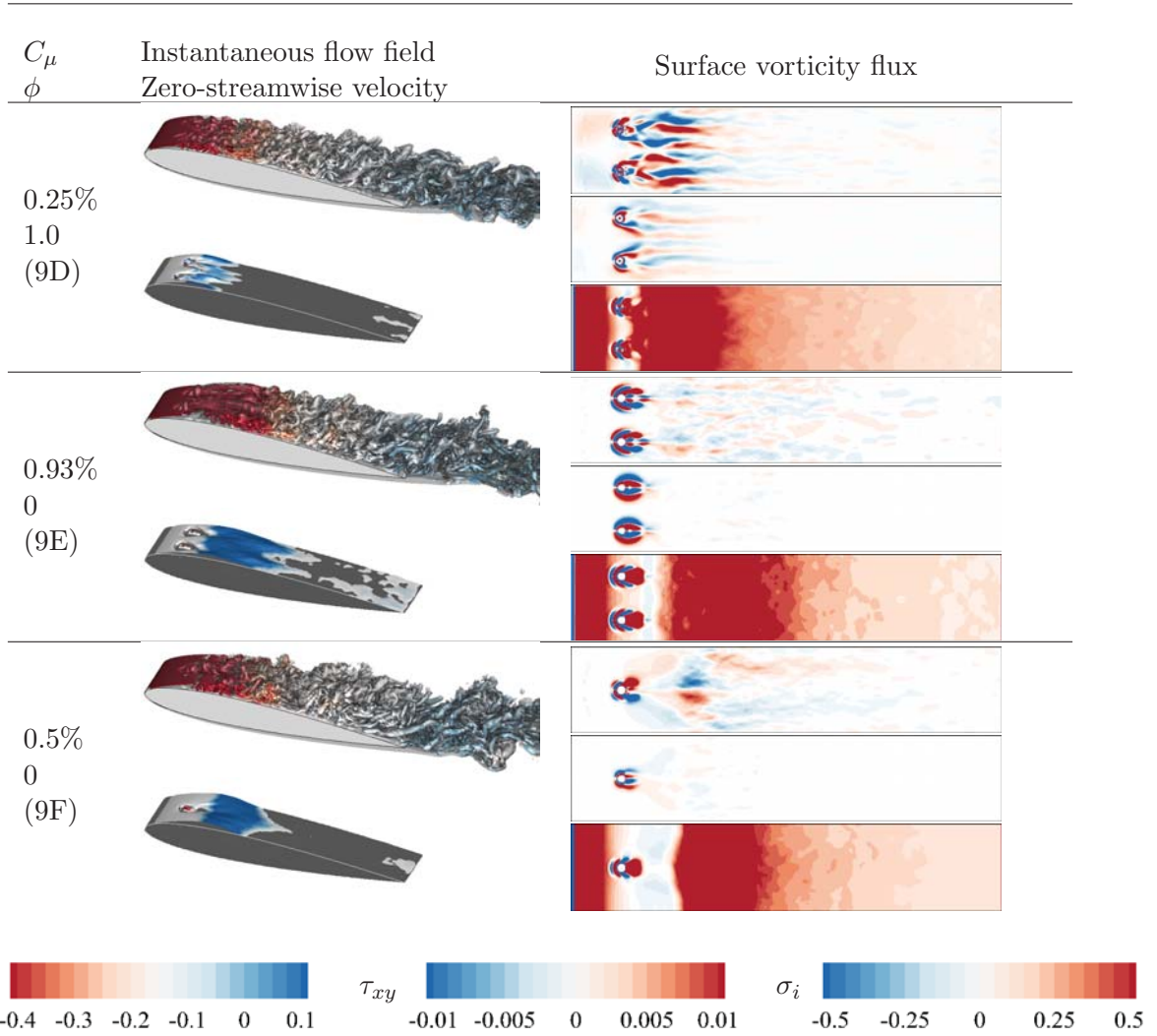
Figure 4.6: For each control case in Table 4.1 the instantaneous flow field (top left) is shown with Q-criterion colored with pressure. The time-averaged zero-streamwise velocity iso-surface is colored with spanwise Reynolds stress (bottom left). The wall normal vorticity flux is to the right from top to bottom is the streamwise, wall-normal, and spanwise vorticity.

Chapter 5

Global Stability Analysis

Understanding the temporal and spatial evolution of perturbations can aid in the placement of flow control devices as well as further the understanding the effects perturbations have on the overall flow field. Linear theory predicates that flow fields can be comprised of stable (exponential decay), unstable (exponential growth), and/or neutrally stable (remains constant) modes; identification of these modes can be done with several different approaches. These approaches include dynamic mode decomposition (Rowley *et al.*, 2009; Schmid, 2010), initial value problems (Brehm & Fasel, 2011), and global stability analysis (Theofilis, 2011, 2003), each with advantages and limitations. For example, while the initial value problems can be performed at a lower computational cost, yet the ability to resolve the eigenspectrum is greatly reduced. Global stability analysis provides a broader range of eigenvalues at an increased computational cost.

5.1 Bi-Global Stability Formulation

Performing linear stability analysis first begins with the incompressible Navier-Stokes equations,

$$\frac{\partial \boldsymbol{u}}{\partial t} + \boldsymbol{u} \cdot \nabla \boldsymbol{u} = -\nabla p + \frac{1}{Re}\nabla^2 \boldsymbol{u}, \tag{5.1}$$

$$\nabla \cdot \boldsymbol{u} = 0, \tag{5.2}$$

in which we use the non-dimensional form, noted by the Reynolds number, $Re \equiv U_\infty l / \nu_\infty$. Equations 5.1 and 5.2 are linearized such that the solution ($\boldsymbol{u}$ and p) is the sum of a base state ($\overline{\boldsymbol{u}}$ and $\overline{p}$) and perturbation ($\boldsymbol{u}'$ and p') (Schmid, 2007; Theofilis, 2011, 2003). In the linearization process, two assumptions are made: the base state ($\overline{\boldsymbol{u}}$, $\overline{p}$) satisfies the Navier-Stokes equations, and the perturbations ($\boldsymbol{u}'$, p') are relatively small, i.e., $|\boldsymbol{u}'|/|\overline{\boldsymbol{u}}| = \mathcal{O}(\epsilon) \ll 1$. When $\overline{\boldsymbol{u}} + \boldsymbol{u}'$ and $\overline{p} + p'$ are substituted into Eqs. 5.1 and 5.2, and higher order terms ($\mathcal{O}(\epsilon^2)$)

are removed, we arrive at the linearized Navier-Stokes equations

$$\frac{\partial \boldsymbol{u}'}{\partial t} = -\boldsymbol{u}' \cdot \nabla \overline{\boldsymbol{u}} - \overline{\boldsymbol{u}} \cdot \nabla \boldsymbol{u}' - \nabla p' + \frac{1}{Re} \nabla^2 \boldsymbol{u}', \tag{5.3}$$

$$\nabla \cdot \boldsymbol{u}' = 0. \tag{5.4}$$

From the above equations, we not that the advection term provides the only mechanism for the base flow to interact with the perturbation. Once perturbations grow large ($|\boldsymbol{u}'|/|\overline{\boldsymbol{u}}| > \epsilon$), the linearized equations are no longer valid due to the sizeable nonlinear interactions amongst the perturbations.

In order to simplify the problem, assumptions are made about spatial characteristics of the flow. The simplification assumes a wave-like propagation in one or two spatial directions. For flows varying in two spatial directions, assuming a wave-like pattern in the third is considered bi-global stability. To perform bi-global stability analysis, the perturbation $\boldsymbol{q}'$ $=[\boldsymbol{u}',p']^T$ is assumed to have a solution of the form

$$\boldsymbol{q}'(x, y, z, t) = \hat{\boldsymbol{q}}(x, y) \exp[i(\beta z - \omega t)] + \text{c.c.}, \tag{5.5}$$

and the perturbation is assumed to be wavelike in the spanwise direction with a spanwise wavenumber $\beta = 2\pi/L_z$, and L_z is the spanwise wavelength. Temporally, $\omega = \omega_r + i\omega_i$ is the complex eigenvalue for the two-dimensional eigenmode $\hat{\boldsymbol{q}}$. Based on Eq. 5.5, the eigenvalues contain information about the exponential growth and decay rates (ω_i), as well as the frequency of the global modes (ω_r). The growth ($\omega_i > 0$) or decay ($\omega_i < 0$) rate is of particular interest because, as mentioned previously, flow control can effectively take advantage of inherent instabilities in the flow. Herein, we refer to modes with a positive growth rate as unstable, and negative as stable ($\omega_i = 0$, is neutrally stable). Additionally, modifying the frequency of perturbations can directly influence the growth and decay rate of specific modes. Based on the frequency content of modes, we classify a mode as steady if $\omega_r = 0$ or unsteady if $\omega_r \neq 0$. Unsteady modes come in complex conjugates pairs.

5.1.1 Eigenvalue Problem

To perform an eigenanalysis of a fluid flow, we seek to derive the algebraic form of the linearized Navier-Stokes equations. Substituting the solution form (Eq. 5.5) into the linearized Navier-Stokes equations (Eqs. 5.3 and 5.4) results in

$$-\overline{u}\frac{\partial \hat{u}}{\partial x} - \overline{v}\frac{\partial \hat{u}}{\partial y} - \hat{u}\frac{\partial \overline{u}}{\partial x} - \hat{v}\frac{\partial \overline{u}}{\partial y} - \frac{\partial \hat{p}}{\partial x} + \frac{1}{Re}\left(\frac{\partial^2 \hat{u}}{\partial x^2} + \frac{\partial^2 \hat{u}}{\partial y^2} - \beta^2 \hat{u}\right) = -i\omega\hat{u}, \tag{5.6}$$

$$-\overline{u}\frac{\partial \hat{v}}{\partial x} - \overline{v}\frac{\partial \hat{v}}{\partial y} - \hat{u}\frac{\partial \overline{v}}{\partial x} - \hat{v}\frac{\partial \overline{v}}{\partial y} - \frac{\partial \hat{p}}{\partial y} + \frac{1}{Re}\left(\frac{\partial^2 \hat{v}}{\partial x^2} + \frac{\partial^2 \hat{v}}{\partial y^2} - \beta^2 \hat{v}\right) = -i\omega\hat{v}, \tag{5.7}$$

$$-\overline{u}\frac{\partial \hat{w}}{\partial x} - \overline{v}\frac{\partial \hat{w}}{\partial y} - \hat{u}\frac{\partial \overline{w}}{\partial x} - \hat{v}\frac{\partial \overline{w}}{\partial y} - i\beta\hat{p} + \frac{1}{Re}\left(\frac{\partial^2 \hat{w}}{\partial x^2} + \frac{\partial^2 \hat{w}}{\partial y^2} - \beta^2 \hat{w}\right) = -i\omega\hat{w}, \tag{5.8}$$

$$\frac{\partial \hat{u}}{\partial x} + \frac{\partial \hat{v}}{\partial y} + i\beta\hat{w} = 0. \tag{5.9}$$

We can formulate these equations as $A\hat{\boldsymbol{q}} = -i\lambda B\hat{\boldsymbol{q}}$, where A is the linear operator (left-hand side of Eqs. 5.6 - 5.9), and λ is the eigenvalue to be solved (ω). Matrix B is of the form

$$B = \begin{bmatrix} 1 & 0 & \cdots & 0 \\ 0 & 1 & \ddots & \vdots \\ \vdots & \ddots & 1 & 0 \\ 0 & \cdots & 0 & 0 \end{bmatrix}, \tag{5.10}$$

which by simple inspection, is not invertible ($det(B) = 0$). Thus, the shift and invert strategy is utilized, and the eigenvalue problem becomes $(A - \sigma B)^{-1}B\tilde{\boldsymbol{q}} = \tilde{\lambda}\tilde{\boldsymbol{q}}$ (Natarajan & Acrivos, 1993). The new problem solves different eigenvalues ($\tilde{\lambda}$), which are related to the original problem by $\lambda = 1/(\tilde{\lambda} - \sigma)$. This particular algorithm searches for eigenvalues closest to the shift parameter (σ). The shift value can be modified to obtain results for different regions of the eigenspectrum.

We take advantage of the domain decomposition and discrete operators from the `Charles` software package. As mentioned previously, the finite volume operators are second order accurate (Ham & Iaccarino, 2004; Ham *et al.*, 2006). For this discretization scheme, the non-zero values of the matrix are illustrated in Fig. 5.1. In the present study, a two-dimensional base state will result in a non-zero value in only two directions ($\overline{u}, \overline{v} \neq 0, \overline{w} = 0$), and the matrix structure is plotted Fig. 5.1. Due to the size and sparseness of the matrices $A \in \mathbb{R}^{N \times N}$ and $B \in \mathbb{R}^{N \times N}$, a matrix-free method to solve the eigenvalue problem is desired to reduce memory requirements for the large-scale problem. The two-dimensional mesh for the NACA 0012 airfoil has $\mathcal{O}(10^5)$ points, and the size of the problem $N \equiv 4 \times$number of grid points. The reverse communication interface of `ARPACK` (Lehoucq *et al.*, 1998) is used to accommodate the matrix-free Arnoldi algorithm. An iterative solver is used to invert the large sparse matrix $(A - \sigma B)^{-1}$; Bi-Conjugate Gradient Stabilized method (Bi-CGSTAB) (Barrett *et al.*, 1993) is implemented for the matrix inversion.

The implementation of the aforementioned procedure can be simplified and explained in Algorithm 1. The procedure hinges primarily on the `ARPACK` subroutine `dnaupd`, which is the serial implicitly restarted Arnoldi algorithm (Lehoucq *et al.*, 1998). The parallel version is `pdnaupd`. The implicitly restarted Arnoldi algorithm, creates an output ($\boldsymbol{b}$) and requests an input ($\boldsymbol{x}$) based on the operator ($\boldsymbol{A}$). As mentioned previously, the returned values ($\boldsymbol{x}$), are solved with the Bi-CGSTAB. The convergence to the proper eigenvalues is dependent on the convergence criteria of the two iterative processes. According to the documentation of the `ARPACK` subroutine used (Lehoucq *et al.*, 1998), the Bi-CGSTAB convergence tolerance should be less than the tolerance of the Arnoldi method ($tol_{\text{Bi-CG}} < tol_{\text{Arnoldi}}$).
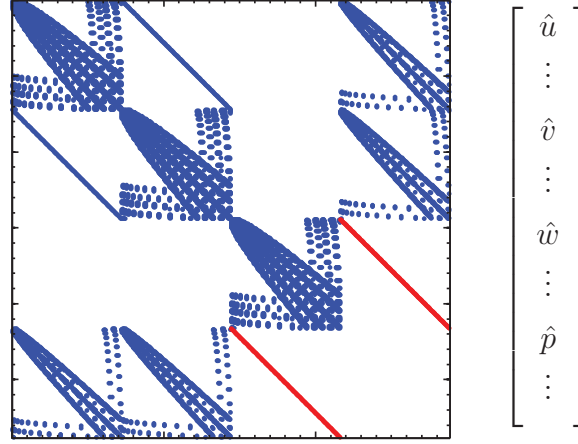
Figure 5.1: Structure of the full matrix form of Eqs. 5.6 - 5.9 on a 16×16 domain with periodic boundary conditions. The colors indicate the non-zero real and imaginary components of $A(i,j)$; real and imaginary components are represented by ■ , and ■ , respectively.

Algorithm 1 Matrix Free Bi-Global Stability Analysis

1: **while** $err_{\text{Arnoldi}} \geq tol_{\text{Arnoldi}}$ **do**
2:     Call Arnoldi algorithm (`znaupd`/`pznaupd`)
3:     Interpret output from Arnoldi algorithm
4:     Set-up the problem in the form $Ax = b$
5:     Provide an initial guess for x_0
6:     Compute initial residual
7:     **while** $err_{\text{Bi-CGSTAB}} \geq tol_{\text{Bi-CG}}$ **do**
8:         Update initial guess based on residual $(x_{i-1} \rightarrow x_i)$
9:         Compute new residual based on new solution
10:         Update error $(err_{\text{Bi-CG}} = ||Ax_i - b||_2)$
11:     **end while**
12: **end while**
13: Call Arnoldi post-processing routing (`zneupd`/`pzneupd`)

5.1.2 Boundary Conditions

Traditional boundary conditions are enforced, but special consideration for stability analysis has to be taken into account for both the base flow and perturbation. Dirichlet or Neumann boundary conditions can be implemented for velocity and pressure perturbations.

Wall

For no-slip boundaries, velocity at the wall is zero, $\boldsymbol{U}_{BC} = \overline{\boldsymbol{u}} = \hat{\boldsymbol{u}} = 0$. The base flow should satisfy the boundary condition, so the perturbation velocity at the wall is Dirichlet and specified to be $\hat{u} = \hat{v} = \hat{w} = 0$. The compatibility pressure boundary conditions are specified to be Neumann,

$$\frac{\partial \hat{p}}{\partial \hat{n}} = \frac{1}{Re} \nabla^2 (\boldsymbol{u} \cdot \hat{n}), \tag{5.11}$$

which is reported to be successful in the previous study by Theofilis *et al.* (2004).

Inflow

Depending on the structure of the domain, an inflow condition may be more appropriate or applicable as opposed to the far field condition. In the present cases, the inflow is laminar $(U_\infty = 1)$, and with that knowledge of the flow field, perturbations should approach zero at the inlet of the domain. Therefore, this additional boundary condition was created for perturbation velocity and pressure to be zero $(q' = 0)$.

Outflow and Far Field

Downstream of the airfoil, an appropriate boundary condition is necessary to allow pertur-bations to leave the domain. Similarly, approaching the far field, exact boundary conditions are unknown, therefore the outflow boundary condition is compatible for boundaries consid-ered as far field. In open flow, perturbations are advected downstream and will impact the boundary of the finite computational domain. Boundary information is obtained from the interior, by means of linear extrapolation. Values of the interior perturbation and derivative are used to calculate the boundary values. To accommodate unstructured domains, multiple interior nodes (n is the number of nodes) are used to extrapolate the solution for a single boundary node, which is done as follows

$$\hat{q}_b = \frac{1}{\sum_{i=1}^{n} \frac{1}{\Delta \boldsymbol{x}_i}} \left(\sum_{i=1}^{n} \frac{\hat{q}_i + \Delta \boldsymbol{x}_i \frac{\partial \hat{q}}{\partial \boldsymbol{x}}}{\Delta \boldsymbol{x}_i} \right). \tag{5.12}$$

Weighting the interior nodes to the inverse of distance allows for nodes closer to the boundary node to be more influential. The distance between the inner node and boundary point are defined as $\Delta \boldsymbol{x}_i = \boldsymbol{x}_b - \boldsymbol{x}_i$. Linear extrapolation at the boundary has worked in the past for multiple studies and was found to be a robust approximation for boundaries in open flow (Kitsios *et al.*, 2009; Rodríguez, 2010).

5.1.3 Base flow

In the formulation of stability analysis, a base state is required for the linear Navier–Stokes equations. To solve for the base state, direct numerical simulations are performed using the finite volume solver Charles (Cliff for Incompressible flow). Boundary conditions used

are slip, no-slip, inlet, and outlet. For steady flow, solving for the base flow is trivial. A simulation can be performed allowing transients to decay, resulting in the final state being equivalent to the stable base state. It is more difficult to obtain the base state for an unstable flow, and we outline the formulation used below.

Unstable steady state

In the present study, the primary intent is to perform stability analysis with respect to the unstable steady state. Note that the base flow is in general not equal to the time-averaged flow field. Selective frequency damping is used to find the unstable steady state and can be represented as

$$\frac{d\boldsymbol{u}}{dt} = NS(\boldsymbol{u}) - \chi(\boldsymbol{u} - \tilde{\boldsymbol{u}}), \tag{5.13}$$

where NS is the right-hand side of the Navier-Stokes operator, χ is the gain, and $\tilde{\boldsymbol{u}}$ is a time-filtered, nonlinear flow field (Åkervik *et al.*, 2006). The forcing term added to the right hand side of the Navier-Stokes equations forces the flow to the unstable steady state. A second-order low-pass Butterworth filter is implemented to allow the filtered solution to approach the base state. The cut-off frequency is selected to be below the dominant (characteristic) frequency present in the flow. This case is run until $\max(d\boldsymbol{u}/dt) < $ tol, where tol is a tolerance selected by the user.

5.2 BiGlobal Stability Analysis

We validate the above formulation using the following two problems: lid-driven cavity and separated flow over a NACA 0015 at $\alpha = 18°$. First, we quantitatively verify the results by comparing the least stable eigenvalues to previous lid-driven cavity studies. Qualitatively, we compare the eigenmodes of separated flow over an airfoil to verify the results for open flow cases.

5.2.1 Lid-Driven Cavity

BiGlobal stability analysis of lid-driven cavity flow has been investigated thoroughly in past studies. The steady solution ($\hat{\boldsymbol{u}}(t \to \infty)$) of the non-linear direct numerical simulation of lid-driven cavity is used for the base flow. The base flow for $Re = 100$ is plotted in Fig. 5.2 (left). For validation, the leading eigenvalue(s) for two different spanwise wavelengths are compared with results reported by Theofilis *et al.* (2004), see Table 5.1. Changing the spanwise wave length (β), modifies the characteristics of the leading eigenvalue. The leading eigenvalue for the both spanwise wavelengths is stable ($\sigma_i < 0$), and is steady ($\omega_r = 0$) for $\beta = 1$ and unsteady ($\omega_i \neq 0$) for $\beta = 5$. The first 96 eigenvalues for $Re = 200$ and $\beta = 1$ are shown in Fig. 5.2 (right).

Table 5.1: Most unstable eigenvalue for lid-driven cavity flow at $Re = 200$.

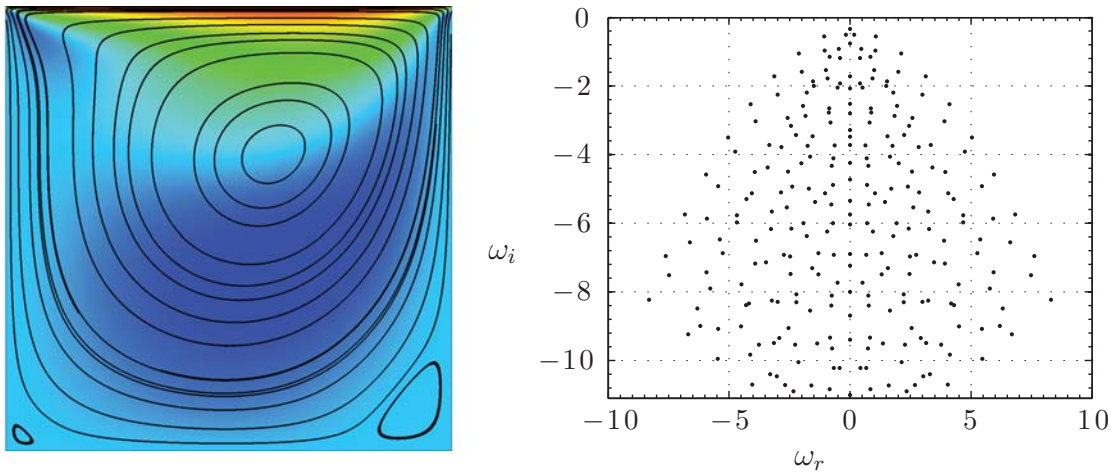|	$\beta = 1$	$\beta = 5$
Theofilis *et al.* (2004)	$0.000 - 0.3297i$	$\pm 0.4260 - 0.3404i$
Present Results	$0.000 - 0.3298i$	$\pm 0.4274 - 0.3410i$

Figure 5.2: Base flow and 96 closest to the shift value $\sigma = 1$. The Reynolds number and spanwise wave number are $Re = 200$ and $\beta = 1$, respectively.

5.2.2 NACA 0015, $\alpha = 18°$

A NACA 0015 airfoil at $\alpha = 18°$ is investigated at low Reynolds numbers ($Re\mathcal{O}(100)$) by Kitsios *et al.* (2009) and we will use this set-up to verify the correct implementation of the code for open flow scenarios. For comparison at higher Reynolds numbers ($Re\mathcal{O}(10^4)$) we compare the results of the present solver to those of Zhang & Samtaney (2016). Though the study by Zhang & Samtaney (2016) is with a different airfoil (NACA 0012) and angle of attack ($\alpha = 16°$), the base state for the separated flows is similar. Thus, we qualitatively compare the results to ensure the solver is capable of handling open flow and increased Reynolds number. We compare the results of flow at $Re = 200, 600$, and $1,000$ and $\beta = 1$.

Base Flow

For the following cases, the base flow is the unstable steady state, except for $Re = 200$ which we will notice is inherently steady. The gain used in all of the cases using selective frequency damping is $\chi = 1.0$. The size of the two-dimensional computational domain $(x/c, y/c) \in [-20, 25] \times [-20, 20]$. The boundary conditions at the inlet is uniform, laminar flow, $U_\infty = [1, \ 0]$. Top and bottom are slip boundaries. The airfoil near the center of the domain is set to be a wall, i.e. no-slip and no-penetration boundary. The outflow boundary is a convective outlet, which allows structures to leave the domain without affecting the near field solution. The outflow boundary is described by $\frac{\partial \boldsymbol{u}}{\partial t} + U_c \frac{\partial \boldsymbol{u}}{\partial \hat{n}} = 0$ and the convective velocity (U_c) is defined as the mean velocity at the outlet.

Computing the base flow at $Re = 200$, we observe a stable, separated flow. In Fig. 5.3 (top), flow separates from the leading edge and produces a primary recirculation region. From the trailing edge a smaller secondary recirculation region is generated. The center of the primary recirculation region is relatively close to the airfoil. At $Re = 600$, the increase in Reynolds increases the size of both the recirculation regions behind the airfoil. From Fig. 5.3 we observe further increasing the Reynolds number gradually increases the size of the recirculation regions. The distance of the two recirculation regions are a similar distance from the airfoil.

Eigenmodes

Using the base flows described above, we compute the eigenvalues and eigenvectors for the BiGlobal stability formulation. At $Re = 200$, the flow is steady, and as a result there are no unstable eigenvalues. In Fig. 5.3, the most unstable modes are shown and at $Re = 200$; we note that the mode has a negative growth rate. The colored contour visualizes the x-direction perturbation velocity, which is similar to the wake mode observed in separated flow, such as circular cylinder (Noack & Eckelmann, 1994). Increasing Reynolds number, both $Re = 600$ and $1,000$ have unstable modes, whose eigenvectors are similar that of $Re = 200$. The increased Reynolds number produces cases that begin to shed, which correlates to the emergence of unstable modes. At $Re = 600$, there are two unstable modes: a steady mode and unsteady mode (plotted in Fig. 5.3). Further increasing the Reynolds number ($Re = 1000$), an additional wake mode is excited, resulting in a near and far wake mode.
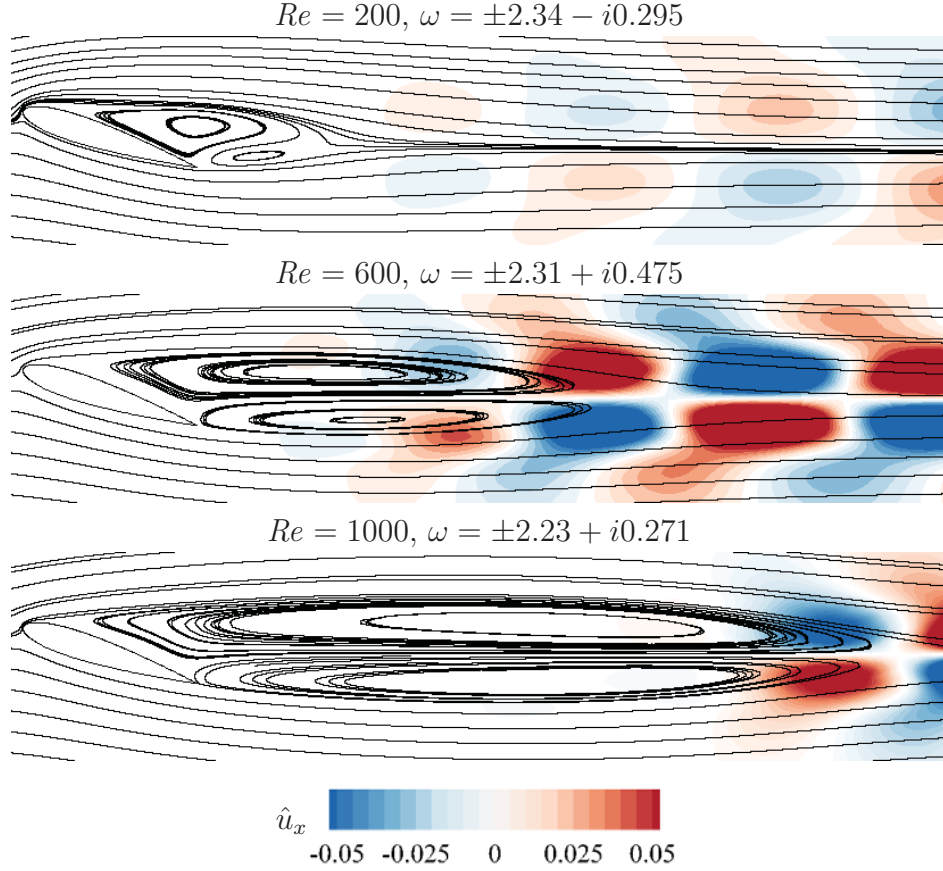
Figure 5.3: Streamlines of the base flow for each case Reynolds number, accompanied by the contour of $\hat{u}_x$.

The two wake modes and steady mode are consistent with the observations of Zhang & Samtaney (2016) at the same Reynolds number. The agreement between the two cases shows that the formulation of matrix-free, bi-global stability eigenvalue problem appears to be correct. With direct numerical simulation these were the largest Reynolds number cases that were attained in this study using biglobal stability analysis. Further increasing Reynolds number requires drastically increased computational resources.

Chapter 6

Network Analysis

6.1   Network-theoretic framework

To assess and describe the vortical interactions in the flow field, we utilize a weighted network (graph). The definition of a network (graph) $\mathcal{G}$ requires sets of vertices (nodes) $\mathcal{V}$, edges $\mathcal{E}$, and weights $\mathcal{W}$ (Newman, 2010). With these three components defined, a graph can be uniquely determined, i.e., $\mathcal{G} = \mathcal{G}(\mathcal{V}, \mathcal{E}, \mathcal{W})$. The nodes $\mathcal{V}$ in this study are taken to be the vortical elements and the edges $\mathcal{E}$ represent the vortical interactions between those vortical elements. The edge weights $\mathcal{W}$ quantify the strengths of the vortical interactions. Given n nodes, a collection of the weights w_{ij} in the form of a matrix $\boldsymbol{A} \in \mathbb{R}^{n \times n}$ with

$$A_{ij} = \begin{cases} w_{ij} & \text{if } (i,j) \in \mathcal{E} \\ 0 & \text{otherwise,} \end{cases} \tag{6.1}$$

is called the adjacency matrix and is used to describe the network connectivity. In the above definition, A_{ij} is set to the edge weight w_{ij} if there exists an edge (interaction) between nodes i and j. Details on the fundamental concepts involved in network theory can be found in Newman (2010) and Dorogovtsev (2010) with descriptions of vortical-interaction networks in Nair & Taira (2015). The diagonal entries of the adjacency matrix relate to the weight of the self-connecting (loops) edges. The adjacency matrix of an undirected graph is symmetric. The degree k_i of a vertex i represents the summation of the weights of the edges connected to it given by $k_i = \sum_{j=1}^{N} [\boldsymbol{A}_{\mathcal{G}}]_{ij}$. Another important matrix in graph theory is the graph Laplacian matrix $\boldsymbol{L}_{\mathcal{G}} \in \mathbb{R}^{N \times N}$, which is given by

$$[\boldsymbol{L}_{\mathcal{G}}]_{ij} = \begin{cases} k_i & \text{if } (i,j) \in E \text{ and } (i = j) \\ -w_{ij} & \text{if } (i,j) \in E \text{ and } (i \neq j) \\ 0 & \text{otherwise.} \end{cases} \tag{6.2}$$

The graph Laplacian matrix can also be deduced from the adjacency matrix, $\boldsymbol{L}_{\mathcal{G}} = \boldsymbol{D}_{\mathcal{G}} - \boldsymbol{A}_{\mathcal{G}}$, where $\boldsymbol{D}_{\mathcal{G}} \in \mathbb{R}^{N \times N}$ is a diagonal matrix with elements equal to degrees of vertices, $\boldsymbol{D}_{\mathcal{G}} = \text{diag}([k_i]_{i=1}^{N})$. For undirected networks, it is symmetric and positive semidefinite (singular).
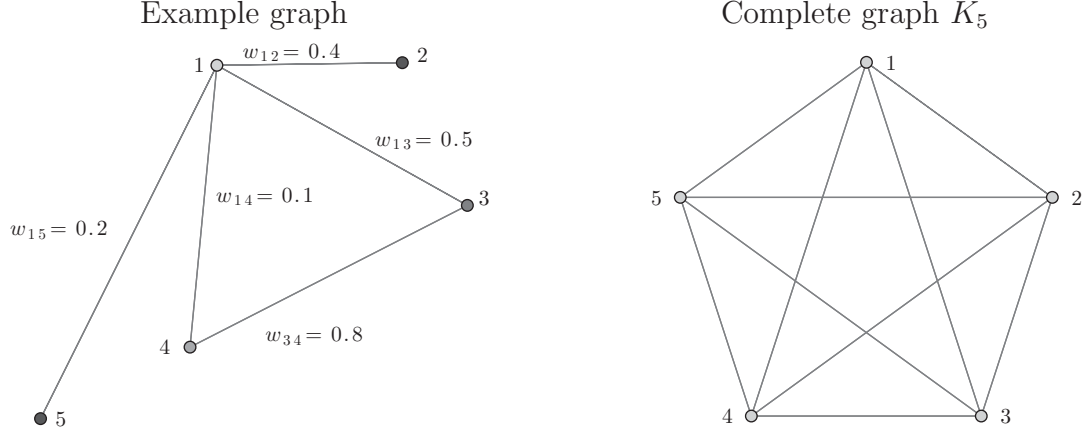
Figure 6.1: (left) An example weighted graph; and (right) a complete graph $\mathcal{K}_5$.

This Laplacian matrix is a discrete analog of the negative continuous Laplacian operator $(-\nabla^2)$ and is also called as the discrete Laplacian. It is naturally defined by its quadratic form. If we have a linear system of the form $\boldsymbol{L}_\mathcal{G}\boldsymbol{x} = \boldsymbol{b}$, for the vector $\boldsymbol{x} \in \mathbb{R}^N$, the Laplacian quadratic form of a weighted graph $\mathcal{G}$ is given by Mohar (1991)

$$\boldsymbol{x}^T \boldsymbol{L}_\mathcal{G} \boldsymbol{x} = \sum_{(i,j)\in E} w_{ij}(x_i - x_j)^2. \tag{6.3}$$

The discrete Laplacian is a smoothness indicator of $\boldsymbol{x}$ over the edges in $\mathcal{G}$. The Laplacian quadratic form becomes large as $\boldsymbol{x}$ jumps over the edges of $\mathcal{G}$. The definitions of adjacency matrix and graph Laplacian form the building blocks of the graph-theoretic framework. The Laplacian quadratic form will be used below to introduce the notion of spectral similarity of graphs and graph sparsification.

An example of a weighted graph is shown in Fig. 6.1 (left) with weights associated with the edges displayed. A complete graph $\mathcal{K}_N$ with $N = 5$, shown in Fig. 6.1 (right), has all the vertices connected to each other. In other words, this graph has N vertices with complete set of possible $N(N-1)/2$ edges without any self-loops. The adjacency matrix for an example graph $\boldsymbol{A}_\mathcal{G}$ and the complete graph $\boldsymbol{A}_{\mathcal{K}_5}$ shown in Fig. 6.1 are given by

$$\boldsymbol{A}_\mathcal{G} = \begin{pmatrix} 0 & 0.4 & 0.5 & 0.1 & 0.2 \\ 0.4 & 0 & 0 & 0 & 0 \\ 0.5 & 0 & 0 & 0.8 & 0 \\ 0.1 & 0 & 0.8 & 0 & 0 \\ 0.2 & 0 & 0 & 0 & 0 \end{pmatrix} \text{ and } \boldsymbol{A}_{\mathcal{K}_5} = \begin{pmatrix} 0 & 1 & 1 & 1 & 1 \\ 1 & 0 & 1 & 1 & 1 \\ 1 & 1 & 0 & 1 & 1 \\ 1 & 1 & 1 & 0 & 1 \\ 1 & 1 & 1 & 1 & 0 \end{pmatrix},$$

where $\mathcal{G}$ is a weighted graph and $\mathcal{K}_5$ is an unweighted complete graph.

Vortical interactions on a graph

To extract the network structure of the flow, we quantify the interactions between fluid elements based on the vortical interactions. The velocity $\boldsymbol{u}$ at position $\boldsymbol{x}$ induced by the vorticity distribution $\boldsymbol{\omega}$ of the flow is

$$\boldsymbol{u}(\boldsymbol{x}, t) = \frac{1}{4\pi} \int \frac{\boldsymbol{\omega}(\tilde{\boldsymbol{x}}, t) \times (\boldsymbol{x} - \tilde{\boldsymbol{x}})}{|\boldsymbol{x} - \tilde{\boldsymbol{x}}|^3} d\tilde{\boldsymbol{x}}. \tag{6.4}$$

A vortex is advected by the induced velocity from the other vortices and not by its own velocity. Each vortex is influenced by all other vortices, which means that each and every vortex has a connection to all other vortices without any self-loops. Thus, the discrete system of N point vortices can be represented by a weighted complete graph, $\mathcal{K}_N$. The vertices or nodes of the graph represent the discrete point vortices and the edge weights represent the strength of the connections between them. The motion of point vortices is influenced by the strengths (circulation) of the individual point vortices and the distances between them. The shorter the distance between the point vortices, the higher is the influence of the vortices on each other. Also, a vortex with higher strength has more ability to influence the surrounding vortices compared to that with lower strength. We assign the weight for the interaction between two vortices to be dependent on the characteristic vortex induced velocity based on the strengths of the two vortices and the distance between them. Thus, this implies that the edge weight for the vortex network should be proportional to κ/r, where κ is the characteristic strength of the two vortices and r is the distance between them within the network. The magnitude of the induced velocity from fluid element i on another element j reduces from Eq. (6.4) to

$$u_{i \to j} = \frac{|\kappa_i|}{2\pi |\boldsymbol{x}_i - \boldsymbol{x}_j|}, \tag{6.5}$$

Based on Eq. (6.5), we define the network adjacency matrix as the average induced velocity

$$A_{ij} = \begin{cases} \frac{1}{2}(u_{i \to j} + u_{j \to i}) & \text{if } i \neq j \\ 0 & \text{otherwise} \end{cases} \tag{6.6}$$

to quantify the magnitude of interaction between fluid elements i and j (Nair & Taira, 2015). Alternatively, the geometric mean of induced velocity can be used to define the network adjacency matrix,

$$[\boldsymbol{A}_{\mathcal{G}}]_{ij} = \begin{cases} \sqrt{u_{i \to j} u_{j \to i}} & \text{if } (i, j) \in E \text{ and } i \neq j \\ 0 & \text{otherwise}. \end{cases} \tag{6.7}$$

Note that an element cannot impose velocity upon itself, which is captured by the null entry along the diagonal of the adjacency matrix.

6.2 Graph sparsification

In order to identify key vortical interactions involved in unsteady fluid flows, we construct sparse approximation of dense vortical graphs. Graph sparsification is useful for designing computationally efficient algorithms and helps in identifying representative edges and associated weights (Spielman & Teng, 2011). Graph similarity, which forms the basis for graph sparsification, can be derived in a number of ways depending on the desired similarity properties. Distance similarity of graphs (Peleg & Ullman, 1989) can be achieved by sparse graphs called spanners that keep the same shortest-path distance between each pair of vertices as in the original graph while cut similarity (Benczúr & Karger, 1996) can be achieved by maintaining the weight of the edges leaving a set of vertices of the sparse graph to be the same as that of the original graph. A much stronger notion of similarity referred to as *spectral similarity* was introduced by Spielman & Teng (2011). Spectral similarity is closely tied to the Laplacian quadratic form of the graphs as defined by equation (6.3). The concept of spectral similarity directly leads to spectral sparsification of graphs; that is to create sparse graphs, which are spectrally similar to the original graph.

Spectral sparsification is a more general abstraction than cut sparsifiers and maintains spectral similarity between the sparsified and original graphs. In particular, spectral sparsification can remove some of the edges in the graph, while maintaining similar adjacency and Laplacian eigenspectra. One of the key features of spectral sparsification is that it keeps the sum of the weights leaving the vertex of a graph constant. A spectral sparsifier is a subgraph of the original graph whose Laplacian quadratic form is approximately the same as the original graph (Spielman & Teng, 2011).

Sparsification involves the creation of a sparse graph $\mathcal{G}_S$ from the original graph $\mathcal{G}$ based on an approximation order of ϵ. The quadratic form induced by graph Laplacian of $\mathcal{G}$ is maintained upto a multiplicative $(1 \pm \epsilon)$ factor by spectral sparsification (Kelner & Levin, 2011). Thus, the sparse graph $\mathcal{G}_S$ is a $(1 \pm \epsilon)$-spectral approximation of $\mathcal{G}$. The approximation order ϵ can vary from zero to unity. The approximation with $\epsilon = 0$ indicates that $\mathcal{G}_S$ is same as original graph $\mathcal{G}$ and none of the edges are sparsified, while $\epsilon = 1$ relaxes the quadratic form induced by the sparse graph to within twice of that induced by the original graph. An approximation of $\epsilon = 1$ leads to a heavily sparsified graph. Denoting the Laplacian matrices of $\mathcal{G}$ and $\mathcal{G}_S$ by $\boldsymbol{L}_{\mathcal{G}}$ and $\boldsymbol{L}_{\mathcal{G}_S}$, respectively, the spectrally sparsified Laplacian satisfies

$$(1 - \epsilon)\boldsymbol{x}^T \boldsymbol{L}_{\mathcal{G}} \boldsymbol{x} \leq \boldsymbol{x}^T \boldsymbol{L}_{\mathcal{G}_S} \boldsymbol{x} \leq (1 + \epsilon)\boldsymbol{x}^T \boldsymbol{L}_{\mathcal{G}} \boldsymbol{x} \tag{6.8}$$

at least with probability $1/2$ with large N for all $\boldsymbol{x} \in \mathbb{R}^N$ (Spielman & Srivastava, 2011). For the example problem considered later, these bounds are much tighter. This tells us that $\boldsymbol{L}_{\mathcal{G}_S}$ holds eigenvalues similar to those of $\boldsymbol{L}_{\mathcal{G}}$. These spectrally similar sparse graphs are found using the spectral sparsification algorithm based on sampling by effective resistance discussed below.

Before we discuss how a graph can be sparsified, let us first follow the works of Bollobás (1998) and Srivastava (2010) to establish an analogy of a graph to an electrical circuit. If the entire graph is viewed as a resistive circuit, we can define a resistance on the individual edges $e = (i, j)$ of the graph. According to Thomson's principle, the potentials and currents

in a resistive circuit distribute themselves so as to minimize the total energy in the network (Bollobás, 1998). This energy minimization principle leads to the concept of effective resistance.

Effective resistance between vertices i and j is the potential difference induced between them when a unit current is injected at one vertex and extracted at the other (Bollobás, 1998; Srivastava, 2010). The effective graph resistance (also called as resistance distance) is the sum of the effective resistance over all the pairs of vertices in the graph $\mathcal{G}$ (Klein & Randić, 1993; Ellens *et al.*, 2011). Rayleigh's monotonicity law states that pairwise effective resistance is a non-increasing function of the edge weights (Mieghem, 2011).

In order to obtain an expression of effective resistance for graph sparsification, we orient the edges of the original weighted undirected graph $\mathcal{G}$ with N vertices and M edges. We can represent any directed graph by a signed edge (e)-vertex (v) incidence matrix $\boldsymbol{B}_{\mathcal{G}} \in \mathbb{R}^{M \times N}$ given by

$$[\boldsymbol{B}_{\mathcal{G}}]_{ev} = \begin{cases} 1 & \text{if } e \in E \text{ and } v \text{ is the head of } e \\ -1 & \text{if } e \in E \text{ and } v \text{ is the tail of } e \\ 0 & \text{otherwise.} \end{cases} \tag{6.9}$$

The row of $\boldsymbol{B}_{\mathcal{G}}$ corresponding to an edge $e = (i, j)$ is given by $(\boldsymbol{p}_i - \boldsymbol{q}_j)$, where $\boldsymbol{p}_i$ and $\boldsymbol{q}_j$ are elementary unit vectors in the i and j directions, respectively. If the edge weights of the graph are represented in a diagonal matrix given by $\boldsymbol{C}_{\mathcal{G}} \in \mathbb{R}^{M \times M}$, we can express the Laplacian matrix based on the incidence matrix as

$$\boldsymbol{L}_{\mathcal{G}} = \boldsymbol{B}_{\mathcal{G}}^T \boldsymbol{C}_{\mathcal{G}} \boldsymbol{B}_{\mathcal{G}} = \sum_{i,j \in E} w_{ij} (\boldsymbol{p}_i - \boldsymbol{q}_j)(\boldsymbol{p}_i - \boldsymbol{q}_j)^T. \tag{6.10}$$

The above relation holds true only for undirected graphs. The incidence matrix $\boldsymbol{B}_{\mathcal{G}}$ and the diagonal matrix $\boldsymbol{C}_{\mathcal{G}}$ for the example graph shown in Fig. 6.1 (left) are given by

$$\boldsymbol{B}_{\mathcal{G}} = \begin{pmatrix} 1 & -1 & 0 & 0 & 0 \\ 1 & 0 & -1 & 0 & 0 \\ 1 & 0 & 0 & -1 & 0 \\ 0 & 0 & 1 & -1 & 0 \\ 1 & 0 & 0 & 0 & -1 \end{pmatrix} \text{ and } \boldsymbol{C}_{\mathcal{G}} = \begin{pmatrix} 0.4 & 0 & 0 & 0 & 0 \\ 0 & 0.5 & 0 & 0 & 0 \\ 0 & 0 & 0.1 & 0 & 0 \\ 0 & 0 & 0 & 0.8 & 0 \\ 0 & 0 & 0 & 0 & 0.2 \end{pmatrix}.$$

For undirected graphs, each edge is counted only once in the incidence matrix and the convention for head and tail of an edge can be fixed arbitrarily. Here, for edge $e = (1, 2)$ of the example graph shown in Fig. 6.1 (left), the head and tail are considered to be vertex 1 and 2, respectively. The corresponding elementary unit vectors for the edge are given by $p_1 = (1, 0, 0, 0, 0)$ and $q_2 = (0, 1, 0, 0, 0)$, which is apparent from the first row of $\boldsymbol{B}_{\mathcal{G}}$ being $\boldsymbol{p}_1 - \boldsymbol{q}_2$.

For an edge corresponding to $e = (i, j)$, the unit current is injected at vertex i and extracted at vertex j. Thus, we set the electrical current across the edge to be $(\boldsymbol{p}_i - \boldsymbol{q}_j)$. The potential induced by this current at the vertices is given by $\boldsymbol{L}_{\mathcal{G}}^+ (\boldsymbol{p}_i - \boldsymbol{q}_j)$, where $\boldsymbol{L}_{\mathcal{G}}^+$ is the Moore–Penrose pseudoinverse of the Laplacian matrix $\boldsymbol{L}_{\mathcal{G}}$ (Srivastava, 2010). The

potential difference across edge $e = (i, j)$ is then given by $(\boldsymbol{p}_i - \boldsymbol{q}_j)^T \boldsymbol{L}_{\mathcal{G}}^+ (\boldsymbol{p}_i - \boldsymbol{q}_j)$. Thus, for unit current, the effective resistance across edge $e = (i, j)$ which corresponds to the potential difference can be expressed as

$$[R_e]_{ij} = (\boldsymbol{p}_i - \boldsymbol{q}_j)^T L_{\mathcal{G}}^+ (\boldsymbol{p}_i - \boldsymbol{q}_j). \tag{6.11}$$

The above expression is used for computing effective resistance of the edges of the graph. The sparsification of the original graph $\mathcal{G} = \{V, E, w\}$ is performed with an algorithm `Sparsify` (Spielman & Srivastava, 2011) to produce a sparse graph $\mathcal{G}_S = \{V, \widetilde{E}, \widetilde{w}\}$ where $\widetilde{w}$ are the weights corresponding to the sparse graph $\mathcal{G}_S$. This algorithm is based on the concept of effective resistance and yields a $(1+\epsilon)$ sparse graph $\mathcal{G}_S$. This sparse graph contains a reduced number of $\mathcal{O}(N \log(N)/\epsilon^2)$ edges. The procedure for sparsification $\mathcal{G}_S = $ `Sparsify`$(\mathcal{G})$ is summarized below.

We first create a list of the edges E with the associated weights of the original graph $\mathcal{G}$. The adjacency and Laplacian matrices of graph $\mathcal{G}$ are constructed from equations (6.1) and (6.2). The Moore–Penrose pseudoinverse of the Laplacian matrix $\boldsymbol{L}_{\mathcal{G}}^+$ is then computed. For each edge in the edge list, the elementary unit vectors, $\boldsymbol{p}_i$ and $\boldsymbol{q}_j$, and edge weights w_e are obtained. Next, the effective resistance $[R_e]_{ij}$ corresponding to each edge is computed from equation (6.11).

A random edge $e = (i, j)$ from the edge list of graph $\mathcal{G}$ is chosen with probability p_e proportional to $w_e [R_e]_{ij}$. The edge e is added to the sparse graph $\mathcal{G}_S$ with the weight given by $\widetilde{w}_e = w_e/q p_e$, where $q = 8N \log_2(N)/\epsilon^2$. We take integer$(q)$ number of samples independently without replacement and sum the weights if an edge is chosen more than once. The resulting graph becomes the sparsified graph $\mathcal{G}_S$ that satisfies equation (6.8) with eigenvalues similar to those of $\mathcal{G}$.

After the random sampling procedure, a sparsified adjacency matrix $\boldsymbol{A}_{\mathcal{G}_S}$ is obtained. For convenience, we define the ratio of the sparsified and original adjacency matrix weights as W_{ij},

$$W_{ij} \equiv \begin{cases} \widetilde{w}_{ij}/w_{ij} & \text{if } (i, j) \in \widetilde{E} \\ 0 & \text{otherwise.} \end{cases} \tag{6.12}$$

This sparsification factor W_{ij} is related to the probability of an edge $e = (i, j)$ of graph $\mathcal{G}$ being sampled. The edges of the original graph that are not sampled during the random sampling procedure have zero weights in the sparsified graph. These edges are cut during sparsification. The spectral sparsification procedure also redistributes the weights of the cut edges among the other edges of the sparsified graph. Thus, cutting of graph edges is compensated by redistribution of the weights to preserve spectral properties of the original graph.

The spectral sparsification algorithm described above produces a $(1 \pm \epsilon)$ expander graph, i.e., sparsifier with strong connectivity properties when $\epsilon \geq 1/\sqrt{N}$, where N is the number of vertices (Spielman & Srivastava, 2011). With the concept of graphs and spectral sparsification now discussed, we consider the application of network analysis to discrete vortex dynamics in the next chapter.

Chapter 7

Vortical Interaction Networks

We apply network analysis to study the dynamics of a collection of point vortices (Saffman, 1992; Newton, 2001). In the present work, the flow is assumed to be two-dimensional, incompressible, and inviscid. The spatial domain $\mathcal{D}$ is taken to be infinitely large and the position of the vortices in the flow field is denoted by $\boldsymbol{r} = (x, y) \in \mathcal{D}$. We consider a collection of N vortices to be in the domain $\mathcal{D}$ resulting in the vorticity field of

$$\omega(\boldsymbol{r}) = \sum_{j=1}^{N} \frac{\kappa_j}{2\pi} \delta(\boldsymbol{r} - \boldsymbol{r}_j), \tag{7.1}$$

where κ_j and $\boldsymbol{r}_j$ are the strength (circulation) and position of the j-th vortex, respectively, and $\delta(\cdot)$ is the Dirac delta function. The motion of the vortices is described by the Biot–Savart law

$$\frac{d\boldsymbol{r_i}}{dt} = \sum_{\substack{j=1 \\ j \neq i}}^{N} \frac{\kappa_j}{2\pi} \frac{\hat{\boldsymbol{k}} \times (\boldsymbol{r}_i - \boldsymbol{r}_j)}{|\boldsymbol{r}_i - \boldsymbol{r}_j|^2}, \tag{7.2}$$

where $\hat{\boldsymbol{k}}$ is the out-of-plane unit normal vector. To determine the trajectories of the vortices, we numerically integrate the above equation. This equation is the basis of the discrete vortex methods that are used to simulate unsteady vortical flows in place of discretizing the two-dimensional Euler equations.

The distance between the vortices is dependent on the location of the two point vortices $|\boldsymbol{r}_i - \boldsymbol{r}_j|$ and the characteristic strength can be established by considering their geometric mean or algebraic mean of circulation. We use the geometric mean of induced velocity as adjacency matrix for the graph representation of a set of point vortices. The interaction between the system of discrete point vortices represented on a complete graph can be sparsified for deriving the sparse vortex interaction model.

In addition to considering the geometric mean of the circulation for the weights, algebraic mean of the circulation was also considered. The computation using the algebraic mean for the weights perform similar to that with the above geometric mean. While we show that geometric mean sufficiently captures the vortex interaction, there may be some room for
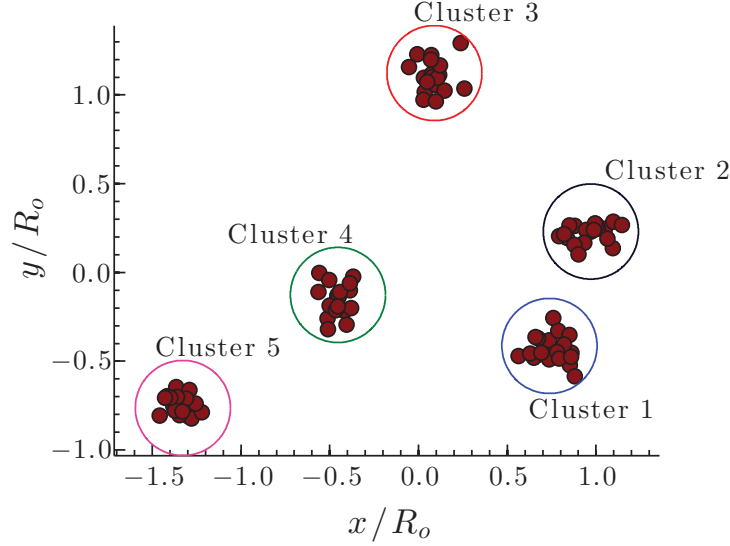
Figure 7.1: The spatial arrangement of $N = 100$ point vortices with five clusters.

optimizing the choice of weights. In what follows we utilize the geometric mean in equation (6.7) for the network weight.

7.1 Sparsification of vortex interactions

In this section, we construct sparsified representation of vortex interactions by sparsifying and redistributing the weights of the connections between the point vortices as discussed in §6.2. We consider a configuration of N point vortices in n_c clusters. This setup allows us to examine the effect of sparsification on a cluster of vortices. The edge weights represented in the adjacency matrix are given by equation (6.7).

Let us first consider a collection of $N = 100$ point vortices with $n_c = 5$ with each cluster containing 20 vortices. The clusters in this setup can be clearly identified by the use of graph clustering algorithms. An algorithm maximizing modularity (Newman, 2004) can be utilized for the identification of clusters. One could also use k-means for cluster identification similar to the work performed by Kaiser *et al.* (2014*a*). The point vortices in a particular cluster are given a normal distribution in space with a radial standard deviation of $\sigma_r = 0.2$. The strength of the point vortices, κ_i, within the individual clusters have a normal distribution with the mean of $\bar{\kappa} = 0.1$ and a standard deviation of $\sigma_\kappa = 0.01$. The setup for this configuration is shown in figure 7.1. The positions of the clusters are normalized by the average radial distance of the centroid of the clusters from the geometric center of the system (R_o).

The original point vortex distribution modeled as a complete graph is shown in figure 7.2 (top left). The colors of the point vortices (network vertices) indicate their unweighted

degree (number of edge connections). As the original graph here is a complete graph $\mathcal{K}_N$, each vortex is connected to every other vortex. Thus, the unweighted degree of each vortex in this example is $N - 1 = 99$. The sparsity pattern of the adjacency matrix for the complete graph $\boldsymbol{A}_{\mathcal{K}_N}$ is shown in figure 7.2 (top right). We also note in the figure the sparsity index S, defined as $S \equiv n_{\mathrm{non\text{-}zero}}/N^2$ with $n_{\mathrm{non\text{-}zero}}$ being the number of non-zero weights in the adjacency matrix and N being the number of vortices. As the diagonal elements of the adjacency matrix have zero weights, $n_{\mathrm{non\text{-}zero}} = N(N - 1)$ for the complete graph. For $N = 100$, a sparsity index of $S = 0.99$ is obtained for the original graph.

We now perform spectral sparsification on the original graph ($\mathcal{G} = \mathcal{K}_N$) using the algorithm $\mathcal{G}_S = \texttt{Sparsify}(\mathcal{G})$ described in §6.2 to obtain the spectrally similar sparse representations of the complete graph based on approximation order ϵ. The corresponding adjacency matrix, $\boldsymbol{A}_{\mathcal{G}_S}$ can also be found. The vortex network for sparse graph and the sparsity pattern of $\boldsymbol{A}_{\mathcal{G}_S}$ corresponding to approximation order of $\epsilon = 0.5$ are shown in Fig. 7.2 (middle). We observe that the number of edges (connections) between the vortices in cluster 3 and 5 are reduced. Because the weights of the adjacency matrix are inversely proportional to the distance between the vortices, a large number of edges between the vortices of the clusters with larger distances are cut during sparsification. The sparsity index decreases from $S = 0.99$ for the original complete graph to $S = 0.741$ for the sparse graph ($\epsilon = 0.5$), reducing the number of connections by approximately 25 percent.

The vortex network and sparsity patterns for approximation order of $\epsilon = 1$ are shown in figure 7.2 (bottom). We observe dense representation of the connections between the clusters 1 and 2. Thus, the proximity in clusters is identified both in the network structure and the sparsity patterns. Also, we realize from the sparsity patterns that the connections between the vortices in a particular cluster are maintained while majority of the inter-cluster ties are cut resulting in a sparse graph. The number of connections in the sparse graph for $\epsilon = 1$ are reduced dramatically by nearly 60 percent with $S = 0.4006$.

For weighted graphs, the effective resistance is computed in such as way so as to maintain spectral similarity. The eigenspectra (σ and λ) of the adjacency and Laplacian matrices for the sparse and original graphs are compared in figure 7.3. We observe from figure 7.3 that the spectra of the sparse and original configurations are in good agreement as expected. The second smallest eigenvalue of the Laplacian matrix represents the spectral gap or algebraic connectivity of the graph, i.e., vertices connected by at least a single path (Newman, 2010). As observed from Fig. 7.3, the spectral gap is greater than zero for original and sparse graphs indicating that the graph is connected. Thus, sparsification preserves the connectivity properties of the original graph. The sparsified graphs slightly underpredict the maximum eigenvalues of the adjacency and Laplacian matrices compared to the original graph. The preservation of spectral properties is attractive if the sparsified network is to be used to describe the dynamics of the vortices. We expect the overall motion of the vortices to remain similar with sparsified representations of the vortex interactions.

Sparsification helps identify the individual clusters by creating subgraphs within a graph where the density of the edges between vertices is much greater than that outside it. The spectral sparsification procedure leads to the reduction in the number of edges to $\mathcal{O}(N \log(N)/\epsilon^2)$
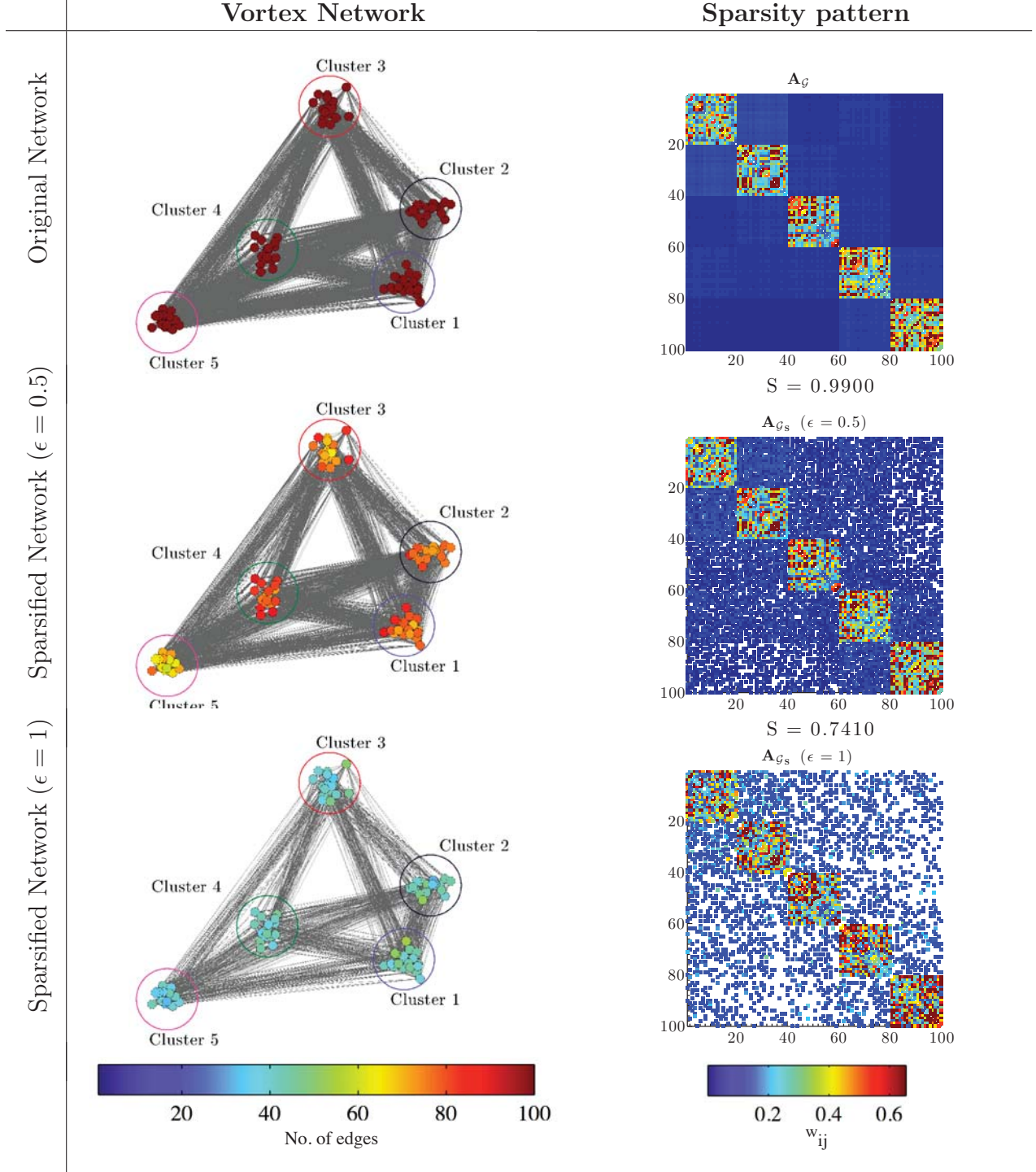
Figure 7.2: Original and sparsified graphs and their respective sparsity patterns of the adjacency matrix for $N = 100$ vortices. The color of the nodes of the vortex network represents the unweighted connections (number of connected edges) of the individual point vortices. The color in the sparsity patterns of the adjacency matrix indicates the adjacency weights w_{ij} for original graph $\boldsymbol{A}_{\mathcal{G}}$ and $\widetilde{w}_{ij}$ for sparse graphs $\boldsymbol{A}_{\mathcal{G}_S}$. The empty white spaces indicate sparsity in the adjacency matrix. Sparsity index is $S \equiv n_{\text{non-zero}}/N^2$, where $n_{\text{non-zero}}$ is the number of non-zero weights (elements) in adjacency matrix and N is the number of vortices. The colored circles in the vortex network represent the individual cluster groups.
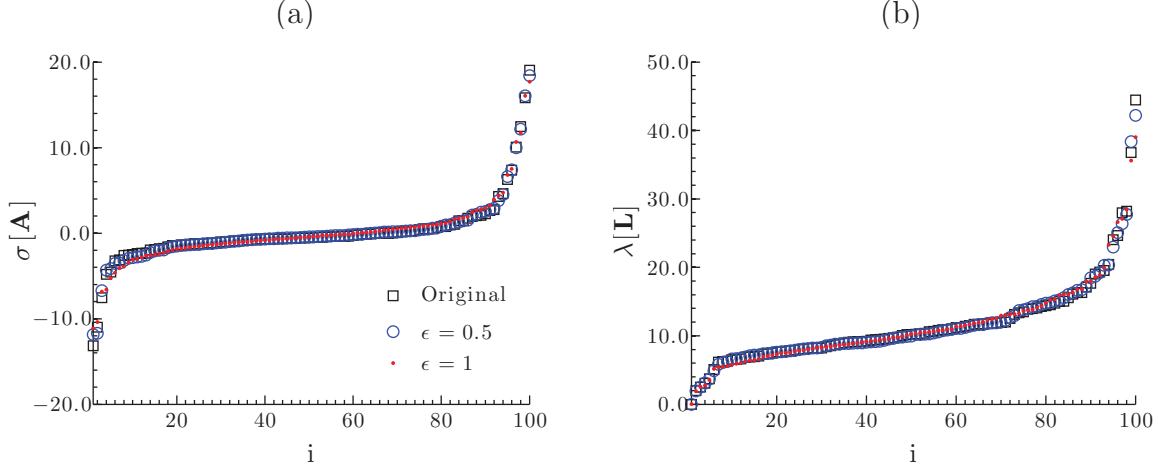
Figure 7.3: Eigenvalue spectra of (a) adjacency and (b) Laplacian matrices of the sparsified graphs with $\epsilon = 0.5$ and 1 in comparison to the original graph.

for large N. We examine the performance of spectral sparsification on the current example for increasing the total number of vortices. As in the example that was previously considered, we maintain a constant number of clusters $n_c = 5$ but increase the number of vortices in each cluster N/n_c. The sparsity patterns of the adjacency matrix for $N = 500$ and 2000 with approximation order $\epsilon = 1$ are shown in Fig. 7.4. We observe that as the number of vortices increases, the adjacency matrix of the sparsified graph becomes increasingly sparse. Similar to the case with $N = 100$ vortices, the majority of the ties within a cluster are maintained while a large number of inter-cluster ties are cut. The sparsity index decreases from $S = 0.1784$ to 0.0707 for $N = 500$ to 2000, which is a substantial amount of sparsification. Let us further show the sparsity index S for increasing N with different approximation order ϵ in Fig. 7.5. The sparsity index S decreases with an increase in ϵ and the number of vortices. The expected behavior of the sparsity index $S = \mathcal{O}(N \log(N))/(N^2) = \mathcal{O}(\log(N)/N)$ is observed for larger N. The trend deviates from the expected behavior for lower N as the availability of the connections for redistribution of the weights of the sparsified connections decreases.

We observe that the sparsification algorithm provides us with a heavily sparsified model to produce a computationally tractable representation of the vortex-to-vortex interaction. We further note that the sparsification algorithm can be easily parallelized, which is attractive to further reduce the computational wait time. The bulk motion of clusters of point vortices could be tracked effectively by tracking their individual centroids. The present approach may lead to algorithms similar to fast particle summation methods where near and far-field effects are taken into consideration (Greengard & Rokhlin, 1987).
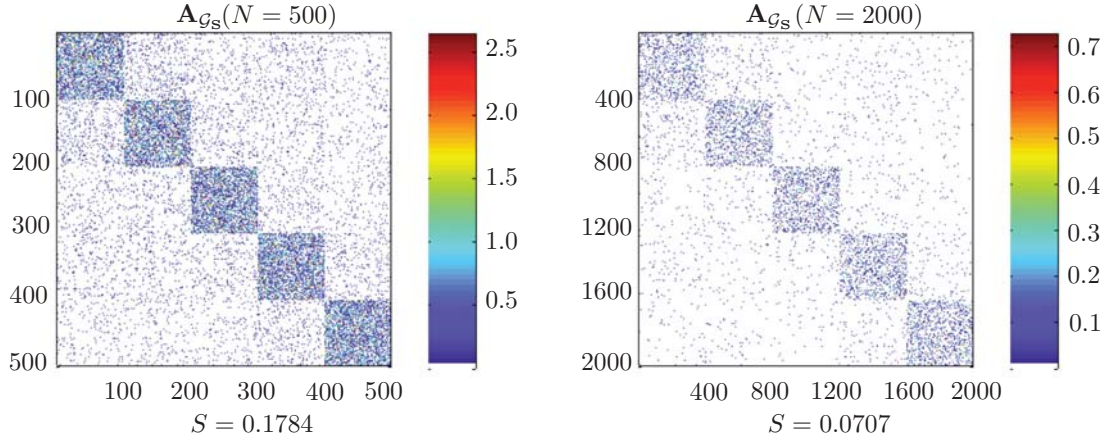
Figure 7.4: Sparsity patterns of adjacency matrix for $N = 500$ and 2000 for approximation order $\epsilon = 1$. The color in the sparsity patterns of the adjacency matrix denotes the adjacency weights $\widetilde{w}_{ij}$ with the empty white space indicating sparsity.
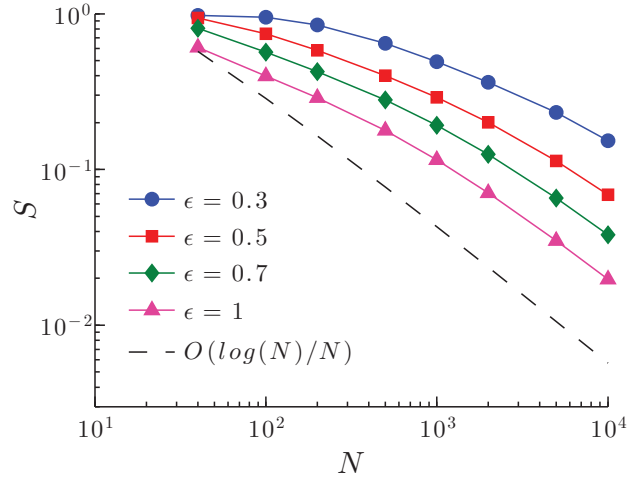

Figure 7.5: Variation of sparsity index S for sparsification with increasing number of point vortices. The reference black line represents $\log(N)/N$.

7.2 Sparsified-dynamics model

The sparsified vortex interactions can be used for analyzing the dynamics of the system of discrete point vortices. Spectral sparsification can be viewed as adjusting the strength of the vortices in the Biot-Savart law through the sparsification factor W given by equation (6.12). We can incorporate the weights of the sparse graph into the Biot-Savart law as

$$\frac{d\boldsymbol{r_i}}{dt} = \sum_{\substack{j=1 \\ W_{ij} \neq 0}}^{N} W_{ij} \frac{\kappa_j}{2\pi} \frac{\widehat{\boldsymbol{k}} \times (\boldsymbol{r}_i - \boldsymbol{r}_j)}{|\boldsymbol{r}_i - \boldsymbol{r}_j|^2}, \tag{7.3}$$

where W_{ij} is the sparsification factor. The above expression significantly reduces the amount of computation compared to the original Biot–Savart law, because the sparsification has made a significant number of elements of W to be zero, as seen in figures 7.2 and 7.4.

For evaluating the effect of sparsification on dynamics of the point vortices, we consider the same example presented in §7.1 with $N = 100$ vortices as the initial condition. The objective here is to accurately capture the dynamics of the vortex clusters with the sparsified Biot–Savart law given by equation (7.3). The bulk motions of the clusters of point vortices are well represented by the centroid of the individual clusters. The original and the sparsified dynamics are given by equations (7.2) and (7.3), respectively, and are integrated in time with the fourth-order Runge–Kutta method. The results from the sparsified-dynamics model are shown in figures 7.6 and 7.7.

For the present analysis, time is non-dimensionalized by considering the cumulative circulation of the vortices of the cluster (Γ) and average radial distance of the centroid of the clusters from the geometric center of the overall system at the initial time (R_o). As the advective velocity of an isolated cluster of point vortices of strength Γ at R_o is given by $u^\star = \Gamma/2\pi R_o$, the non-dimensional time can be deduced as $tu^\star/R_o = t\Gamma/2\pi R_o^2$. In the current example, each individual cluster has a collection of vortices with their strength having a mean of $\bar{\kappa} = 0.1$ (with a normal distribution). Thus, for n vortices in a cluster, $\Gamma = n\bar{\kappa}$. The error in position of the centroid of the clusters for the sparsified setting with respect to the original setting given by $|\boldsymbol{r}_\epsilon - \boldsymbol{r}|$ is non-dimensionalized by the average radial distance of the centroid of the clusters from the geometric center of the system at the initial time (R_o).

Let us consider the case where sparsification is performed only once to determine the sparsification factor W_{ij} before initiating the time integration. The same sparsification factor is used throughout the time integration. This procedure is inexpensive as sparsification is performed only once *a priori*. The trace of the positions of the centroid of the individual clusters and their error for approximation orders of $\epsilon = 0.5$ and 1 for a single sparsification are shown in figures 7.6 (top) and 7.7 (top), respectively. Considering the number of connections cut between the vortices for sparse approximations, the trajectories of the centroid of the clusters based on sparse vortex dynamics agrees reasonably with those from full dynamics. On comparing the errors, we find that the errors with approximation order of $\epsilon = 0.5$ is less than those with $\epsilon = 1$, which is expected. Despite the Biot–Savart law being nonlinear, the present sparsified approach achieves a reasonable agreement with the full nonlinear solution.

If the clusters of vortices are far from each other, the connections cut between their vortices do not cause a large change in the dynamics while the connections cut between clusters close to each other affect the dynamics considerably. As time progresses, the relative distance between vortices change, resulting in an increase in error. For $t\Gamma/2\pi R_o^2 > 1$, we observe that the errors in sparse vortex dynamics increases to $\approx 0.5 R_o$. As the adjacency weights w_{ij} and the sparsification factor W_{ij} are based on the initial position of the vortices, the ratio does not hold over large times. This calls for adjustment of the weights and periodic sparsification to adapt to the dynamically changing position of the vortices.

We thus consider resparsification of the graph representing the system of point vortices periodically at $(0.1t\Gamma/2\pi R_o^2)$ and $(0.01t\Gamma/2\pi R_o^2)$ for both approximation orders. The trace of the centroids and error for approximation orders of $\epsilon = 0.5$ and 1 with resparsification are shown in middle and bottom subfigures, respectively, of figures 7.6 and 7.7. We observe that the error decreases significantly with resparsification. The error in position reduces from $\mathcal{O}(10^{-1})$ to $\mathcal{O}(10^{-2})$ with resparsification. We notice that the centroid trajectories based on the sparse and original calculations become increasingly similar with resparsification. Resparsification updates the sparsification factor periodically based on the position and strength of the vortices and decreases the error by an order of magnitude. Thus, the nonlinear evolution of discrete vortex dynamics is well predicted by the sparsification techniques.

One of the advantages of sparsification is the decreased computational cost due to increased sparsity of the connections between the vortices. This could potentially lead to design of faster algorithms based on sparsification strategies. Let us first evaluate the offline cost of computing effective resistance and random sampling required for spectral sparsification. The time required for computing effective resistance t_r and time required for random sampling t_s is shown in figures 7.8(a) and (b) respectively. All computations were performed in MAT-LAB on an iMac with 3.4 GHz Intel Core i7 processor. We can observe that for each edge, the computation time of effective resistance is $\mathcal{O}(\log(N))$, hence requiring $\mathcal{O}(N^2 \log(N))$ for the overall effective resistance computation. The random sampling procedure takes $\mathcal{O}(N^2)$ time for all the approximation orders. We compare the computational time t_d required at each step of numerical integration of the Biot–Savart law for the original and sparse configuration. We can observe from figure 7.8(c) that the original configuration takes $\mathcal{O}(N^2)$ time equivalent to the number of edges in the complete graph, while for the sparse configuration the computation time is reduced to $\mathcal{O}(N \log(N))$.

There is always a tradeoff amongst the level of sparsification, the error that appears in the dynamics, and the associated computational cost. The sparser the network is, the faster the computation can become but may compromise accuracy. To increase the computational accuracy, resparsification can be performed but can introduce an additional computational load. We evaluate the computational cost for numerical integration until a total time of $0.1t\Gamma/2\pi R_o^2$. The time required for resparsification and numerical integration for the two different resparsification frequencies (performed every $0.1t\Gamma/2\pi R_o^2$ and $0.01t\Gamma/2\pi R_o^2$) considered in this work for original and sparse configuration with $\epsilon = 1$ is shown in figure 7.9. It should be noted that for the resparsification performed every $0.1t\Gamma/2\pi R_o^2$, resparsification is performed once for the total time considered. For resparsification conducted every
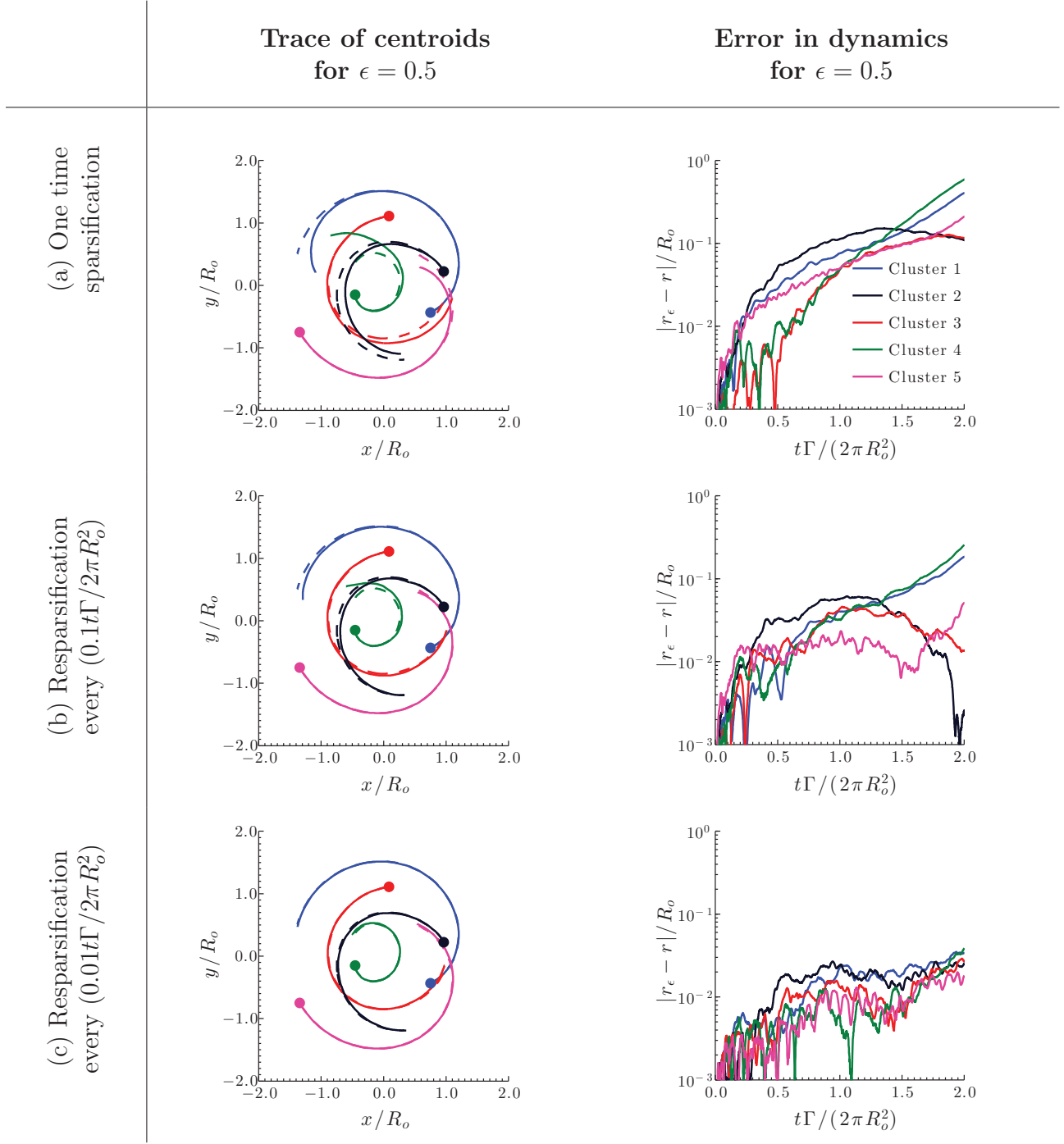
Figure 7.6: Trajectories of the centroids (left) and error in position of centroids (right) of the vortex clusters based on sparse graph ($\epsilon = 0.5$) and original graph with time for $N = 100, \bar{\kappa} = 0.1$. (a) trajectories and error based on sparsification performed only at the initial step while (b) results based on resparsification performed at every $(0.1 t\Gamma/2\pi R_o^2)$ and (c) results based on resparsification performed at every $(0.01 t\Gamma/2\pi R_o^2)$. The full nonlinear solution is shown with dashed lines.
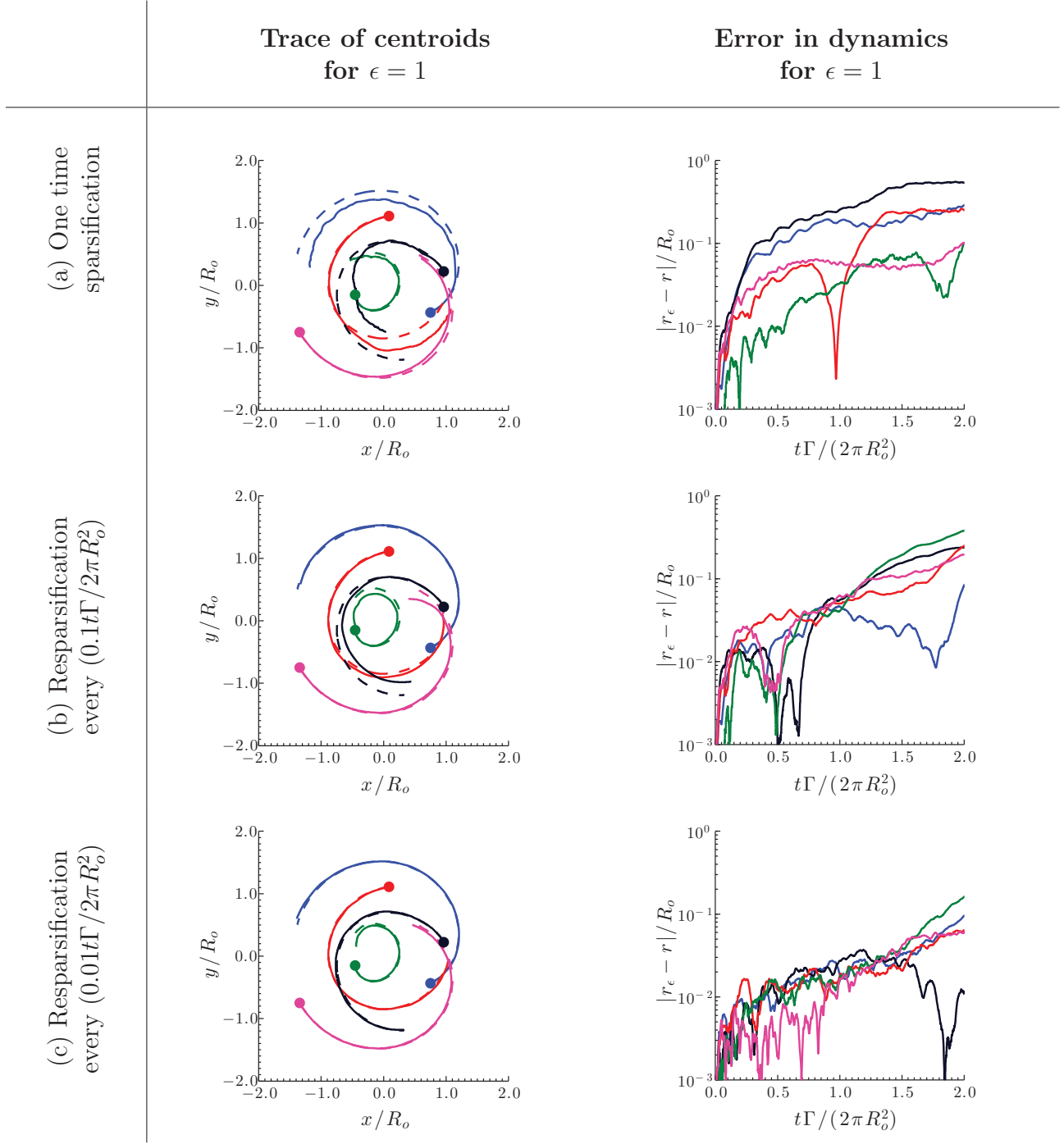
Figure 7.7: Trajectories of the centroids (left) and error in position of centroids (right) of the vortex clusters based on sparse graph ($\epsilon = 1$) and original graph with time for $N = 100, \bar{\kappa} = 0.1$. (a) trajectories and error based on sparsification performed only at the initial step while (b) results based on resparsification performed at every $(0.1t\Gamma/2\pi R_o^2)$ and (c) results based on resparsification performed at every $(0.01t\Gamma/2\pi R_o^2)$. The full nonlinear solution is shown with dashed lines.
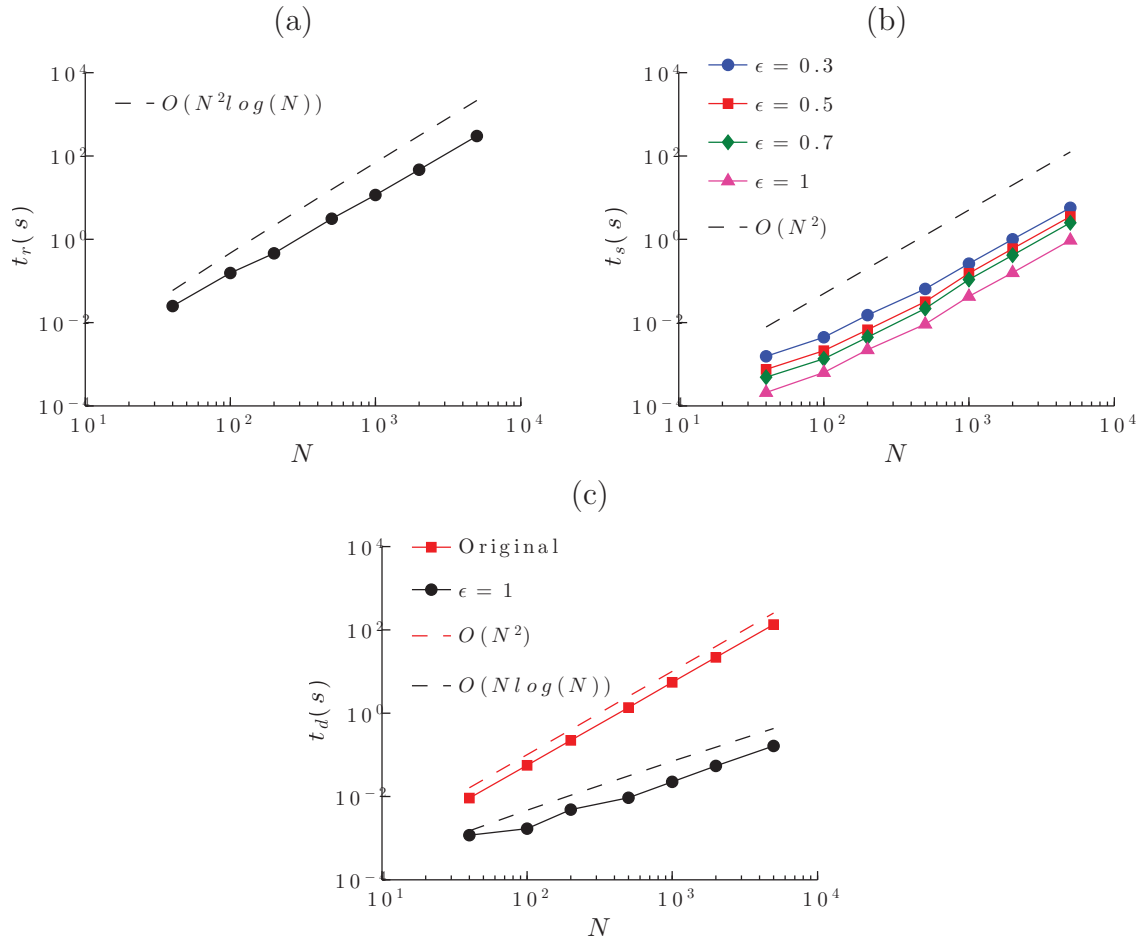
Figure 7.8: The time required for computation of (a) effective resistance and (b) random sampling for different approximation orders for one-time sparsification. The dashed lines indicate the expected trends. (c) Time required for numerical integration at each step for original and sparsified configuration with $\epsilon = 1$.
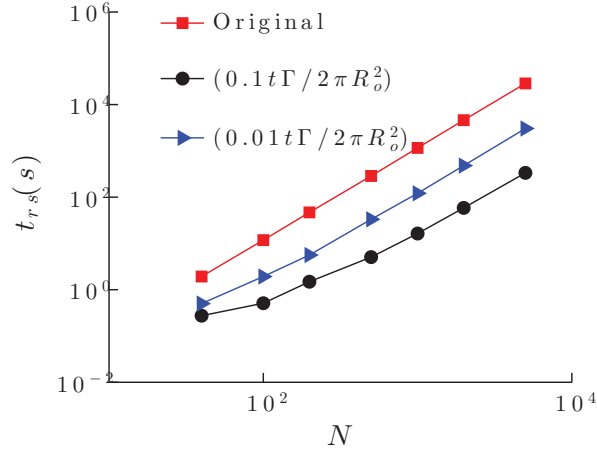
Figure 7.9: The time required for numerical integration for a total time of $0.1t\Gamma/2\pi R_o^2$ with different resparsification frequencies.

$0.01t\Gamma/2\pi R_o^2$, resparsfication is performed ten times. We can see that the time required for resparsification at every $0.1t\Gamma/2\pi R_o^2$ is considerably less compared to the original configuration. With increase in resparsification frequency, though the time required is less compared to the original configuration, there is increased cost associated with resparsification.

To illustrate that the trajectory prediction using sparsification cannot be performed naively, we compare the results from spectral sparsification with those based on random edge removal (without redistribution of edge weights). We keeep the number of cuts identical to that achieved by spectral sparsification for fairness. The sparsity patterns for random cuts with sparsity $S = 0.7410$ and 0.4006 and the corresponding Laplacian eigenspectra are shown in figure 7.10. We observe that the spectra from the randomly sparsified graphs grossly under-predicts that of the original graph.

The trace of the positions of the centroid of the individual clusters and their error for random cuts with sparsity $S = 0.7410$ and 0.4006 for one-time sparsification are shown in figure 7.11. The random-cut approximation performs poorly as compared to spectral sparsification and the dynamics of the centroid of the vortex clusters are not captured. As the connections between the vortices are randomly cut, the centroids of the clusters move slower compared to the original configuration as expected. This is due to the loss of induced velocity with the absence of weight redistribution from random sparsification. Spectral sparsification, on the other hand, redistributes the weights to prevent the loss of the overall interactions amongst the set of point vortices.

It is well known that fast multipole methods (Greengard & Rokhlin, 1987) can also reduce the $\mathcal{O}(N^2)$ velocity evaluation significantly. The particle-box and box-box schemes reduce the computational complexity from $\mathcal{O}(N^2)$ to $\mathcal{O}(N\log(N))$ and $\mathcal{O}(N)$, respectively. As seen in this section, spectral sparsification reduces the computational load to $\mathcal{O}(N\log(N))$ for computing the velocity of the vortices. Fast multipole methods approximate the effect of
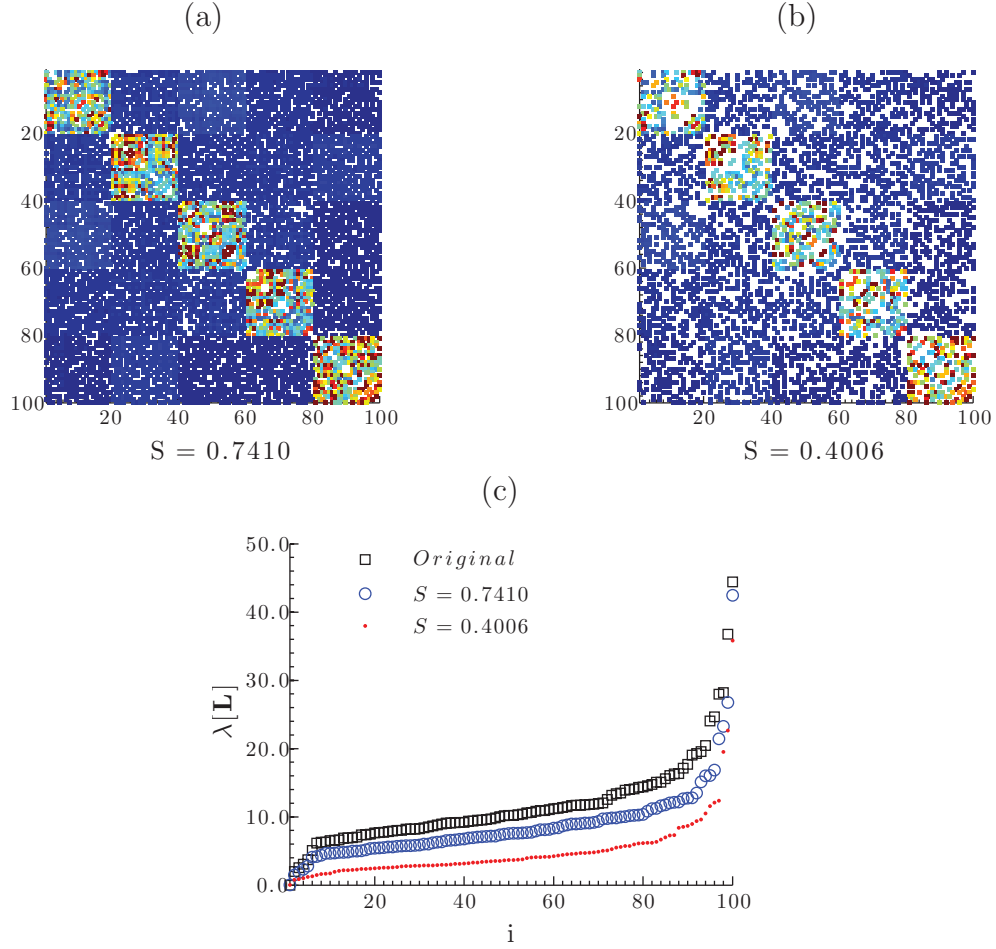
Figure 7.10: Sparsity patterns of the adjacency matrix for $N = 100$ vortices with random cuts with sparsity (a) $S = 0.7410$ and (b) $S = 0.4006$. The color in the sparsity patterns of the adjacency matrix indicates the adjacency weights $\widetilde{w}_{ij}$ for $S = 0.7410$ and 0.4006. (c) Eigenvalue spectra of Laplacian matrices of the randomly sparsified graphs with $S = 0.7410$ and 0.4006 in comparison to the original graph. The legend for the sparsity patterns is similar to that of sparsity patterns in figure 7.2.

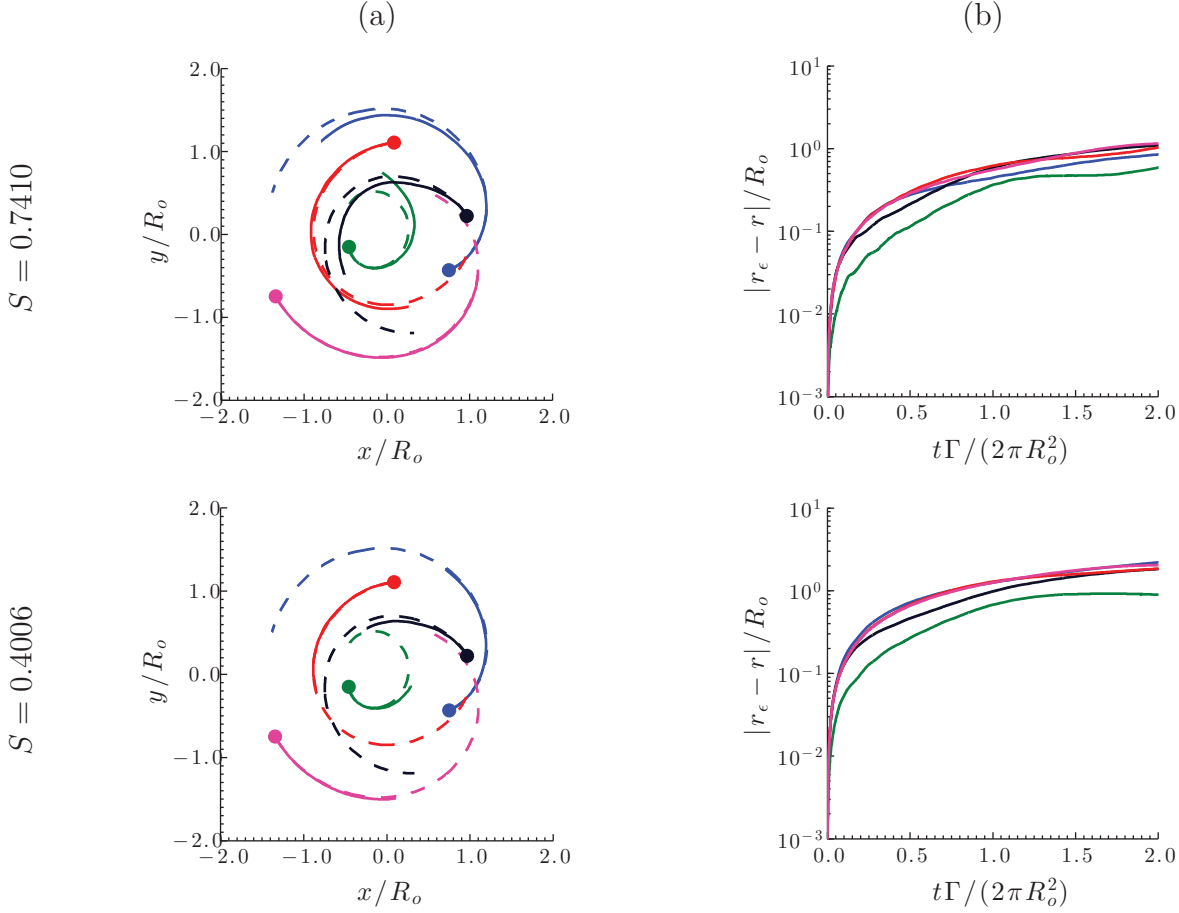Figure 7.11: (a) Trajectories of the centroids and (b) error in position of centroids (right) of the vortex clusters based on random cuts with sparsity $S = 0.7410$ and 0.4006 for $N = 100, \bar{\kappa} = 0.1$.

cluster of particles at a certain distance by multipole expansions and organizing the particles to a hierarchy of clusters (Cottet & Koumoutsakos, 2000). In order to compensate for the sparsified connections in spectral sparsification, the weights are redistributed among the other edge connections to compute the sparsified dynamics. In an analogy to fast multipole methods, the interaction list depends on the connections that have direct impact on the vortices and computational accuracy may degrade when the vortices move in space. Similar to reconstruction of tree data structures in fast multipole methods, performing resparsification periodically increases the accuracy by re-evaluating the associated weights as the positions of the vortices evolve over time. We note that even with sparsification, invariants of discrete vortices are conserved as discussed below.

7.2.1 Conservation properties

For a discrete set of point vortices, angular impulse and linear impulse are among the conserved quantities. The coordinates of center of vorticity obtained from linear impulse and the length of dispersion about the center of vorticity obtained from angular impulse, when the strength of vortices is of the same sign, remain constant. The center of vorticity (X, Y) and length of dispersion of vorticity D are given by

$$X = \frac{\sum_{i=1}^{N} \kappa_i x_i}{\sum_{j=1}^{N} \kappa_j}, \quad Y = \frac{\sum_{i=1}^{N} \kappa_i y_i}{\sum_{j=1}^{N} \kappa_j}, \tag{7.4}$$

$$D^2 = \frac{\sum_{i=1}^{N} \kappa_i \{(x_i - X)^2 + (y_i - Y)^2\}}{\sum_{j=1}^{N} \kappa_j}, \tag{7.5}$$

where κ_i is the strength of the i-th vortex and (x, y) are the vortex positions (Batchelor, 2000; Newton, 2001). The circulation for n vortices in a cluster is $\Gamma = n\bar{\kappa}$. The total circulation of the system of $n_c = 5$ clusters is given by $\Gamma_t = \sum_{i=1}^{N} \kappa_i = n_c \Gamma$. Another conserved quantity is the Hamiltonian. The Hamiltonian is defined as the interaction energy of the system of point vortices and is given by

$$H = -\frac{1}{4\pi} \sum_{i,j=1, i \neq j}^{N} \kappa_i \kappa_j \log \sqrt{(x_i - x_j)^2 + (y_i - y_j)^2}. \tag{7.6}$$

We non-dimensionalize the Hamiltonian using the total circulation of n_c clusters and the average radial distance of centroid of the clusters at initial time R_o.

We compare the error in the Hamiltonian $(H_\epsilon(r/R_o) - H(r/R_o))/\Gamma_t^2$, the center of vorticity $((X_\epsilon - X)/R_o, (Y_\epsilon - Y)/R_o)$, and the square of length of dispersion of vorticity $(D_\epsilon^2 - D^2)/R_o^2$ for approximation orders of $\epsilon = 0.5$ and 1 over time in figure 7.12. The preservation of center of vorticity and length of dispersion implies the conservation of linear and angular impulse. Here, the variables with subscript ϵ denote those based on a sparsified model. We observe that the error in the Hamiltonian is of $\mathcal{O}(10^{-4})$ for $\epsilon = 0.5$ and $\mathcal{O}(10^{-3})$ for $\epsilon = 1$. The error in the square of dispersion is of $\mathcal{O}(10^{-6})$ while the error in the center of vorticity is of $\mathcal{O}(10^{-8})$ with sparsification. While not shown, resparsification of these vortices periodically performed at every $(0.1 t\Gamma/2\pi R_o^2)$ and $(0.01 t\Gamma/2\pi R_o^2)$ maintain similar error levels for the invariants. We also note that the circulation of each vortices has not been altered, which conserves the individual and overall circulation over time.

As seen in §6.2, sparsification by effective resistance is based on the energy-minimization principle. The effective resistance is defined such that the total energy of the system remains constant. This is reflected well in the conservation of the Hamiltonian representing the interaction energy of the discrete point vortices. In addition, sparsification preserves other invariants including linear and angular impulse of the discrete set of point vortices. We note in passing that even with resparsification, the invariants were observed to be conserved. The conservation of the invariants for the sparse configurations further encourages the applicability of sparsification strategies on discrete vortex dynamics.
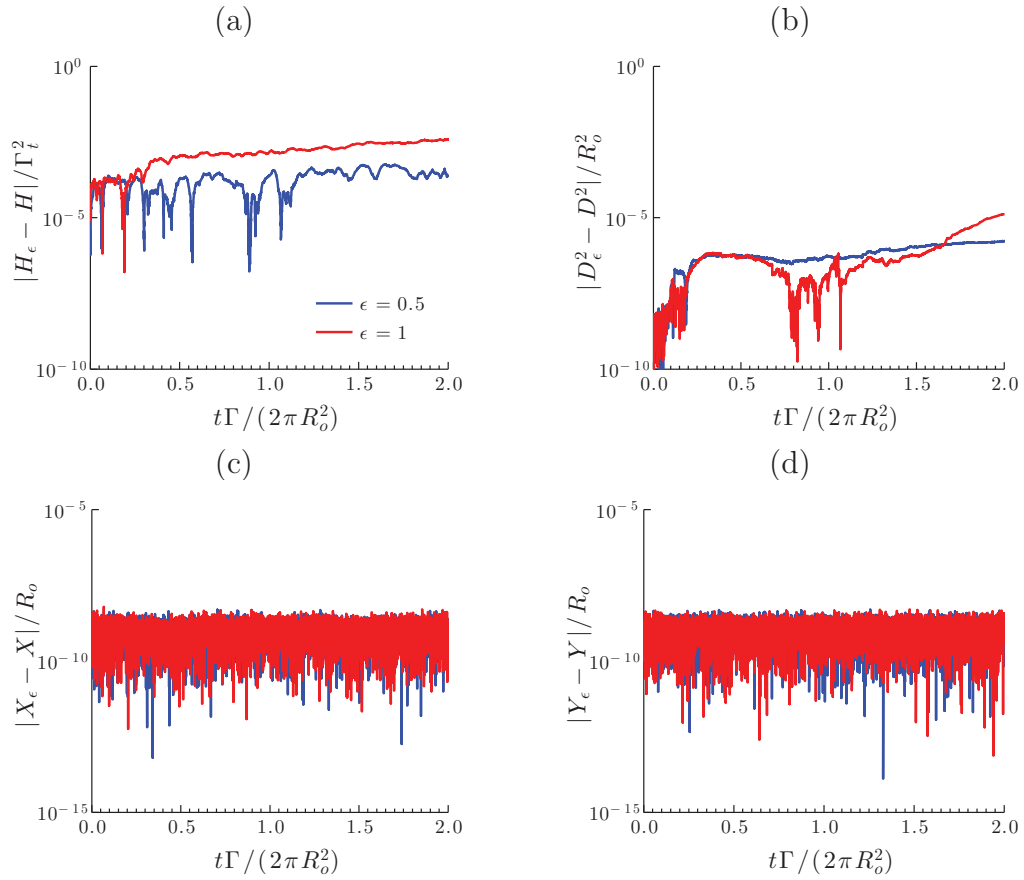
Figure 7.12: Error in the (a) Hamiltonian, (b) square of length of dispersion, (c) x-position of center of vorticity and (d) y-position of center of vorticity based on single sparsification for $N = 100, \bar{\kappa} = 0.1$ and $\epsilon = \{0.5, 1\}$.

7.2.2 Comparison with Reduced-order model

We comment on the similarities and differences between the present sparsified-dynamics model and the reduced-order model. Both models share the general objective of deriving a model that captures the full-order physics in a distilled manner. Reduced-order models achieve such goals by reducing the dimension of the state variable. One such technique is the Galerkin projection of the Navier–Stokes equations using a set of spatial bases (Noack *et al.*, 2005; Rowley *et al.*, 2004), such as those determined from POD (Berkooz *et al.*, 1993; Holmes *et al.*, 1996). One can further consider incorporating the effect of input and output dynamics by using balanced truncation or the eigensystem realization algorithm (Rowley, 2005; Ma *et al.*, 2009). The resulting reduced-order models are generally described by ordinary-differential equations for the temporal coefficients with reduced dimensions.

On the other hand, the present sparsified-dynamics model does not reduce the dimensionality of the state variable. We instead focus on reducing the number of connections used to capture the overall dynamics of the fluid flow. The reduction in the number of connections is performed based on the concepts from network analysis and graph theory. Although we cut a large number of the edges in the graph representation of the dynamical interaction, we redistribute the weights associated with the edges to maintain properties of the graph. This procedure is based upon approximating the spectral properties of the graph and does not require selecting the spatial basis functions unlike the Galerkin-projection based models. One nice feature of the sparsified-dynamics model is its ability to conserve physical variables such as the Hamiltonian, angular impulse, and linear impulse, as discussed previously. Hence, the sparsified dynamics is able to predict the full dynamics as demonstrated by the example with discrete vortices. By highlighting the interactions amongst a set of vortices, we are able to determine which interactions amongst the vortices are important in guiding the overall motion of vortices.

We believe the sparsified-dynamics model has promising potential to model various types of fluid flow by considering the modal structures as a abstraction of graph nodes. The application of sparsified dynamics models towards flow control problems may also become fruitful as the the computational time necessary to capture the complex behavior of the flow is reduced and the interaction of nodes or flow structures are well-captured, which has been a lacking feature in linear dynamics model and linear stability analysis. We anticipate that the presently proposed model can lead to potential feedback control of fluid flow (Bagheri *et al.*, 2009; Ahuja & Rowley, 2010) but with nonlinear interactions emphasized. One of the open questions in extending the sparsified dynamics model for a wide variety of fluid flow problems is the choice of the variables or modes to be used for graph nodes. This issue is currently being examined and will be reported in upcoming studies. In the next chapter, we extend the vortical interaction analysis to turbulent flows using network theory.

Chapter 8

Turbulent Interaction Networks

In this study, we focus on unforced two-dimensional isotropic turbulence in a periodic box and assess the influence of the vorticity distribution over a Cartesian domain. Here, the two-dimensional vorticity field reduces to $\boldsymbol{\omega}(\boldsymbol{x}, t) = \omega(x, y, t)\hat{\mathbf{e}}_z$ with $\hat{\mathbf{e}}_z$ denoting the unit normal plane vector. Modeling the vortical component for each discrete Cartesian element as a line vortex, we can evaluate how fluid elements influence each other, as depicted in Fig. 8.1. We define, $\kappa_i = \omega(\boldsymbol{x_i})\Delta x \Delta y$ is the circulation of fluid element i with side lengths of Δx and Δy. The superposition of the induced velocity from all other fluid elements provides the advective velocity of the fluid element. Detailed discussions on using point vortices to develop the network-theoretic framework for describing unsteady vortical flows can be found in Nair & Taira (2015) and previous chapter. We note in passing that adjacency matrices are commonly defined with positive weights as considered here, but they can be relaxed to accommodate positive and negative weights within the context of vortical interactions. This point will be revisited later.

In the present study, the influence from the neighboring periodic vortex images are also accounted for in the analysis. This formulation yields a full matrix except for its diagonal entries that are identically zero. In assessing the strength of the vortical interaction between two fluid elements, we utilize Eq. (6.6) to perform network analysis to extract the spatial connectivity structure. This approach has been successful in capturing the nonlinear vortex dynamics and modeling the trajectories of vortex clusters (Nair & Taira, 2015). The average induced velocity is used as the adjacency matrix. Note that the geometric mean can be alternatively chosen and yields similar results. In general, the adjacency matrix can be formulated in an asymmetric manner:

$$A_{ij} = \begin{cases} \phi u_{i \to j} + (1 - \phi)u_{j \to i} & \text{if } i \neq j \\ 0 & \text{otherwise.} \end{cases} \tag{8.1}$$

Here the parameter ϕ takes a value between 0 and 1. For the aforementioned symmetric formulation in Eq. (6.6), ϕ is selected as $1/2$. When $\phi = 0$ and 1, the adjacency matrix A_{ij} are defined by the velocity imposed to the other elements ($A_{ij} = u_{j \to i}$) and upon themselves ($A_{ij} = u_{i \to j}$), respectively, for $i \neq j$. We mainly focus on the use of the symmetric adjacency
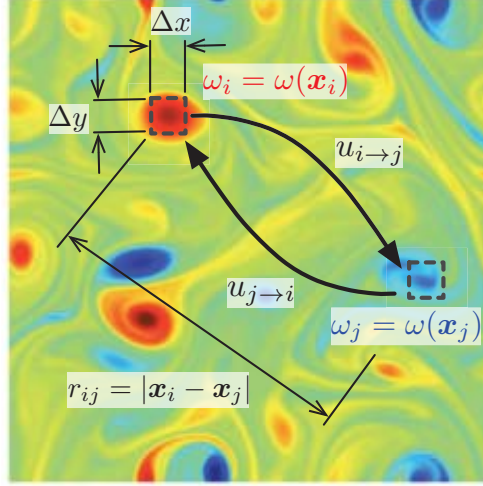
Figure 8.1: Interaction of fluid elements in two-dimensional turbulence. The strength of the vortical interaction between elements i and j having vorticity ω_i and ω_j is quantified through the induced velocities $u_{i\to j}$ and $u_{j\to i}$, respectively. For discretizing the Cartesian domain, we take n_x and n_y points in the horizontal and vertical directions, respectively, providing the adjacency matrix $\boldsymbol{A}$ of size $n \times n$ with $n = n_x n_y$. Shown in the background with a contour plot is the corresponding vorticity field with initial $Re(t_0) = 814$ at $t = 18$.

matrix in this work but will consider the asymmetric formulation briefly to highlight the difference from a physical point of view in the next section. We note in passing that the theoretical tools for symmetric adjacency matrices are more widely available compared to the asymmetric matrices.

The flow field analyzed in this study is obtained from direct numerical simulation on a square bi-periodic computational domain $(x, y) \in [0, L] \times [0, L]$ with a grid size of $m_x \times m_y = 1024 \times 1024$. The unforced two-dimensional incompressible isotropic turbulent flow is simulated by numerically solving the two-dimensional vorticity transport equation

$$\frac{\partial \omega}{\partial t} + u_j \frac{\partial \omega}{\partial x_j} = \frac{1}{Re} \frac{\partial^2 \omega}{\partial x_j \partial x_j}, \tag{8.2}$$

where $\boldsymbol{u}$ and ω are the velocity and vorticity variables, respectively. The simulation is performed with the Fourier spectral method and the fourth-order Runge–Kutta time integration scheme (Canuto *et al.*, 1988). The vorticity field is initialized with a smooth distribution comprised of a large number (≈ 100) of superposed vortices (Taylor, 1918) with random strengths, core sizes, and locations. The initial core sizes are selected to be sufficiently small compared to the size of the computational domain (McWilliams, 1984) arranged in random positions. The velocity variable is normalized by the square root of the spatial average of the initial kinetic energy $u^*(t_0) \equiv [\overline{u^2(t_0)}]^{1/2}$, where the overline denotes the spatial average. The spatial length and time scales are non-dimensionalized by the initial integral length scale $l^*(t_0) \equiv [2\overline{u^2(t_0)}/\overline{\omega^2(t_0)}]^{1/2}$ and the initial eddy turnover time $t_0^* \equiv l^*(t_0)/u^*(t_0)$, respectively.

The Reynolds number is defined accordingly as $Re \equiv u^*l^*/\nu$ where ν is the kinematic viscosity. In this study, turbulent flows with initial Reynolds numbers of $Re(t_0) = 75$, 439, 814, 1607, and 2485 are selected.

8.1   Network-based characterization

We identify the underlying network structure and characteristics of two-dimensional turbulence based on the aforementioned symmetric adjacency weights. The time-evolving vorticity field is obtained from a two-dimensional incompressible bi-periodic direct numerical simulation (Canuto *et al.*, 1988) for unforced isotropic turbulence. Given the vorticity field over a Cartesian grid, each fluid element is considered to be connected to all other elements through vortical network edges. The resulting fluid flow network can in fact be described by a complete graph with a range of weights. Next, we visualize the network edges with transparent gray scale corresponding to the adjacency weight, as shown in Fig. 8.2(a). The captured structure reveals the turbulent network. Some regions in the flow have a large number of strong connections corresponding to larger stronger vortices seen in red, serving as primary network hubs. Note that these strong vortices induce velocities over long distances. Moderate size vortices that act as secondary hubs also possess dominant connections to primary hubs and other secondary hubs. In contrast, fluid elements corresponding to smaller, weaker eddies, shown in blue, generally have influence only in their vicinity. The node strength distribution ($s_i = \sum_j A_{ij}$) over space shows that the vortices with large circulation have larger strength, as illustrated in Fig. 8.2(b). The node strength distribution over space enables us to distinguish secondary and primary hubs, which may not be easily differentiated from simply visualizing the vorticity field or the Q criterion in a traditional manner. For instance, see the green vortices in (b) which can appear similar to primary ones in vorticity level.

Plotting the probability of strength distribution $P(s)$ over the strength s of fluid elements in Fig. 8.2(c), we find that two-dimensional isotropic turbulence network has a power-law distribution $P(s) \sim s^{-\gamma}$ with $\gamma = 2.7$ at the time shown. This tells us that the vortex interactions in turbulence can be characterized by a weighted scale-free network. This realization enables the interaction-based analysis of turbulent flows from a new perspective through network theory (Newman, 2010; Cohen & Havlin, 2010). In particular, this type of network is known to have certain resilience properties as we will explore later in this section. Also shown in Fig. 8.2(c) in gray are the degree distributions for asymmetric adjacency formulations. The out and in-degree distributions can be found by setting $\phi = 0$ and 1, respectively, in Eq. (8.1). It can be observed that the scale-free symmetric distribution is mostly comprised of the out-degree components, which describe how each vortical element influences all other elements (i.e., $u_{j \to i}$). In contrast, we find that the in-degree distribution has a single peak which conveys that all fluid elements receive a similar amount of collective influence from vortices in the flow field. We have found that the scale-free property of two-dimensional isotropic turbulence is most well-captured by the symmetric weights compared to the other asymmetric formulations. It is also possible to examine the strength distribution taking positive and negative values of circulations, as we have briefly discussed in Section 2. Uti-
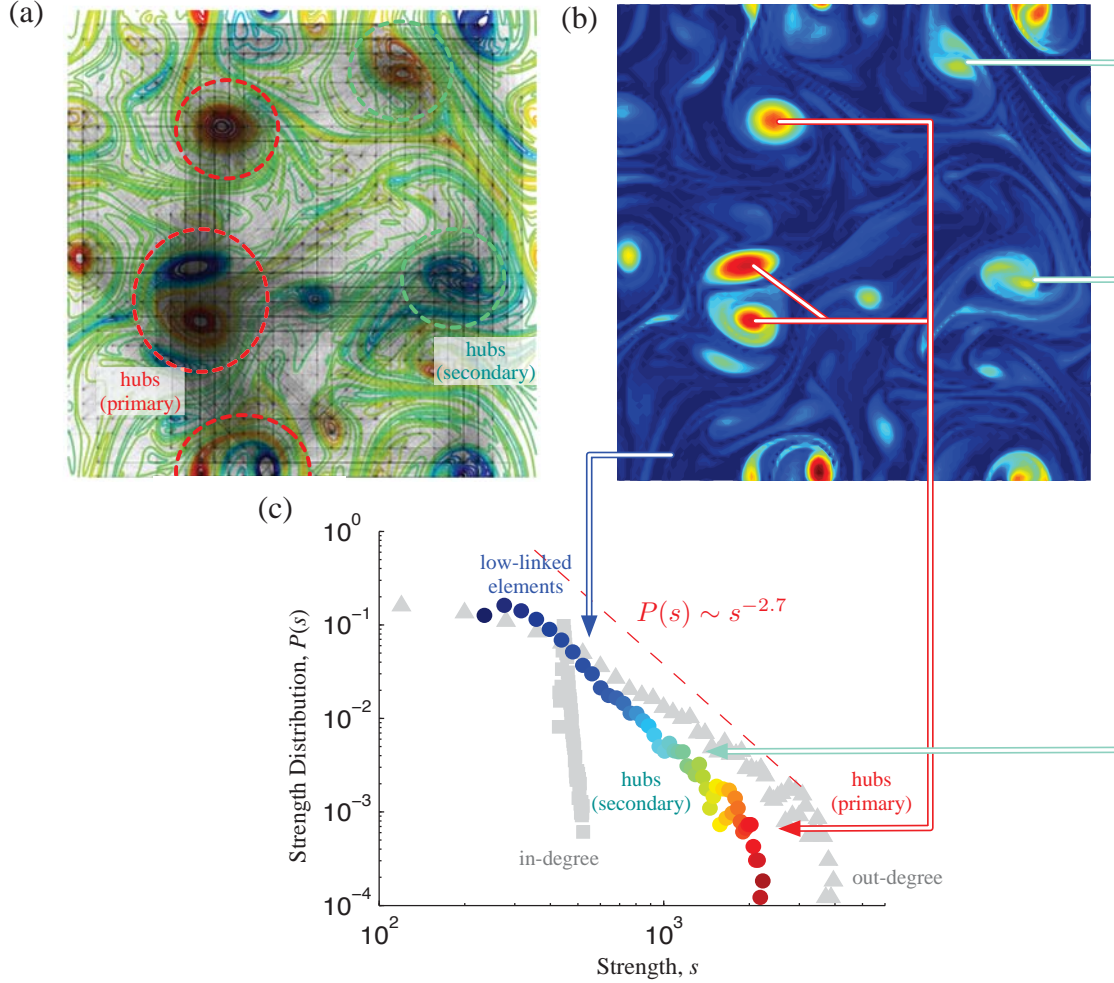
Figure 8.2: The scale-free network of vortical interactions in two-dimensional turbulence with initial $Re(t_0) = 814$. (a) Turbulent network structure overlaid on the vorticity field with the darkness of the network edges corresponding to the values of the adjacency weights ($t = 18$). (b) Contour plot of the node strength s distribution. Vortex cores having high degree of connectivity act as hubs in the turbulent vortical network. (c) The corresponding node strength probability distribution exhibiting the scale-free characteristics with $P \sim s^{-2.7}$. The same contour level is shared by (b) and (c). Also shown in the background of (c) in gray are the out and in-degree distributions ($\phi = 0$ and 1, respectivley). The network visualized in (a) does not show interactions from periodic images and uses 32×32 nodes for graphical clarity.

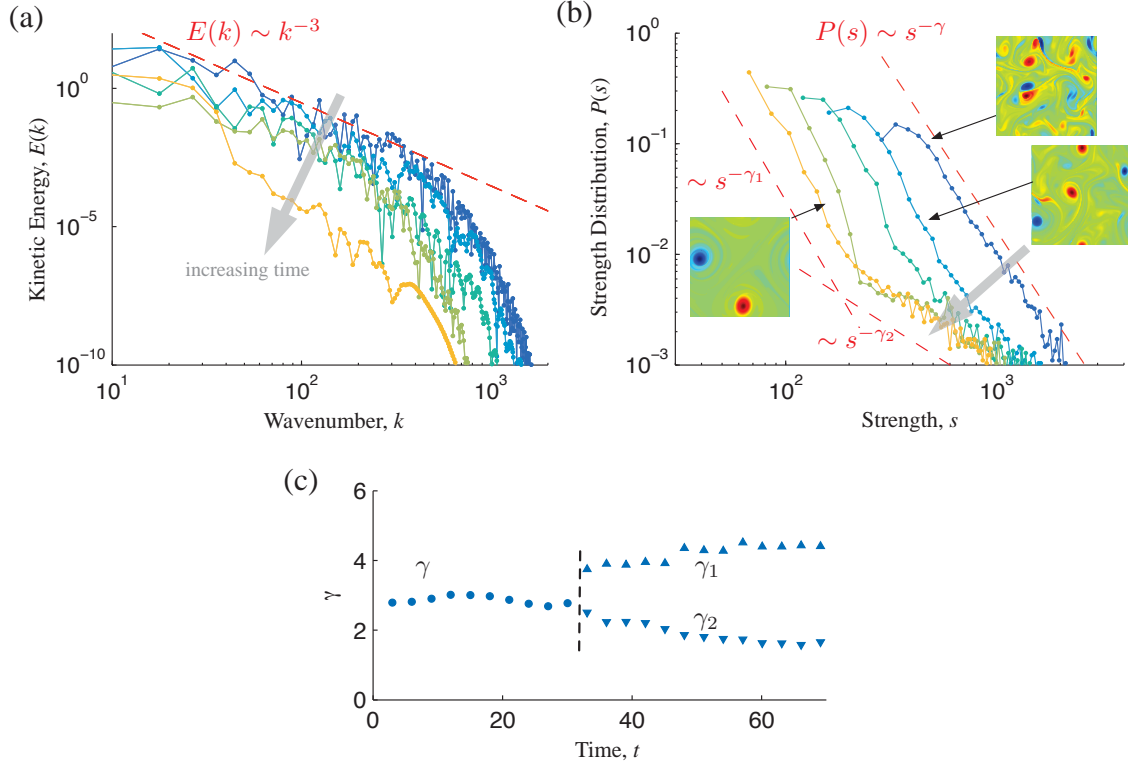Figure 8.3: The dynamics of turbulent network with $Re(t_0) = 814$. (a) Kinetic energy and (b) strength distribution of two-dimensional isotropic turbulence for $t = 15$, 30, 75, 150, and 300 (line colors represent time). The inset plots in (b) show the corresponding vorticity fields. The kinetic energy $E(k)$ is shown over the wavenumber k exhibiting the asymptotic profile of $E(k) \sim k^{-3}$. The strength distribution $P(s)$ displays the scale-free property of $P(s) \sim s^{-\gamma}$ over node strength s. (c) The corresponding exponents γ, γ_1, and γ_2 are shown. Later in time the strength distribution exhibits the emergence of two distributions, $P(s) \sim s^{-\gamma_1}$ and $s^{-\gamma_2}$.

lizing positive and negative weights, their strength distribution can also exhibit a scale-free behavior but with network strength having both negative and positive values. This leads to a symmetric strength distribution over the strength with resemblance to the probability density function of scaled displacements (Weiss *et al.*, 1998). In what follows, results based on the symmetric adjacency matrix (using the magnitude of induced velocity) are presented.

Let us further examine the time-varying properties of the turbulent network. In unforced turbulence, the kinetic energy of the flow decreases over time due to viscous dissipation as shown in Fig. 8.3(a). The strength distribution $P(s)$ of the turbulence network and the corresponding flow field snapshots are presented in Fig. 8.3(b). Turbulent flow is comprised of vortical structures over a wide range of spatial scales initially. The distribution $P(s)$ exhibits scale-free characteristics for $t \lesssim 30$ with $P(s) \sim s^{-\gamma}$, where $\gamma \approx 2.7$. For the flow
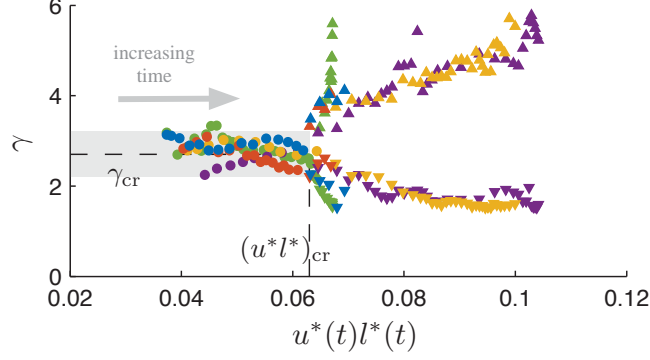
Figure 8.4: Exponent γ for the network strength distribution $P(s) \sim s^{-\gamma}$ plotted over $u^*(t)l^*(t)$ with different initial Reynolds numbers (green: $Re(t_0) = 75$, purple: $Re(t_0) = 439$, yellow: $Re(t_0) = 814$, red: $Re(t_0) = 1607$, and blue: $Re(t_0) = 2485$). Scale-free distributions are observed with γ coalescing to $\gamma_{cr} \approx 2.7$ up until a bifurcation at $(u^*l^*)_{cr} \approx 0.063$. The gray box shows $\gamma = -2.7 \pm 0.5$ as reference.

under consideration, a bend in the strength distribution appears after $t \approx 30$ as the system starts to exhibit scale separation. This is caused by the diffusion of smaller scale structures and their merging with other structures. Over time, viscous dissipation removes kinetic energy through the smaller eddies and leaves only the larger vortices. This behavior can be described by two power laws $P(s) \sim s^{-\gamma_1}$ and $P(s) \sim s^{-\gamma_2}$, where they capture the weaker fluid elements and the larger stronger vortices, respectively. The bifurcation of these power laws is shown in Fig. 8.3(c) indicated by the vertical dashed line.

We have considered a range of Reynolds numbers and observed that γ takes values of $\gamma = 2.7 \pm 0.5$. The variations observed in γ, γ_1, and γ_2 shown in Fig. 8.3(c) are influenced by the chaotic nature of turbulence. These parameters however appear to exhibit a coalescing behavior when they are plotted over the product of the characteristic velocity and length, $u^*(t)l^*(t)$. Here, we interpret $u^*(t)l^*(t)$ as the circulation of vortices that have the characteristic velocity and length scales. As shown in Figure 8.4, we observe that the turbulence network shows coalescence of the scale-free parameter γ to $\gamma_{cr} \approx 2.7$ over time for different cases of turbulent flows. Once the flows reach a state where the characteristic strength of vortices is $(u^*l^*)_{cr} \approx 0.063$, the network distribution bifurcates to display two different slopes with γ_1 and γ_2, as previously illustrated in Figure 8.3. This observation reveals that a scale-free turbulent network is present until the unforced turbulent flow field loses the smaller-scale vortices and mostly contains vortices with strengths larger than the critical value of $(u^*l^*)_{cr}$.

8.2   Resilience of turbulence networks

Characterizing turbulent flow with a scale-free network enables us to view turbulent interactions in a systematic manner and provides insights into how vortical structures influence each

other. It is known from network analysis that scale-free networks are resilient to random perturbations but attacks towards network hubs can affect network dynamics in a detrimental manner (Albert *et al.*, 2000). Network resilience for fluid flow translates to the difficulty of modifying the vortical interaction network and, consequently, the collective behavior of the vortices over time. To measure the change in vortical interaction caused by network disturbance, we can consider how the removal of turbulence network nodes (percolation) modifies the characteristic network length

$$l_{\text{network}} \equiv \frac{1}{n(n-1)} \sum_{i \neq j} \min d(i, j), \tag{8.3}$$

which is the average shortest network distance $d(i, j)$ between any two nodes on a network. Here, we perform node percolation by setting the vorticity values at the chosen nodes to be zero. The above metric quantifies how well vortical elements are connected within a turbulent network. Note that the distance here refers to network distance based on the adjacency matrix and not the spatial distance. In particular, we take the inverse of each adjacency weight $1/a_{ij}$ and evaluate the minimal sum

$$d(i, j) = 1/a_{ik_1} + 1/a_{k_1 k_2} + \cdots + 1/a_{k_m j} \tag{8.4}$$

over a network path that connects nodes i and j for this metric (Rubinov & Sporns, 2010). This metric l_{network} can be thought of as the average of the minimal characteristic advective (commute) time per unit length between every pair of fluid elements in the domain. This minimal network distance is determined using the Floyd–Warshall algorithm (Floyd, 1962).

The changes in the turbulence network characteristic length l_{network} when network nodes are removed in a random fashion and a coordinated manner targeting hub nodes are summarized in Fig. 8.5. Here, the changes in the normalized characteristic network length

$$\Delta \tilde{l}_{\text{network}} \equiv \frac{l_{\text{network}}(t, f) - l_{\text{network}}(t, f = 0)}{l_{\text{network}}(t, f = 0)} \tag{8.5}$$

for varied fraction of node removal are shown. While it would be difficult to completely remove nodes as we have performed in this investigation, the present analysis sheds light on how external forcing or perturbations can alter the turbulent flow from an interaction-based analysis. We observe that turbulent flow is resilient against random forcing, as evident from the characteristic network length being unaffected even for a large fraction f of nodes being removed. This behavior is consistently observed over time. On the other hand, we find that the global vortical interaction network can be greatly modified by targeting large vortex cores (hubs), as exhibited by the substantial change in the characteristic length. It may be more energetically expensive to remove well-connected hub nodes, which often correspond to regions of concentrated vorticity. However, it is clear from Figure 8.5 that even the smallest fraction of hub node removal can influence the overall interaction, which suggests that hub removal still provides a more effective and efficient way to modify the flow than random node removal.
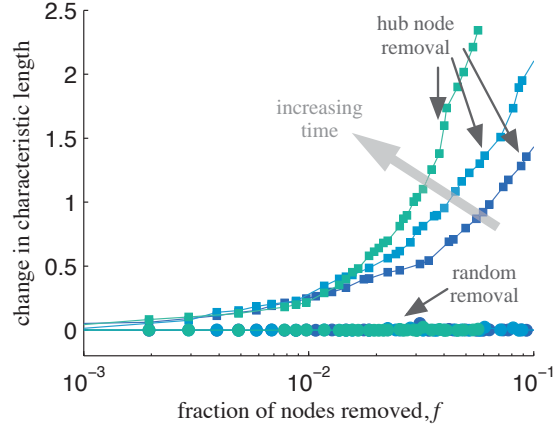
Figure 8.5: The resilience of turbulence network against node removals for $t = 15$, 30, and 75 with $Re(t_0) = 814$. Shown are relative changes in the characteristic network length $\Delta \tilde{l}_{\mathrm{network}}$ of turbulent flow for random node and hub node removals. The colors of the curves represent the time when node removal is considered and follows Figure 8.3.

When the vortical interaction network is grossly altered, the dynamics of the collection of vortices would be significantly modified (Nair & Taira, 2015). These observations also agree with past studies in flow control that identified effective actuation frequencies to be associated with the length scale of the large coherent structures in turbulent flows (Joslin & Miller, 2009; Gad-el-Hak, 2000b). With increasing time, we can further notice that network connectivity decreases with hub removal due to viscous dissipation of smaller vortical structures and the influence of removing the core structures becomes more evident. The present network based understanding reveals which type of flow structures should be targeted with flow control if we aim to alter the behavior of the turbulent flow field in a global manner.

Chapter 9

Concluding Remarks

Perturbations of wall-normal momentum and wall-normal vorticity are injected into the boundary layer to modify the separated flow over a NACA 0012 airfoil at $Re = 23,000$ and at a high angle of attack. We considered a massively separated baseline flow with a separation region which extends from the leading edge to the trailing edge. Eliminating the large separation using actuation led to increased lift and decreased drag. In this study the control inputs were independently prescribed by a model boundary condition near the natural separation point. By examining the controlled flow field and resulting forces, we quantified the necessary control inputs to the alter the aerodynamic forces. In doing so, we establish a need for not only a coefficient of momentum but also a coefficient of circulation to account for the angular momentum added to the boundary layer by streamwise vortices. The so-called coefficient of circulation is a function of wall-normal and azimuthal velocity, accounting for the vorticity flux into boundary layer.

Using the coefficients individually did not result in an obvious trend that would allow general input arguments to quantify the resulting forces. Therefore, a linear relationship is created between the momentum directly added to the flow (C_μ) and that added through mixing the free stream and boundary layer (C_Γ). Using the total coefficient ($C_\mu + C_\Gamma$) identifies three regions: separated flow, transition, and attached flow. Initially, for small values of control input lift decreases due to the perturbation added to the boundary layer, but remains consistent for a range of values of $C_{\text{total}} \lesssim 0.4$. For these smaller inputs the size of the separation region remains similar to the baseline case. A sharp increase in lift forces is observed when the reverse flow region begins to diminish. Reaching a certain value for the control input, in this study $C_{\text{total}} \gtrsim 0.65\%$, flow is reattached, leading to improvements in the aerodynamic forces. Realizing the total coefficient value necessary to reattach the flow allows implementation of any actuator with C_{total} greater than some critical value, which was $C_{\text{total}} \gtrsim 0.65\%$ for $\alpha = 9°$. For example, we successfully identified the value of wall-normal velocity (C_μ) that would reattach the flow at $\alpha = 9°$ based on the total coefficient.

Moreover, the study has developed advanced analysis techniques. First, the capability to perform bi-global stability analysis has been developed and validated, which can serve as a basis for physics-based active flow control guided by the knowledge of hydrodynamic instabilities. Second, as part of modeling complex unsteady flows in general, efforts in

this study has led to the initial development of a novel approach in quantifying nonlinear interactions present in vortical flows.

Graph representations of a system of discrete point vortices provide us with a framework for identifying important connections amongst vortices. The edge weights of the graph were related to the importance of the ties between the vortices, which were quantified based on the strength of the vortices and the relative distance between them. We sparsify the connections between these vortices based on spectral graph theory not only to cut some of these ties but also to redistribute their weights to preserve the dynamics of the vortices. We have demonstrated that an effective resistance approach to graph sparsification proves extremely useful in constructing sparsified-dynamics models. Moreover, sparsification reduces the number of connections to $\mathcal{O}(N \log N/\epsilon^2)$ based on approximation order ϵ. We also observe an increase in the effectiveness of sparsification with increasing number of point vortices. In spite of the nonlinear nature of the dynamics of these point vortices, the sparse representations are capable of identifying the core vortex structures as well as tracking the bulk motion of these structures in an effective manner. We have referred to the dynamical model that uses the sparsified vortex network as the sparsified-dynamics model. In addition, the sparsified models preserve spectral properties of the original setup. Resparsification is utilized to enhance the prediction of the motion of the vortices over time. We observe that sparsification conserves the invariants of discrete vortices dynamics such as the Hamiltonian, linear and angular impulse, and circulation. The objectives of sparsified-dynamics model are aligned with those of reduced-order models but these goals are achieved by sparsifying the connections rather than deriving a model equation with state variable of reduced dimension. The results of graph-theoretic approach to discrete vortex dynamics point to promising research in its applicability to a variety of problems in fluid mechanics.

Also, we have identified that the vortical interactions in two-dimensional isotropic turbulence have a scale-free network structure (Taira *et al.*, 2016). We have been able to reveal the structure by taking a continuous representation of the flow field and quantifying the network using a Cartesian discretization. For two-dimensional isotropic turbulence, the node strength distribution was uncovered to be $P(s) \sim s^{-\gamma}$, where $\gamma = 2.7 \pm 0.5$. Furthermore, we have found that the unforced turbulent flow field possesses an underlying scale-free network structure until the circulation of vortices with characteristic velocity and length scales reach $(u^*l^*)_{\mathrm{cr}} \approx 0.063$. By noticing that the turbulence network has scale-free characteristics, we were able to systematically show that the turbulence network is resilient against random perturbations but vulnerable against coordinated forcing on the hub vortices. It should be noted that estimating and controlling each and every vortical structure in a turbulent flow is most likely improbable and impractical. Instead, network analysis may provide a refreshing view point on how one can predict and modify the collective dynamics of vortices in the turbulent flow fields. We believe that the network-based analysis and control (Mesbahi & Egerstedt, 2010; Liu *et al.*, 2011; Cornelius *et al.*, 2013; Kaiser *et al.*, 2014*b*; Yan *et al.*, 2015) will provide novel mathematical fabric for paving the path towards network-based modeling and control of turbulent flows, which can potentially impact a wide spectrum of problems.

Acknowledgments

Appendix A

Control Input

A.1 $\alpha = 6°$

The velocities used to control the flow at $\alpha = 6°$ and resulting total coefficient. The accompanying lift and drag coefficients are listed as well.

α	Case	$u_{n,max}/U_\infty$	$u_{\theta,max}/U_\infty$	$C_{\text{total}}[\%]$	Rot. dir.	C_D	C_L
6°	Baseline	–	–	–	–	0.061	0.612
	6A	0	1.26	0.010	CTR	0.056	0.643
		0	5.05	0.040	CTR	0.043	0.623
	6B	0.32	0	0.082	–	0.047	0.614
		0.32	1.26	0.325	ROT	0.043	0.608
	6C	0.32	1.26	0.325	CTR	0.047	0.615
		0.63	0	0.272	–	0.050	0.595
		0.63	1.26	0.658	ROT	0.043	0.609
		0.63	1.26	0.658	CTR	0.049	0.600
		1.26	0	0.911	–	0.047	0.540
		1.26	1.26	1.524	ROT	0.055	0.534
		1.26	1.26	1.524	CTR	0.048	0.533

Table A.1: All of the control parameters used to control for flow over a NACA0012 airfoil at $\alpha = 6°$. The specific cases used as examples are denoted.

A.2 $\alpha = 9°$

The velocities used to control the flow at $\alpha = 9°$ and resulting total coefficient. The accompanying lift and drag coefficients are listed as well. Each table contains different data. Table A.2 contains the majority of cases run, and Table A.3 contains the result from modifying the spanwise spacing of the actuator.

α	Case	$u_{n,max}/U_\infty$	$u_{\theta,max}/U_\infty$	$C_{\text{total}}[\%]$	Rot. dir.	C_D	C_L
9°	Baseline	–	–	–	–	0.118	0.584
		0	5.04	0.027	CTR	0.118	0.552
		0.631	0	0.272	–	0.108	0.416
		0.631	1.26	0.657	CTR	0.120	0.411
		0.631	1.26	0.657	ROT	0.112	0.414
		0.789	0.95	0.736	CTR	0.108	0.429
		0.789	1.26	0.848	CTR	0.078	0.679
		0.789	2.52	1.294	CTR	0.097	0.609
		0.946	0	0.551	–	0.118	0.467
		0.946	0.946	0.930	CTR	0.101	0.463
		0.946	1.26	1.056	ROT	0.065	0.716
	9E	0.946	1.26	1.056	CTR	0.064	0.726
		0.946	2.52	1.561	CTR	0.092	0.628
	9A	1.26	0	0.911	–	0.108	0.403
		1.26	0.631	1.217	ROT	0.099	0.493
		1.26	0.631	1.217	CTR	0.096	0.510
	9B	1.26	0.95	1.370	CTR	0.094	0.483
	9C	1.26	1.26	1.523	ROT	0.069	0.665
		1.26	1.26	1.523	CTR	0.067	0.699
		1.26	2.523	2.134	CTR	0.069	0.725
		1.545	0	1.747	–	0.106	0.391
	9F	1.829	0	1.298	–	0.084	0.673

Table A.2: Control inputs for flow over a NACA0012 airfoil at $\alpha = 9°$, $l_z/c = 0.1$, and $\xi/c = 0.1$. The specific cases used as examples are denoted.

l_z/c	Case	$u_{n,max}/U_\infty$	$u_{\theta,max}/U_\infty$	$C_{\text{total}}[\%]$	Rot. dir.	C_D	C_L
0.2		0.892	0	0.249	–	0.112	0.457
0.2		0.892	0.892	0.420	ROT	0.113	0.451
0.2		0.892	1.784	0.592	ROT	0.103	0.376
0.2		1.34	0	0.505	–	0.114	0.464
0.2		1.34	0.892	0.730	ROT	0.111	0.411
0.2		1.34	1.784	0.955	ROT	0.064	0.731
0.2	9F	1.784	0	0.836	–	0.075	0.724
0.2		1.784	1.784	1.382	ROT	0.082	0.687
0.067		1.029	0	0.956	–	0.100	0.454
0.067		1.029	1.023	1.609	ROT	0.101	0.444
0.05		0.981	0	0.992	–	0.096	0.494
0.05		0.891	0.891	1.677	ROT	0.105	0.378

Table A.3: Control inputs for flow over a NACA0012 airfoil at $\alpha = 9°$, $l_z/c \neq 0.1$, and $\xi/c = 0.1$. The specific cases used as examples are denoted.

Bibliography

ABE, Y., OKADA, K., SATO, M., NONOMURA, T. & FUJII, K. 2013 Significance of three-dimensional unsteady flows inside of the cavity on separated-flow control around an NACA 0015 using a synthetic jet. *AIAA 2013-2748* .

AHUJA, S. & ROWLEY, C. W. 2010 Feedback control of unstable steady states of flow past a flat plate using reduced-order estimators. *J. Fluid Mech.* **645**, 447–478.

ÅKERVIK, E., BRANDT, L., HENNINGSON, D. S., JÉRÔME, H., MARXEN, O. & SCHLATTER, P. 2006 Steady solutions of the navier-stokes equations by selective frequency damping. *Physics of Fluids* **18**.

ALBERT, R., JEONG, H. & BARABÁSI, A.-L. 2000 Error and attack tolerance of complex networks. *Nature* **406**, 378–382.

ASHILL, P. R., FULKER, J. L. & HACKETT, K. C. 2002 Studies of flows induced by sub boundary layer vortex generators. *AIAA Paper 2002-0968* .

BAGHERI, S., HŒPFFNER, J., SCHMID, P. & HENNINGSON, D. 2009 Input-output analysis and control design applied to a linear model of spatially developing flows. *Applied Mechanics Reviews* **62** (2).

BARABÁSI, A.-L. & ALBERT, R. 1999 Emergence of scaling in random networks. *Science* **286**, 509–512.

BARRAT, A., BARTHÉLEMY, M. & VESPIGNANI, A. 2004 Weighted evolving networks: coupling topology and weighted dynamics. *Phys. Rev. Let.* **92** (22), 228701.

BARRETT, R., BERRY, M., CHAN, T., DEMMEL, J., DONATO, J., DONGARRA, V. E., POZO, R., ROMAINE, C. & VANDENHORST, H. 1993 Templates for the solutions of linear systems: Building blocks for iterative methods. In *Philidelphia*. SIAM.

BATCHELOR, G. 2000 *An introduction to fluid dynamics*. Cambridge university press.

BENCZÚR, A. & KARGER, D. R. 1996 Approximating $s - t$ minimum cuts in $\mathcal{O}(n^2)$ time. In *Proceedings of the twenty-eighth annual ACM symposium on Theory of computing*, pp. 47–55. ACM.

BENZI, R. & COLELLA, M. 1992 A simple point vortex model for two-dimensional decaying turbulence. *Phys. Fluids A* **4** (5), 1036–1039.

BENZI, R., PALADIN, G. & VULPIANI, A. 1990 Power spectra in two-dimensional turbulence. *Phys. Rev. A* **42** (6), 3654–3656.

BERKOOZ, G., HOLMES, P. & LUMLEY, J. 1993 The proper orthogonal decomposition in the analysis of turbulent flows. *Annual review of fluid mechanics* **25** (1), 539–575.

BOFFETTA, G. & ECKE, R. E. 2012 Two-dimensional turbulence. *Annu. Rev. Fluid Mech.* **44**, 427–451.

BOLLOBÁS, B. 1998 *Modern graph theory*. Springer.

BREHM, C. & FASEL, H. F. 2011 An initial value problem approach to investigate biglobal stability problems. AIAA.

BRUNTON, S. L. & NOACK, B. R. 2015 Closed-loop turbulence control: progress and challenges. *App. Mech. Rev.* **67** (5), 050801.

CALDARELLI, G. 2007 *Scale-free networks*. Oxford Univ. Press.

CANUTO, C., HUSSAINI, M. Y., QUARTERONI, A. & ZANG, T. A. 1988 *Spectral methods in fluid dynamics*. Springer-Verlag, New York.

CATTAFESTA, L., SONG, Q., WILLIAMS, D., ROWLEY, C. & ALVI, F. 2008 Active control of flow-induced cavity oscillations. *Progress In Aerospace Sciences* **44**, 479–502.

CATTAFESTA, L. N. & SHEPLAK, M. 2011 Actuators for active flow control. *Annu. Rev. Fluid Mech.* **43**, 247–272.

CAUCHEMEZA, S., A, B., MARCHBANKS, T. L., FAGAN, R. P., S. OSTROFF, N. M. F., SWERDLOW, D. & WORKING GROUP, P. H. 2011 Role of social networks in shaping disease transmission during a community outbreak of 2009 H1N1 pandemic influenza. *Proceedings of the National Academy of Sciences* **108** (7), 2825–2830.

CHANG, P. K. 1976 *Control of Flow Separation*. Hemisphere Publishingn Corporation.

CHEN, W. K. 2004 *The Electrical Engineering Handbook*. Elsevier Science.

CHOI, H., MOIN, P. & KIM, J. 1993 Direct numerical simulation of turbulent flow over riblets. *Journal of Fluid Mechanics* **255**, 503–539.

COHEN, R. & HAVLIN, S. 2010 *Complex Networks: Structure, Robustness and Function*. Cambridge Univ. Press.

COMPTON, D. A. & JOHNSTON, J. P. 1992 Streamwise vortex production by pitched and skewed jets in a turbulent boundary layer. *AIAA Journal* **30**, 640–647.

Corke, T. C., Enloe, C. L. & Wilkinson, S. P. 2010 Dielectric barrier discharge plasma actuators for flow control. *Annual Review of Fluid Mechanics* **42**, 505–529.

Cornelius, S. P., Kath, W. K. & Motter, A. E. 2013 Realistic control of network dynamics. *Nature Comm.* .

Cottet, G.-H. & Koumoutsakos, P. D. 2000 *Vortex methods: theory and practice*. Cambridge Univ. Press.

Davidson, P. A. 2004 *Turbulence: an introduction for scientists and engineers*. Oxford University Press.

Deng, S., Jiang, L. & Liu, C. 2007 DNS for flow separation control around an airfoil by pulsed jets. *Computers and Fluids* **36** (6), 1040–1060.

Dorogovtsev, S. N. 2010 *Lectures on Complex Networks*. Oxford Univ. Press.

Duarte-Cavajalino, J. M., Jahanshad, N., Lenglet, C., McMahon, K. L., de Zubicaray, G. I., Martin, N. G., Wright, M. J., Thompson, P. M. & Sapiro, G. 2012 Hierarchical topological network analysis of anatomical human brain connectivity and differences related to sex and kinship. *NeuroImage* **59**, 3784–3804.

Ellens, W., Spieksma, F., Van Mieghem, P., Jamakovic, A. & Kooij, R. 2011 Effective graph resistance. *Linear algebra and its applications* **435** (10), 2491–2506.

Farazmand, M. M., Kevlahan, N. K.-R. & Protas, B. 2011 Controlling the dual cascade of two-dimensional turbulence. *J. Fluid Mech.* **668**, 202–222.

Floyd, R. W. 1962 Algorithm 97: Shortest path. *Comm. ACM* **5** (6), 345.

Frisch, U. 1995 *Turbulence*. Cambridge Univ. Press.

Gad-el-Hak, M. 2000a *Flow control: passive, active, and reactive flow management*. Cambridge Univ. Press, London.

Gad-el-Hak, M. 2000b *Flow control: passive, active, and reactive flow management*. Cambridge Univ. Press.

Gilarranz, J. L., Traub, L. W. & Redinoitis, O. K. 2005 A new class of synthetic jet actuators–Part II: application to flow separation control. *Journal of Fluids Engineering* **127**.

Glass, R. J., Glass, L. M., Beyeler, W. E. & Min, H. J. 2006 Targeted social distancing design for pandemic influenza. *Emerg. Infect. Diseases* **12** (11), 1671–1681.

Glezer, A. & Amitay, M. 2002 Synthetic jets. *Annu. Rev. Fluid Mech.* **34**, 503–529.

GREENBLATT, D., WYGNANSKI, I. J. & RUMSEY, C. L. 2015 Aerodynamic flow control. *Encyclopedia of Aerospace Engineering* .

GREENGARD, L. & ROKHLIN, V. 1987 A fast algorithm for particle summations. *J. Comput. Phys.* **73**, 325–348.

HAM, F. & IACCARINO, G. 2004 Energy conservation in collocated discretization schemes on unstructured meshes. Annual research brief. Center for Turbulence Research, Stanford University.

HAM, F., MATTSON, K. & IACCARINO, G. 2006 Accurate and stable finite volume operators for unstructured flow solvers. *Tech. Rep.*. Center for Turbulence Research.

HEMATI, M., ELDREDGE, J. D. & SPEYER, J. L. 2014 Improving vortex models via optimal control theory. *Journal of Fluids and Structures* .

HINZE, J. O. 1975 *Turbulence*. McGraw-Hill, New York.

HOLMES, P., LUMLEY, J. L. & BERKOOZ, G. 1996 *Turbulence, coherent structures, dynamical systems and symmetry*. Cambridge Univ. Press.

HORNUNG, H. 1989 Vorticity generation and transport. In *Tenth Australasian Fluid Mechanics Conference - University of Melbourne*.

HUANG, L., HUANG, P. G. & LEBEAU, R. P. 2004 Numerical study of blowing and suction control mechanism on NACA 0012 airfoil. *Journal of Aircraft* **41** (1).

JOSLIN, R. D. & MILLER, D. (ed.) 2009 *Fundamentals and applications of modern flow control*. AIAA.

KAISER, E., NOACK, B. R., CORDIER, L., SPOHN, A., SEGOND, M., ABEL, M., DAVILLER, G. & NIVEN, R. K. 2014*a* Cluster-based reduced-order modelling of a mixing layer. *Journal of Fluid Mechanics* **754**, 365–414.

KAISER, E., NOACK, B. R., CORDIER, L., SPOHN, A., SEGOND, M., ABEL, M., DAVILLER, G., OSTH, J., KRAJNOVIĆ, S. & NIVEN, R. K. 2014*b* Cluster-based reduced-order modelling of a mixing layer. *J. Fluid Mech.* **754**, 365–414.

KELNER, J. & LEVIN, A. 2011 Spectral sparsification in the semi-streaming setting. *Leibniz International Proceedings in Informatics (LIPIcs) series* **9**, 440–451.

KERHO, M., HUTCHERSON, S., BLACKWELDER, R. F. & H., L. R. 1993 Vortex generators used to control laminar separation bubbles. *Journal of Aircraft* **30** (3), 315–319.

KITSIOS, V., RODRÍGUEZ, D., THEOFILIS, V., OOI, A. & SORIA, J. 2009 Biglobal stability analysis in curvilinear coordinates of massively separted lifting bodies. *Journal of Computational Physics* **228**, 7181–7196.

KLEIN, D. J. & RANDIĆ, M. 1993 Resistance distance. *Journal of Mathematical Chemistry* **12** (1), 81–95.

KOJIMA, R., NONOMURA, T., OYAMA, A. & FUJII, K. 2013 Large-eddy simulation of low-Reynolds-number flow over thick and thin NACA airfoils. *Journal of Aircraft* **50** (1), 187–196.

KOTAPATI, R. B., MITTAL, R., MARXEN, O., HAM, F., YOU, D. & CATTAFESTA, L. N. 2010 Nonlinear dynamics and synthetic-jet-based control of a canonical separated flow. *J. Fluid Mech.* **654**, 65–97.

KRAICHNAN, R. H. & MONTGOMERY, D. 1980 Two-dimensional turbulence. *Rep. Prog. Phys.* **43**, 547–619.

LACHMANN, G. V. 1961 *Boundary layer and flow control. Its principles and applications. vol 1 & 2*. Pergamon Press.

LEHOUCQ, R. B., SORENSEN, D. C. & YANG, C. 1998 Arpack users guide: Solution of large-scale eigenvalue problems with implicitly restarted arnoldi methods. SIAM.

LEONARD, A. 1980 Vortex methods for flow simulation. *Journal of Computational Physics* **37** (3), 289–335.

LESIEUR, M. 2008 *Turbulence in fluids*, 4th edn. Springer.

LIN, J. C. 2002 Review of research on low-profile vortex generators to control boundary-layer separation. *Progress in Aerospace Science* **38**, 389–420.

LIN, J. C., ROBINSON, S. K., MCGHEE, R. J. & VALAREZO, W. O. 1994 Separation control on hihg-lift airfoil via micro-vortex generators. *Journal of Aircraft* **31** (6).

LITTLE, J., NISHIHARA, M., ADAMOVICH, I. & SAMIMY, M. 2010 High-lift airfoil trailing edge separation control using a single dielectric barrier discharge plasma actuator. *Experiments in Fluids* **48**, 521–537.

LIU, Y.-Y., SLOTINE, J.-J. & BARABÁSI, A.-L. 2011 Controllability of complex networks. *Nature* **473** (7346), 167–173.

LLOYD-SMITH, J., SCHREIBER, S., KOPP, P. & GETZ, W. 2005 Superspreading and the effect of individual variation on disease emergence. *Nature* **438**, 355–359.

MA, Z., AHUJA, S. & ROWLEY, C. W. 2009 Reduced order models for control of fluids using the eigensystem realization algorithm. *Theo. Comp. Fluid Dyn.* **25** (1), 233–247.

MCWILLIAMS, J. C. 1984 The emergence of isolated coherent vortices in turbulent flow. *J. Fluid Mech.* **146**, 21–43.

MESBAHI, M. & EGERSTEDT, M. 2010 *Graph theoretic methods in multiagent networks*. Princeton Univ. Press.

MIEGHEM, P. V. 2011 *Graph spectra for complex networks*. Cambridge University Press.

MOHAR, B. 1991 The Laplacian spectrum of graphs. In *Graph theory, combinatorics, and applications* (ed. Y. Alavi, G. Chartrand, O. Ollermann & A. Schwenk), pp. 871–898. Wiley, New York.

MORINISHI, Y., LUND, T. S., VASILYEV, O. V. & MOIN, P. 1998 Fully conservative high order finite difference schemes for incompressible flow. *Journal of Computational Physics* **143**, 90–124.

MORRIS, M. 1993 Epidemiology and social networks - modeling structured diffusion. *Sociol. Method Res.* **22**, 99–126.

MUNDAY, P. M. & TAIRA, K. 2014 Separation control on NACA 0012 airfoil using momentum and wall-normal vorticity injection. *AIAA 2014-2685* .

MUNDAY, P. M. & TAIRA, K. 2015 Surface vorticity flux analysis in separation control on NACA 0012 airfoil. *AIAA 2015-2632* .

MUPPIDI, S. & MAHESH, K. 2005 Study of trajectories of jets in crossflow using direct numerical simulations. *Journal of Fluid Mechanics* **530**, 81–100.

NAIR, A. G. & TAIRA, K. 2015 Network-theoretic approach to sparsified discrete vortex dynamics. *J. Fluid Mech.* **768**, 549–571.

NATARAJAN, R. & ACRIVOS, A. 1993 The instability of the steady flow past spheres and disks. *Journal of Fluid Mechanics* **254**, 323–344.

NEWMAN, M. E. J. 2004 Fast algorithm for detecting community structure in networks. *Physical review E* **69**, 066133.

NEWMAN, M. E. J. 2010 *Networks: an introduction*. Oxford Univ. Press.

NEWTON, P. K. 2001 *The N-vortex problem: analytical techniques*, *Applied Mathematical Sciences*, vol. 145. Springer.

NOACK, B. R. & ECKELMANN, H. 1994 A global stability analysis of the steady and periodic cylinder wake. *Journal of Fluid Mechanics* **270**, 297–330.

NOACK, B. R., PAPAS, P. & MONKEWITZ, P. A. 2005 The need for a pressure-term representation in empirical Galerkin models of incompressible shear flows. *J. Fluid Mech.* **523**, 339–365.

Owen, J. P., Li, Y.-O., Ziv, E., Strominger, Z., Gold, J., Bukhpun, P., Wakahiro, M., Friedman, E. J., Sherr, E. H. & Mukherjee, P. 2013 The structural connectome of the human brain in agenesis of the corpus callosum. *NeuroImage* **70**, 340–355.

Pedro, H. T. C. & Kobayashi, M. H. 2008 Numerical study of stall delay on humpback whale flippers. AIAA Paper 2008-0584.

Peleg, D. & Ullman, J. 1989 An optimal synchronizer for the hypercube. *SIAM Journal on computing* **18** (4), 740–747.

Pope, S. B. 2000 *Turbulent flows*. Cambridge Univ. Press.

Porter, M. A., Mucha, P. J., Newman, M. E. J. & Warmbrand, C. M. 2005 A network analysis of committees in the U.S. House of Representatives. *Proc. Nat. Acad. Sci.* **102** (20), 7057–7062.

Raju, R., Aram, E., Mittal, R. & Cattafesta, L. 2009 Simple models of zero-net mass-flux jets for flow control simulations. *International Journal of Flow Control* **1** (3), 179–197.

Rathay, N., Boucher, M., Amitay, M. & Whalen, E. 2014a Parametric study of synthetic-jet-based control for performance enhancement of a vertical tail. *AIAA Journal* **52** (11), 2440–2454.

Rathay, N., Boucher, M., Amitay, M. & Whalen, E. 2014b Performance enhancement of a vertical tail using synthetic jet actuators. *AIAA Journal* **52** (4).

Robinson, K., Cohen, T. & Colijn, C. 2012 The dynamics of sexual contact networks: effects on disease spread and control. *Theo. Popul. Bio.* **81**, 89–96.

Rodríguez, D. 2010 *Global Instability of Laminar Separation Bubbles*. PhD Thesis, Universidad Politécnica De Madrid.

Rowley, C., Colonius, T. & Murray, R. 2004 Model reduction for compressible flows using POD and Galerkin projection. *Physica D: Nonlinear Phenomena* **189** (1), 115–129.

Rowley, C. W. 2005 Model reduction for fluids, using balanced proper orthogonal decomposition. *Int. J. Bif. Chaos* **15** (3), 997–1013.

Rowley, C. W., Mezić, I., Bagheri, S. & Henningson, D. S. 2009 Spectral analysis of nonlinear flows. *J. Fluid Mech.* **641**, 115–127.

Rubinov, M. & Sporns, O. 2010 Complex network measures of brain connectivity: Uses and interpretations. *NeuroImage* **52**, 1059–1069.

Saffman, P. G. 1992 *Vortex dynamics*. Cambridge Univ. Press.

SALATHÉ, M. & JONES, J. H. 2010 Dynamics and control of diseases in networks with community structure. *PLoS Comput. Bio.* **6** (4), e1000736.

SATO, M., AONO, H., YAKENO, A., NONOMURA, T., FUJII, K., OKADA, K. & ASADA, K. 2015 Multifactorial effects of operating conditions of dielectric-barrier-discharge plasma actuator on laminar-separated-flow control. *AIAA Journal* **53** (9).

SCHMID, P. J. 2007 Nonmodal stability theory. *Annu. Rev. Fluid Mech.* **39**, 129–162.

SCHMID, P. J. 2010 Dynamic mode decomposition of numerical and experimental data. *Journal of Fluid Mechanics* **656**, 5–28.

SEELE, R., GRAFF, E., GHARIB, M., TAUBERT, L., LIN, J. & WYGNANSKI, I. 2012 Improving rudder effectiveness with sweeping jet actuators. *AIAA paper* **3244**.

SEELE, R., GRAFF, E., LIN, J. & WYGNANSKI, I. 2013 Performance enhancement of a vertical tail model with sweeping jet actuators. *AIAA Paper* **411**, 2013.

SEIFERT, A. & PACK, L. T. 1999 Oscillatory excitation of unsteady compressible flows over airfoils at flight reynolds numbers. *AIAA 10.2514/6.1999-925* .

SELBY, G. V., LIN, J. C. & HOWARD, F. G. 1992 Control of low-speed turbulent separated flow using jet vortex generators. *Experiments in Fluids* **12**, 394–400.

SHAN, H., JIANG, L., CHAOQUN, L., LOVE, M. & MAINES, B. 2008 Numerical study of passive and active flow separation control over a NACA 0012 airfoil. *Computers and Fluids* pp. 975–992.

SKILLEN, A., REVELL, A., PINELLI, A., PIOMELLI, U. & FAVIER, J. 2015 Flow over a wing with leading-edge undulations. *AIAA Journal* **53** (2), 464–472.

SPIELMAN, D. A. & SRIVASTAVA, N. 2011 Graph sparsification by effective resistances. *SIAM J. Comput.* **40** (6), 1913–1926.

SPIELMAN, D. A. & TENG, S.-H. 2011 Spectral sparsification of graphs. *SIAM J. Comput.* **40** (4), 981–1025.

SRIVASTAVA, N. 2010 *Spectral sparsification and restricted invertibility*. PhD Thesis, Yale University.

TAIRA, K., NAIR, A. G. & BRUNTON, S. L. 2016 Network structure of two-dimensional decaying isotropic turbulence. *J. Fluid Mech.* **795**, R2.

TAYLOR, G. I. 1918 On the dissipation of eddies. Reports and Memoranda 598. Aero. Res. Comm.

TENNEKES, H. & LUMLEY, J. L. 1972 *A first course in turbulence*. MIT Press, Cambridge.

Theofilis, V. 2003 Advances in global linear instability analysis of nonparallel and three-dimensional flows. *Progress In Aerospace Sciences* **39**, 249–315.

Theofilis, V. 2011 Global linear instability. *Annual Review of Fluid Mechanics* **43**, 319–352.

Theofilis, V., Duck, P. W. & Owen, J. 2004 Viscous linear stability analysis of rectangular duct and cavity flows. *Journal of Fluid Mechanics* **505**, 249–286.

Vreman, A. W. 2004 An eddy-viscocity subgrid-scale model for turbulent shear flow: Algebraic theory and applications. *Physics of Fluids* **16** (10).

Wang, C. & Eldredge, J. 2013 Low-order phenomenological modeling of leading-edge vortex formation. *Theoretical and Computational Fluid Dynamics* **27** (5), 577–598.

Weiss, J. B., Provenzale, A. & McWilliams, J. C. 1998 Lagrangian dynamics in high-dimensional point-vortex systems. *Phys. Fluids* **10** (8), 1929–1941.

Whalen, E. A., Lacy, D. S., Lin, J. C., Andino, M. Y., Washburn, A. E., Graff, E. C. & Wygnanski, I. J. 2015 Performance enhancement of a full-scale vertical tail model equipped with active flow control. In *53rd AIAA Aerospace Sciences Meeting*, pp. 1–11.

Wu, J.-Z., Lu, X.-Y., Denny, A. D., Fan, M. & Wu, J.-M. 1998 Post-stall flow control on an airfoil by local unsteady forcing. *J. Fluid Mech.* **371**, 21–58.

Wu, J.-Z., Ma, H.-Y. & Zhou, M.-D. 2006 *Vorticity and vortex dynamics*. Springer-Verlag.

Yan, G., Tsekenis, G., Barzel, B., Slotine, J.-J., Liu, Y.-Y. & Barabási, A.-L. 2015 Spectrum of controlling and observing complex networks. *Nature Physics* .

You, D., Ham, F. & Moin, P. 2008 Discrete conservation principles in large-eddy simulation with application to separation control over an airfoil. *Physics of Fluids* **20**.

Zhang, W. & Samtaney, R. 2016 Biglobal linear stability analysis on low-re flow past an airfoil at high angle of attack. *Physics of Fluids (1994-present)* **28** (4), 044105.

Zhang, X. 2003 The evolution of co-rotating vortices in a canonical boundary laryer with inclined jets. *Physics of Fluids* **15** (12), 3693–3702.

AFOSR Deliverables Submission Survey

1.

1. Report Type

Final Report

Primary Contact E-mail
Contact email if there is a problem with the report.

ktaira@fsu.edu

Primary Contact Phone Number
Contact phone number if there is a problem with the report

850-645-0140

Organization / Institution name

Florida State University

Grant/Contract Title
The full title of the funded effort.

(YIP 13) Understanding the fundamental roles of momentum and vorticity injections in flow control

Grant/Contract Number
AFOSR assigned control number. It must begin with "FA9550" or "F49620" or "FA2386".

FA9550-13-1-0183

Principal Investigator Name
The full name of the principal investigator on the grant or contract.

Kunihiko Taira

Program Manager
The AFOSR Program Manager currently assigned to the award

Douglas Smith

Reporting Period Start Date

05/15/2013

Reporting Period End Date

05/14/2016

Abstract

The objective of this study is to numerically investigate the fundamental roles that momentum and vorticity injections play in suppressing flow separation over a canonical airfoil. Open-loop control of separated, incompressible flow over a NACA 0012 airfoil at Re = 23,000 is examined through large-eddy simulations. We find that the modification to the flow field can be captured by quantifying both the effects of wall-normal momentum (coefficient of momentum) and wall-normal vorticity (derived coefficient of circulation), by considering a newly defined total input parameter (total coefficient). Moreover, the study has developed advanced analysis techniques. First, the capability to perform bi-global stability analysis has been developed and validated, which can serve as a basis for physics-based active flow control guided by the knowledge of hydrodynamic instabilities. Second, as part of modeling complex unsteady flows in general, efforts in this study have led to the initial development of a novel network-theoretic approach in quantifying nonlinear interactions present in vortical flows.

Distribution Statement
This is block 12 on the SF298 form.

DISTRIBUTION A: Distribution approved for public release.

Distribution A - Approved for Public Release

Explanation for Distribution Statement

If this is not approved for public release, please provide a short explanation. E.g., contains proprietary information.

SF298 Form

Please attach your SF298 form. A blank SF298 can be found here. Please do not password protect or secure the PDF The maximum file size for an SF298 is 50MB.

AFOSR-YIP-SF298.pdf

Upload the Report Document. File must be a PDF. Please do not password protect or secure the PDF . The maximum file size for the Report Document is 50MB.

AFOSR_YIP_final_report.pdf

Upload a Report Document, if any. The maximum file size for the Report Document is 50MB.

Archival Publications (published) during reporting period:

P. M. Munday & K. Taira, ``Separation control on NACA 0012 airfoil using momentum and wall-normal vorticity injection,'' AIAA 2014-2685, 2014.

P. M. Munday & K. Taira, ``Surface vorticity flux analysis in separation control on NACA 0012 airfoil,'' AIAA 2015-2632, 2015.

A. G. Nair & K. Taira, ``Network-theoretic approach to sparsified discrete vortex dynamics,'' J. Fluid Mech. 768, 549-571, 2015.

K. Taira, A. G. Nair, & S. L. Brunton, ``Network structure of two-dimensional decaying isotropic turbulence,'' J. Fluid Mech. 795, R2, 2016.

2. New discoveries, inventions, or patent disclosures:

Do you have any discoveries, inventions, or patent disclosures to report for this period?

Yes

Please describe and include any notable dates

Pending Patent;

K. Taira, P. Munday, and F. Alvi, No. 61/947,164, Swirling jet actuator for control of separated and mixing flows, 2015.

Do you plan to pursue a claim for personal or organizational intellectual property?

Yes

Changes in research objectives (if any):

Change in AFOSR Program Manager, if any:

Extensions granted or milestones slipped, if any:

AFOSR LRIR Number

LRIR Title

Reporting Period

Laboratory Task Manager

Program Officer

Research Objectives

Technical Summary

Funding Summary by Cost Category (by FY, $K)

	Starting FY	FY+1	FY+2
Salary			
Equipment/Facilities			
Supplies			
Total			

Report Document

Report Document - Text Analysis

Report Document - Text Analysis

Appendix Documents

2. Thank You

E-mail user

Aug 12, 2016 10:48:54 Success: Email Sent to: ktaira@fsu.edu